

N70-72189

N70 72189

PREPARATION OF PIGMENTS FOR SPACE-STABLE THERMAL CONTROL COATINGS

by

W. B. Campbell, J. K. Cochran, J. W. Hinton,  
J. W. Randall, R. J. Versic, and J. E. Burroughs

**CASE FILE  
COPY**

THE OHIO STATE UNIVERSITY  
RESEARCH FOUNDATION

Prepared for

George C. Marshall Space Flight Center

Contract NAS8-21317

PREPARATION OF PIGMENTS FOR SPACE-STABLE THERMAL CONTROL COATINGS

June 1, 1968 through April 30, 1969

Contract No. NAS8-21317

Funded Under Code 124-09-18-1200-25-9-004-028-2510

Prepared by

W. B. Campbell  
J. K. Cochran  
J. W. Hinton  
J. W. Randall  
R. J. Versic  
J. E. Burroughs

of

The Ohio State University  
Research Foundation  
Columbus, Ohio

to

NATIONAL AERONAUTICS AND SPACE ADMINISTRATION

George C. Marshall Space Flight Center  
Marshall Space Flight Center, Alabama

July 1969

## ABSTRACT

The identification and control of vapor phase reaction kinetics to produce pigments by homogeneous nucleation have been achieved. A vapor phase apparatus has been designed, fabricated, and calibrated through 1500°C. Vapor phase reactions have been analyzed, calculations have been made, and powders of alumina, rutile, and zinc orthotitanate (in a mixed phase) have been produced by homogeneous nucleation. Electron microscopy shows uniform particle morphology and size. The anticipated advantages of vapor phase homogeneous nucleation (namely, purity, freedom from defects, and uniform particle sizing without grinding) have not been disproved.

### descriptors:

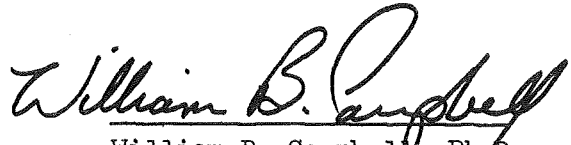
Thermal control space-stable pigments, Vapor phase,  
Nucleation, Alumina, Rutile, Zinc Orthotitanate,  
Ceramics

## FOREWORD

This report was prepared by The Ohio State University Research Foundation, under NASA Contract No. NAS8-21317, entitled, "Preparation of Pigments for Space-Stable Thermal Control Coatings." This report covers the period from June 1, 1968 through April 30, 1969.

Major contributors to the program during this period were Dr. William B. Campbell, Principal Investigator; J. K. Cochran, J. W. Hinton, J. W. Randall, and R. J. Versic for vapor phase apparatus development, powder production, and for free energy computer programming studies; and J. E. Burroughs, program management and planning.

Respectfully submitted,  
OSU Research Foundation



William B. Campbell, Ph.D.  
Associate Professor

Approved by:



Executive Director  
OSU Research Foundation

## SUMMARY

The development of vapor phase technology in the preparation of space-stable pigments has been demonstrated by the production of very fine rutile powders with discrete morphology and an average particle size of  $0.7\mu$ .

The critical parameters for the controlled production of rutile, and alumina have been used as the basis for the development of monosized particles of zinc orthotitanate. Zinc orthotitanate ( $\text{Zn}_2\text{TiO}_4$ ) has been found to be one of the better space-stable pigments for use in thermal-control paints of low  $\alpha$  and low  $\alpha/\epsilon$  ratio (solar absorptance and infrared emittance). Because of these stringent requirements, it is believed that the development of vapor phase reactions to produce zinc orthotitanate by homogeneous nucleation is the best approach.

Vapor phase apparatus has been designed, fabricated, and calibrated. Vapor phase reactions have been analyzed, calculations have been made, and powders of alumina, rutile, and zinc orthotitanate (in a mixed phase) have been produced by homogeneous nucleation. Submicron size particles required for efficient scattering of solar radiation in the  $0.35$  to  $2.5\mu$  wavelength range have been produced. Excellent sub-angular morphology was exhibited in the electron photomicrographs.

# TABLE OF CONTENTS

<u>Section</u>		<u>Page</u>
I	INTRODUCTION	1
	A. Program Objective	1
	B. Survey of Literature	2
	1. Pigment Properties for Thermal Control Coatings of Space Vehicles	2
	2. Phase Equilibrium in the ZnO-TiO <sub>2</sub> System	3
	3. Vapor Phase Powder Technology Developments	5
II	PRINCIPLES OF VAPOR PHASE POWDER PRODUCTION	
	A. Thermodynamics of Zinc Orthotitanate Reactions	7
	B. Production of Metal Vapor Species	10
III	EXPERIMENTAL PROCEDURE	15
	A. Apparatus Design and Fabrication	15
	1. Chlorinator	15
	2. Powder-Gas Separation	15
	3. Gas Scrubbers	18
	4. Computer Program	23
	B. Apparatus Control	24
	1. Gas Flow Control	24
	2. Metal Vapor Species Production	24
	3. Vapor Phase Reaction Furnace	28
	4. System Pressure Control	29
	5. Gas Temperature Measurement	29
	C. Operation Procedure for Vapor Phase Runs	31
IV	EXPERIMENTAL RESULTS	
	A. Aluminum Oxide (Al <sub>2</sub> O <sub>3</sub> ) Production and Characterization	33
	1. Aluminum Oxide Production	33
	2. Aluminum Oxide Characterization	33
	B. Titanium Dioxide (TiO <sub>2</sub> ) Powder Production and Characterization	40
	1. Titanium Dioxide Powder Production	40

# TABLE OF CONTENTS - (continued)

<u>Section</u>	<u>Page</u>
2. Titanium Dioxide Powder Characterization	42
C. Zinc Orthotitanate ( $\text{Zn}_2\text{TiO}_4$ ) Powder Production and Characterization	49
1. Using Zinc Metal as the Zinc Vapor Species	49
2. Using Zinc Chloride as the Zinc Vapor Species	56
V CONCLUSIONS AND RECOMMENDATIONS	59
A. Conclusions	
1. Aluminum Oxide Powder	59
2. Titanium Dioxide Powder	59
3. Zinc Orthotitanate Powder	59
B. Recommendations for Future Effort	60
1. Zinc Orthotitanate Powder	60
2. Lanthanum Oxide and Calcium Tungstate Powders	60
REFERENCES	63
APPENDIX A FREE ENERGY VALUES USED IN THERMODYNAMIC CALCULATIONS	67
APPENDIX B COMPUTER PROGRAM FORMAT	69
APPENDIX C ALUMINUM OXIDE X-RAY DIFFRACTION PATTERNS	71
APPENDIX D TITANIUM DIOXIDE X-RAY DIFFRACTION PATTERNS	75
APPENDIX E ZINC ORTHOTITANATE X-RAY DIFFRACTION PATTERNS	79

# LIST OF FIGURES

<u>Figure No.</u>		<u>Page</u>
1	ZnO-TiO <sub>2</sub> Phase Diagram	4
2	Vapor Pressure of ZnCl <sub>2</sub> and Zn vs Temperature	12
3	Titanium Chlorinator	16
4	Chlorinator Temperature Distribution	17
5	Characteristics of Particles and Particle Dispersoids	19
6	Cyclone Separator	20
7	Typical Laboratory Scrubber	22
8	Vapor Phase Apparatus	25
9	Gas Flow Control Panel	25
10	Vapor Phase System	26
11	Zinc Vapor Apparatus	27
12	Actual Temperature Inside Reaction Tube vs Temperature Outside Reaction Tube for Various Gas Flow Rates	30
13	Temperature Profile of Vapor Phase Reaction Furnace	32
14	Electron Photomicrograph of Alumina Powder, 67,200X	36
15	Electron Photomicrograph of Alumina Powder, 43,400X	37
16	Electron Photomicrograph of Alumina Powder, 92,000X	38
17	Electron Photomicrograph of Alumina Powder, 43,400X	39
18	Particle Size Probability Plot of Alumina Powders	41
19	Electron Photomicrograph of Rutile Powder, Run TiO <sub>2</sub> -1, 22,400X	44
20	Electron Photomicrograph of Rutile Powder, Run TiO <sub>2</sub> -1, 22,400X	45
21	Electron Photomicrograph of Rutile Powder, Run TiO <sub>2</sub> -2, 42,400X	46



# LIST OF FIGURES (continued)

<u>Figure No.</u>		<u>Page</u>
22	Electron Photomicrograph of Rutile Powder, Run TiO <sub>2</sub> -2, 220,000X	47
23	Particle Size Distribution of Vapor Grown Rutile	48
24	Zinc Evaporation Rate vs Temperature at 50 mm Hg	51
25	Powder Deposition Zones	53
26	Electron Photomicrograph, Run Zn <sub>2</sub> TiO <sub>4</sub> -1, Zone 3, 40,000X	54
27	Electron Photomicrograph, Run Zn <sub>2</sub> TiO <sub>4</sub> -1, Zone 3, 82,000X	55
28	Double-Stage Chlorinator	61
29	X-ray Diffractometer Trace of Vapor Grown Aluminum Oxide Powder From Run VA-10	72
30	X-ray Diffraction Pattern for Alumina, Run VA-10	73
31	X-ray Diffractometer Trace of Vapor Grown Rutile Powder From Run TiO <sub>2</sub> -1	76
32	X-ray Diffraction Pattern for Titania, Run TiO <sub>2</sub> -1	77
33	X-ray Diffractometer Trace of Oxides from Run Zn <sub>2</sub> TiO <sub>4</sub> -2, Showing Zn <sub>2</sub> TiO <sub>4</sub> as the Major Phase	80
34	X-ray Diffraction Pattern for Zinc Orthotitanate, Run Zn <sub>2</sub> TiO <sub>4</sub> -1	81

# LIST OF TABLES

<u>Table No.</u>		<u>Page</u>
I	Free Energy Changes and Equilibrium Constants as a Function of Temperature for Zinc Orthotitanate Production Using Zinc Metal	8
II	Free Energy Changes and Equilibrium Constants as a Function of Temperature for Zinc Orthotitanate Production Using Zinc Chloride	9
III	Estimate of Maximum Free Energy of Zinc Orthotitanate	11
IV	Free Energy Changes and Equilibrium Constants as a Function of Temperature for Zinc Oxide Chlorination	14
V	Free Energy Changes and Equilibrium Constants as a Function of Temperature for Aluminum Oxide Production	34
VI	Conditions for Aluminum Oxide Powder Production	35
VII	Free Energy Changes and Equilibrium Constants as a Function of Temperature for Titanium Dioxide Production	43
VIII	System Conditions for Rutile Powder Production	43
IX	System Conditions and Phase Analysis for Runs Using Zinc Metal as the Zinc Vapor Species	50
X	System Conditions and Phase Analysis for Runs Using Zinc Chloride as the Zinc Vapor Species	57
XI	Free Energy Changes and Equilibrium Constants as a Function of Temperature for Titanium Dioxide Chlorination	62
XII	Free Energy Values Used in Thermodynamic Calculations	68
XIII	X-ray Powder Diffraction Data for Alumina, Run VA-10	73
XIV	X-ray Powder Diffraction Data for Titanium, Run No. TiO <sub>2</sub> -1	77
XV	X-ray Powder Diffraction Data for Zinc Orthotitanate, Run Zn <sub>2</sub> TiO <sub>4</sub> -1	81

# PREPARATION OF PIGMENTS FOR SPACE-STABLE THERMAL CONTROL COATINGS

## I. INTRODUCTION

In the past decade, considerable effort has been expended to produce thermal control coatings that are stable to solar radiation in vacuum environments.<sup>1</sup>

In the past six years, the major emphasis in pigment research for thermal control coatings has been on zinc oxide which has consistently shown the greatest stability to ultraviolet irradiation in a vacuum. Of the new pigments under investigation, zinc orthotitanate has shown considerable promise as a new, potentially stable white-pigment.

The first zinc orthotitanate ( $\text{Zn}_2\text{TiO}_4$ ) pigment powder was prepared by mixing ZnO and  $\text{TiO}_2$  (anatase) in the mole ratio (2:1). Any residual ZnO must be removed by washing with acetic acid (complete removal is not always achieved). Stoichiometric considerations suggest that residual  $\text{TiO}_2$  remains, that other titanates are formed, or that titanium is present in interstitial solid solution in the orthotitanate lattice.<sup>2</sup>

Zinc orthotitanate is not completely space-stable and will degrade under space simulation. One of the primary factors believed responsible for promoting damage to the pigment powder is grinding; however, the extraction with acetic acid (previously mentioned) and washing are other important variables. A grinding or mulling operation is usually employed to obtain submicron-size particles that produce the efficient scattering of solar radiation in the 0.35 to  $2.5\mu$  wavelength range.

### A. PROGRAM OBJECTIVE

Since 1960 several exploratory investigations have established the feasibility of production of highly reproducible materials by vapor-phase reactions. Also, the morphology of vapor-phase productions has been controlled in these rapid reaction systems. Product morphologies have ranged from whiskers to bulk crystals to monodisperse powders.

The objective of this investigation is to apply the vapor-phase technology developed in earlier investigations to the production of space-stable pigments of zinc titanates, zirconates, etc. The primary material system to be considered is zinc orthotitanate.

Zinc orthotitanate ( $\text{Zn}_2\text{TiO}_4$ ), which was found to be one of the better space-stable pigments of low  $\alpha$  and low  $\alpha/\epsilon$  ratios (solar absorptance and infrared emittance), was selected as the primary material for

production by homogeneous nucleation in a quantity sufficient for pigment evaluation.

The vapor reaction system has the potentials of close control of chemical composition, production of monosized crystalline particles, and retention of structural integrity -- all with sizeable production batches.

## B. SURVEY OF LITERATURE

### 1. Pigment Properties for Thermal Control of Space Vehicles

Temperature requirements for space vehicles impose stringent restrictions on the properties of thermal control coatings. Satellites containing electronic equipment must maintain temperatures of  $-10^{\circ}\text{C}$  to  $100^{\circ}\text{C}$  and should be kept in the temperature range of  $20^{\circ}$  to  $40^{\circ}\text{C}$  for reliable operation. Manned space vehicles must maintain an even more narrow temperature range and must not exceed  $45^{\circ}\text{C}$  for more than a few minutes.<sup>3</sup>

The average equilibrium surface temperature of a vehicle in space is given by the following general equation:<sup>3</sup>

$$T = \sqrt{\frac{(\alpha/\epsilon)(P_s + P_a) + P_e}{A\sigma}} \quad (1)$$

where

- $\alpha$  = solar absorptivity of external body surface;
- $\epsilon$  = hemispherical emittance of external body surface, assumed to be equal to the absorptance of the Earth-emitted radiation;
- $P_s$  = direct solar radiation incident upon the body;
- $P_a$  = Earth-reflected solar radiation upon the body;
- $P_e$  = Earth-emitted radiation incident upon the body;
- $A$  = surface area of the body; and
- $\sigma$  = Boltzman's constant.

To maintain low temperatures in a space vehicle, a coating of low  $(\alpha/\epsilon)$  ratio and a low  $\alpha$  is desired, as predicted by Eq. (1). A number of inorganic ceramic pigments, including zinc orthotitanate, possess low  $\alpha/\epsilon$  ratios.

In recent years inorganic pigments, once believed to be extremely stable, have been shown to be subject to ultraviolet and proton degradation. The mechanisms involved in degradation having a

minimum of structural defects would be the most space stable. When pigments degrade, the solar absorption ( $\alpha_s$ ) increases, thereby increasing the  $\alpha/\epsilon$  ratio.

The primary purpose of a thermal control coating is to reflect as much radiation as possible; thereby preventing the radiation from reaching the interior of the space vehicle. The most important factor to consider in the reflectivity of a two-phase coating are (1) the particle size of the pigment, (2) the relative index of refraction of the pigment and the binder, and (3) the volume of the pigment present in the coating.<sup>4</sup> Maximum backscattering or reflectance is obtained when the particle size of the pigment is of the same order of magnitude as the wavelength of the incident radiation. For solar radiation, the maximum intensity is between 0.35 and 2.5 $\mu$ .

For greatest reflectance, the index of refraction of the pigment should be significantly higher than that of the binder and the volume of particles should be as great as possible. A pigment suitable for a thermal control coating should (1) have a low ( $\alpha/\epsilon$ ) ratio, (2) be stable when subjected to ultraviolet radiation in a vacuum, (3) have a particle size in the 0.35 to 2.5 $\mu$  range, and (4) have a high index of refraction.

## 2. Phase Equilibrium in the ZnO-TiO<sub>2</sub> System

Compounds reported for the ZnO-TiO<sub>2</sub> system are zinc orthotitanate (Zn<sub>2</sub>TiO<sub>4</sub>), zinc metatitanate (ZnTiO<sub>3</sub>), and zinc sesquittitanate (Zn<sub>2</sub>Ti<sub>3</sub>O<sub>8</sub>). The study of phase equilibria in the ZnO-TiO<sub>2</sub> system made by Dulin and Rase<sup>5</sup> shows decomposition of zinc metatitanate into zinc orthotitanate and rutile at approximately 900°C (see Fig. 1) by the following reaction:



In the composition region ZnO·TiO<sub>2</sub> to ZnO·2TiO<sub>2</sub>, Bartram and Slepety's<sup>6</sup> report the formation of Zn<sub>2</sub>Ti<sub>3</sub>O<sub>8</sub> as the predominant phase from 600 to 900°C. Like the metatitanate, the sesquittitanate becomes unstable in the temperature region 900° - 1000°C. At temperatures greater than 1000°C, the sesquittitanate decomposes to orthotitanate and rutile by the following reaction:



The presence of Zn<sub>2</sub>Ti<sub>3</sub>O<sub>8</sub> may have been overlooked because of similarity between Zn<sub>2</sub>TiO<sub>4</sub> and Zn<sub>2</sub>Ti<sub>3</sub>O<sub>8</sub> structures. Variations in X-ray data have been previously attributed to solid solution of TiO<sub>2</sub> in Zn<sub>2</sub>TiO<sub>4</sub> instead of Zn<sub>2</sub>Ti<sub>3</sub>O<sub>8</sub>. One point on which there is general agreement is that zinc

# ZnO-TiO<sub>2</sub>

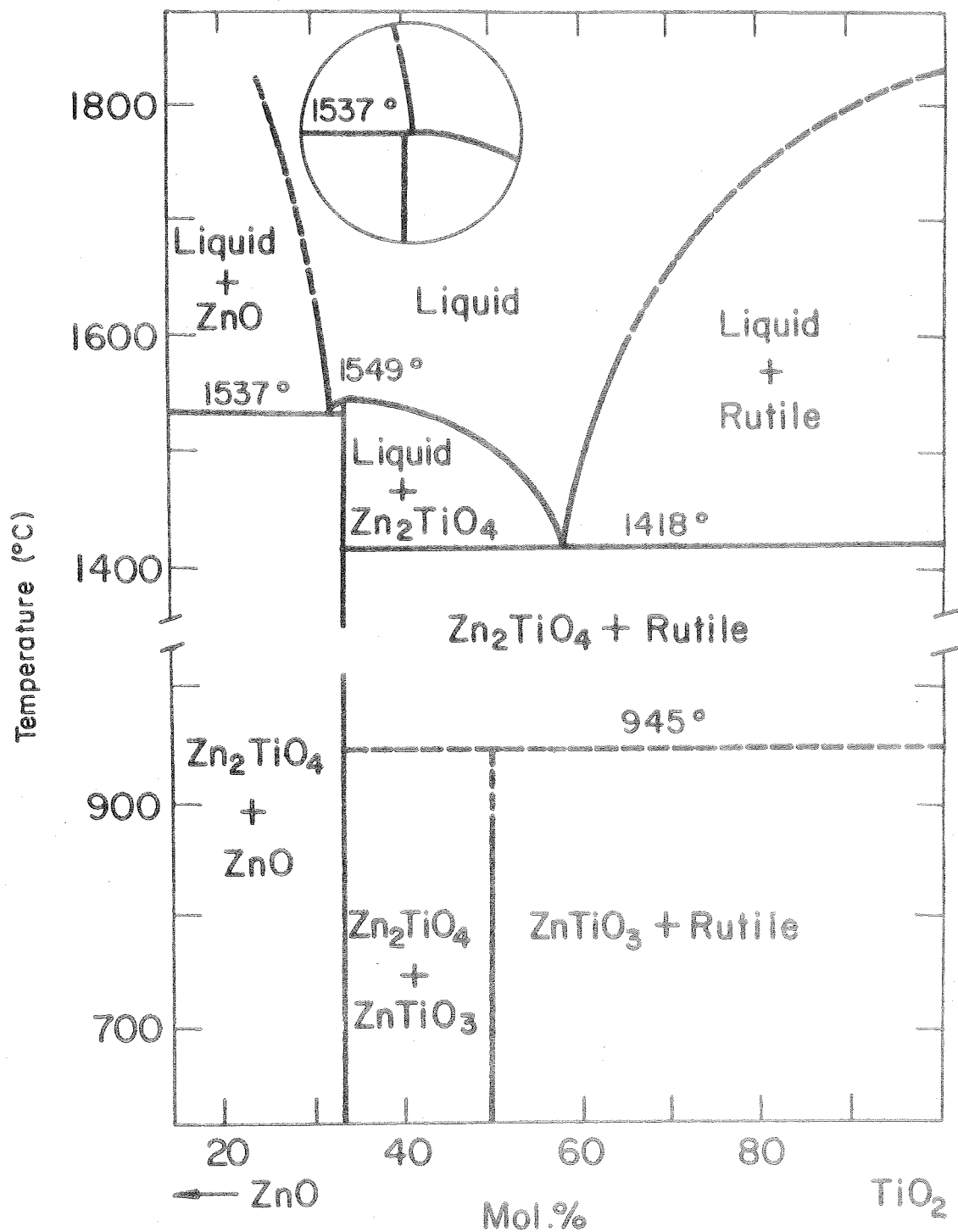


Fig. 1 - System ZnO-TiO<sub>2</sub>. Inset Shows Alternative Incongruent Melting of Zn<sub>2</sub>TiO<sub>4</sub>.<sup>5</sup>

orthotitanate is the only stable zinc oxide-titania compound above 1000°C.

The structures of zinc orthotitanate, zinc metatitanate, and zinc sesquitanate are inverse spinel, hexagonal, and defect spinel, respectively.<sup>6</sup> Zinc orthotitanate with an inverse spinel structure has 32 oxygen atoms in an approximately cubic close-packing arrangement, with 8  $\text{Zn}^{2+}$  ions in A sites with tetrahedral coordination, and 8  $\text{Zn}^{2+}$  + 8  $\text{Ti}^{4+}$  ions distributed randomly in B sites with octahedral coordination to the oxygen atoms. Zinc sesquitanate crystallizes in a defect spinel structure with 8  $\text{Zn}^{2+}$  ions in the tetrahedral positions and 12  $\text{Ti}^{4+}$  ions occupying the octahedral positions. Zinc metatitanate has an ilmenite-type structure.

### 3. Vapor Phase Powder Technology Developments

Aluminum oxide powder was produced by Campbell<sup>7</sup> from homogeneous nucleation in the vapor phase. Aluminum chloride, carbon dioxide, and hydrogen were reacted in an isothermal hot zone. Variables such as temperature, gas velocity, system pressure, and gas composition were shown to be controlling parameters for powder and whisker growth.

Schaffer and Jones<sup>8</sup> produced other oxide powders (i.e.,  $\text{SiO}_2$ ,  $\text{ZrO}_2$ ,  $\text{TiO}_2$ , and  $\text{ZnO}$  and the double oxide  $\text{ZnTiO}_3$ ) using a halide hydrolysis reaction and subsequent homogeneous nucleation of the powder in the gas phase using equipment similar to that of Campbell. Both chlorination and vaporization of zinc were used for production of  $\text{ZnO}$  and  $\text{ZnTiO}_3$ . Chlorination of zinc, proved unsatisfactory because of its high vapor pressure. Vaporization of zinc proved difficult to control because other reacting gases passed over its surface and oxide formation limited evaporation.

Vapor-grown zinc oxide pigmenting powders are produced in large quantities commercially by reaction of zinc oxide with coal at elevated temperatures. The coal reduces zinc oxide to zinc metal vapor, and the zinc vapor is later reoxidized to form zinc oxide powder by homogeneous nucleation. Other materials produced from the vapor phase are numerous.

**Page intentionally left blank**



## II. PRINCIPLES OF VAPOR PHASE POWDER PRODUCTION

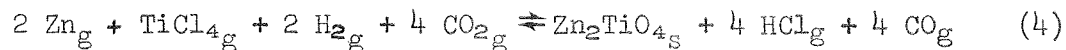
The fundamental considerations for a vapor phase reaction system are

- (1) the thermodynamic behavior of the system at selected temperatures;
- (2) the kinetics of nucleation, reaction, and evaporation; and
- (3) a basis for process control.

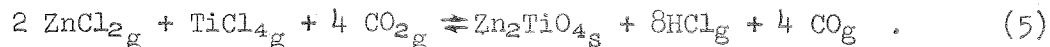
Formation of zinc orthotitanate was attempted by introducing vapor species of zinc and titanium into a heated reaction zone at constant temperature and pressure. Introduction of  $H_2$  and  $CO_2$  with the metal vapors provided the remaining reactants necessary to produce zinc orthotitanate by homogeneous nucleation. By carrying out the chemical reaction in a zone of constant temperature and pressure, the feasibility of the reaction could be predicted from thermodynamics.

### A. THERMODYNAMICS OF ZINC ORTHOTITANATE REACTIONS

The suitability of the thermodynamics for the zinc-titania system has been established by thermodynamic calculation and previous investigations. Two reactions were considered for production of zinc orthotitanate; i.e.,



and



By summing the free energies of the products of the reactions and subtracting the sum of the free energies of the reactants, the free energy changes for Eqs. (4) and (5) were obtained from room temperature to 2000°K. These values are summarized in Tables I and II. Free-energy data<sup>9,10</sup> were available for all the compounds in Eqs. (4) and (5) except  $Zn_2TiO_4$ . An estimate for  $Zn_2TiO_4$  was made using the following reaction:



Table I - Free-Energy Changes and Equilibrium Constants as Functions of Temperature for Zinc Orthotitanate Production Using Zinc Metal

T (°C)	T (°K)	$\Delta G^\circ$ Reaction 4* (Kcal/mole)	$K_p$ Reaction 4*
27	300	-38.90	$2.19 \times 10^{28}$
127	400	-46.25	$1.87 \times 10^{25}$
227	500	-50.15	$8.36 \times 10^{21}$
327	600	-50.90	$3.48 \times 10^{18}$
427	700	-54.15	$8.09 \times 10^{16}$
527	800	-56.85	$3.40 \times 10^{15}$
627	900	-59.50	$2.82 \times 10^{14}$
727	1000	-61.80	$3.22 \times 10^{13}$
827	1100	-63.75	$4.65 \times 10^{12}$
927	1200	-66.19	$1.14 \times 10^{12}$
1027	1300	-68.00	$2.71 \times 10^{11}$
1127	1400	-69.70	$7.61 \times 10^{10}$
1227	1500	-71.65	$2.76 \times 10^{10}$
1327	1600	-74.25	$1.39 \times 10^{10}$
1427	1700	-75.85	$5.65 \times 10^9$
1527	1800	-78.30	$3.22 \times 10^9$
1627	1900	-80.80	$1.97 \times 10^9$
1727	2000	-81.90	$8.92 \times 10^8$

\*  $2 \text{ Zn} + \text{TiCl}_4 + 2\text{H}_2 + 4 \text{ CO}_2 \rightleftharpoons \text{Zn}_2\text{TiO}_4 + 4 \text{ HCl} + 4 \text{ CO} \text{ (4)}$

Table II - Free-Energy Changes and Equilibrium Constants as Functions of Temperature for Zinc Orthotitanate Production Using Zinc Chloride

T (°C)	T (°K)	$\Delta G^\circ$ Reaction 5* (Kcal/mole)	$K_p$ Reaction 5*
27	300	47.00	$5.27 \times 10^{-35}$
127	400	31.55	$5.76 \times 10^{-18}$
227	500	16.45	$6.44 \times 10^{-8}$
327	600	13.10	$1.69 \times 10^{-5}$
427	700	4.65	$3.53 \times 10^{-2}$
527	800	-3.05	$6.81 \times 10^0$
627	900	-10.70	$3.97 \times 10^2$
727	1000	-17.80	$7.77 \times 10^3$
827	1100	-26.91	$2.22 \times 10^5$
927	1200	-36.91	$5.28 \times 10^6$
1027	1300	-45.28	$4.10 \times 10^7$
1127	1400	-54.54	$3.27 \times 10^8$
1227	1500	-63.25	$1.65 \times 10^9$
1327	1600	-70.85	$4.77 \times 10^9$
1427	1700	-76.85	$7.60 \times 10^9$
1527	1800	-84.30	$1.72 \times 10^{10}$
1627	1900	-91.60	$3.45 \times 10^{10}$
1727	2000	-96.90	$3.89 \times 10^{10}$

\*  $2 \text{ZnCl}_2 + \text{TiCl}_4 + 4 \text{H}_2 + 4 \text{CO}_2 \rightleftharpoons \text{Zn}_2\text{TiO}_4 + 8 \text{HCl} + 4 \text{CO} \quad (5)$

This reaction occurs above 780°C<sup>11</sup> and thus the free energy of one mole of Zn<sub>2</sub>TiO<sub>4</sub> must be more negative than the sum of the free energies of two moles of ZnO and one of TiO<sub>2</sub>. Assuming that the free energy change for reaction (6) is at least -5,000 cal/mole Zn<sub>2</sub>TiO<sub>4</sub>, a free-energy value for Zn<sub>2</sub>TiO<sub>4</sub> was calculated, as summarized in Table III.

As indicated in Tables I and II, the free-energy changes for Eqs. (4) and (5) are substantially negative with large equilibrium constants above 1300°K (1023°C). Thus the thermodynamics are favorable for the formation of Zn<sub>2</sub>TiO<sub>4</sub> above 1000°C where Zn<sub>2</sub>TiO<sub>4</sub> is the only stable zinc titanate compound.

#### B. PRODUCTION OF METAL VAPOR SPECIES

The metal vapor species were TiCl<sub>4</sub>, Zn, and ZnCl<sub>2</sub>. Titanium tetrachloride was produced by the chlorination of titanium at 400°C using the reaction



Reaction (7) has a large negative free-energy change from 300° to 2000°K. Titanium tetrachloride vaporizes readily at the chlorination temperature (350°C) since it boils at 136.4°C.

The chlorination of zinc was considered but several factors prohibited its use; namely,

1. at the system pressure, a temperature of 600°C or greater was necessary to vaporize zinc chloride and pass it into the reaction chamber. Previous chlorination of other metals had been attempted at 600°C and proved unsatisfactory using an external Inconel chlorinator. NiCl<sub>2</sub> vapor formed from reaction of Cl<sub>2</sub> with Inconel at this temperature, and condensed in the transfer line completely closing it;
2. zinc melts at 420°C and has a vapor pressure of 6 mm Hg at 550°C. Because of the high vapor pressure of zinc, substantial amounts of metal are introduced with zinc chloride vapor and flow rate control of the total zinc vapor species is lost. Zinc chloride vapor pressures calculated from the Clausius-Clapeyron equation,<sup>12</sup> and zinc vapor pressures<sup>13</sup> are plotted versus temperature in Fig. 2 to illustrate the close relationship between the vapor pressures of the two vapor species.

Table III - Estimate of Maximum Free Energy of Zinc Orthotitanate

Temperature		$2 \Delta G^\circ_{\text{ZnO}}$ (Kcal/mole)	$\Delta G^\circ_{\text{TiO}_2}$ (Kcal/mole)	$\Delta G^\circ_{\text{Zn}_2\text{TiO}_4}$ Estimate (Kcal/mole)
$^\circ\text{K}$	$^\circ\text{C}$			
300	27	-152.20	-212.00	-369.60
400	127	-149.30	-207.90	-362.20
500	227	-142.60	-203.60	-351.20
600	327	-137.90	-199.30	-342.20
700	427	-133.20	-194.30	-333.15
800	527	-121.00	-190.75	-323.75
900	627	-123.00	-186.55	-314.50
1000	727	-118.00	-182.35	-305.35
1100	827	-112.20	-178.00	-295.20
1200	927	-106.80	-173.89	-285.69
1300	1027	-101.40	-169.55	-275.95
1400	1127	-95.80	-165.45	-266.25
1500	1227	-90.20	-161.20	-256.40
1600	1327	-84.40	-157.25	-246.65
1700	1427	-78.80	-153.10	-236.90
1800	1527	-73.20	-149.35	-227.55
1900	1627	-67.60	-145.25	-217.85
2000	1727	-62.00	-141.15	-208.15

$$* \Delta G^\circ_{\text{Zn}_2\text{TiO}_4} = 2 \Delta G_{\text{ZnO}} + \Delta G_{\text{TiO}_2} - 5000 \text{ cal/mole Zn}_2\text{TiO}_4$$

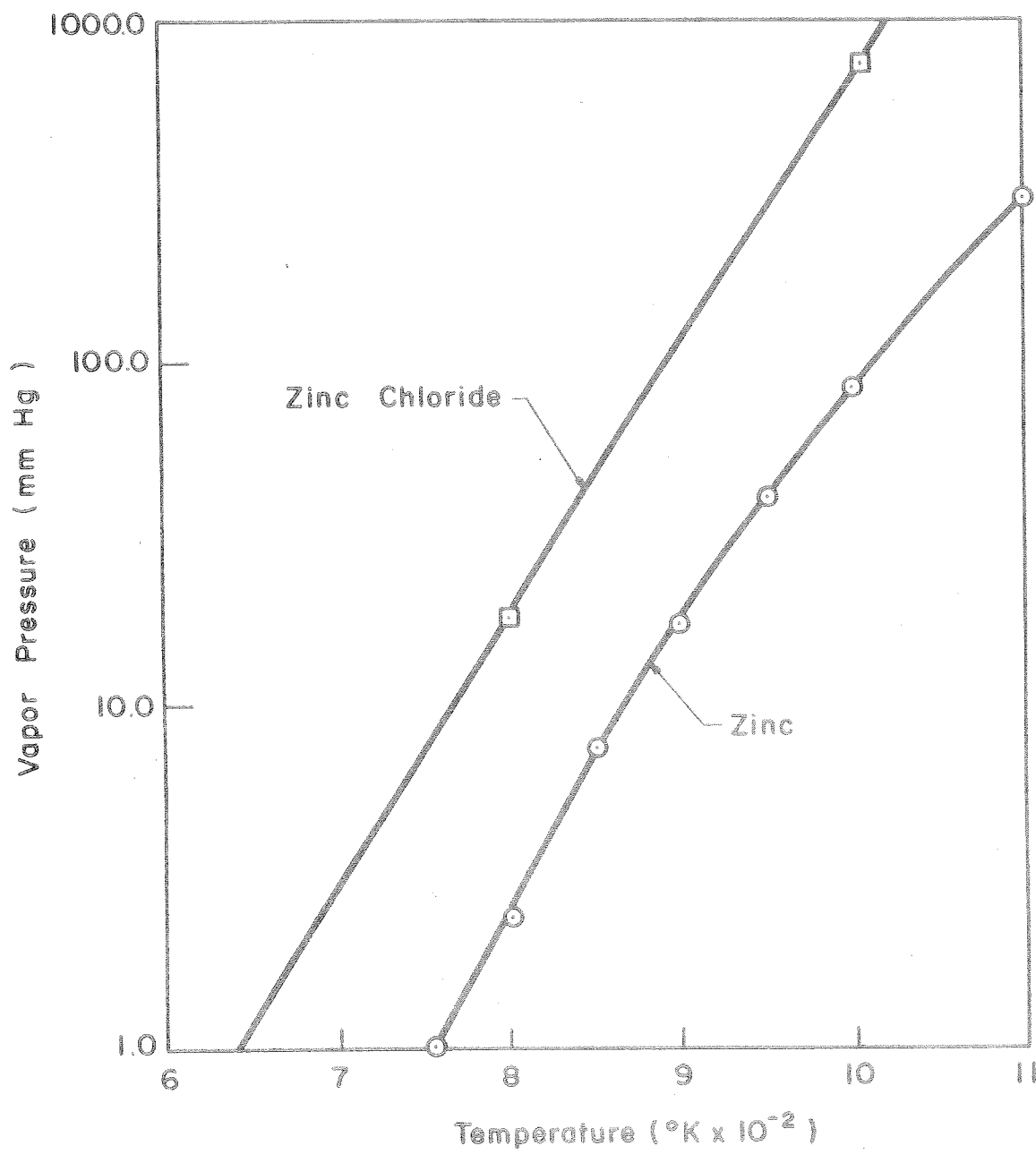


Fig. 2 - Vapor Pressure of  $\text{ZnCl}_2$  and Zn vs Temperature

It was decided to introduce zinc by evaporation of liquid metal from a constant surface area. A series of articles by Spendlove and St. Clair<sup>14-16</sup> showed that the rate of vaporization of zinc from a constant surface area is constant under conditions of constant power input and constant residual gas pressure. A general equation was derived for zinc evaporation; i.e.,

$$w = \sqrt{\frac{m}{2RT}} (P_0 - P) \quad , \quad (8)$$

where

$w$  = zinc evaporation, g/cm<sup>2</sup>-sec  
 $m$  = molecular weight of zinc,  
 $R$  = gas constant  
 $T$  = Temperature, °C  
 $P_0$  = zinc vapor pressure at temperature  $T$ , and  
 $P$  = partial pressure of zinc in the system.

Data were presented on the rate of evaporation of zinc which indicated the rate of evaporation decreases as the residual gas pressure increases and increases as the power input and temperature increases. Based on Spendlove and St. Clair's work, an apparatus was built to evaporate zinc metal into the system.<sup>17</sup>

A second method for introducing zinc into the system consisted of the chlorination of zinc oxide by the reaction



The free-energy change for reaction 9 was approximately -10,000 cal/mole ZnCl<sub>2</sub>. To obtain a more favorable free-energy change the following reaction was used:



Reaction (10) gave a large free-energy change with a large equilibrium constant over the desired temperature range. Therefore, the thermodynamics are favorable for complete chlorination of ZnO if the kinetics are favorable.

The thermodynamic data for equation (10) are presented in Table IV. The results of ZnO chlorination will be presented later.

Vaporization of the zinc vapor species, which prevented chlorination of zinc metal, did not present a problem in the chlorination of zinc oxide because zinc oxide has a low vapor pressure at chlorination temperatures.

Table IV - Free-Energy Changes and Equilibrium Constants as a Function of Temperatures for Zinc Oxide Chlorination

T (°C)	T (°K)	$\Delta G^\circ$ Reaction 10* (Kcal/mole)	$K_p$ Reaction 10*
27	300	-73.80	$5.86 \times 10^{53}$
127	400	-69.45	$8.89 \times 10^{37}$
227	500	-67.10	$2.15 \times 10^{29}$
327	600	-64.95	$4.57 \times 10^{23}$
427	700	-62.95	$4.52 \times 10^{19}$
527	800	-61.20	$5.25 \times 10^{16}$
627	900	-59.40	$2.66 \times 10^{14}$
727	1000	-57.65	$3.99 \times 10^{12}$
827	1100	-55.12	$8.96 \times 10^{10}$
927	1200	-52.54	$3.71 \times 10^9$
1027	1300	-49.81	$2.37 \times 10^8$
1127	1400	-47.48	$2.59 \times 10^7$
1227	1500	-44.85	$3.43 \times 10^6$
1327	1600	-43.50	$8.76 \times 10^5$
1427	1700	-42.30	$2.75 \times 10^5$
1527	1800	-41.15	$9.92 \times 10^4$
1627	1900	-39.85	$3.84 \times 10^4$
1727	2000	-38.75	$1.72 \times 10^4$

\* $\text{ZnO} + \text{Cl}_2 + \text{CO} \rightleftharpoons \text{ZnCl}_2 + \text{CO}_2$  (10)



### III. EXPERIMENTAL PROCEDURE

#### A. APPARATUS DESIGN AND FABRICATION

Several apparatus designs were reviewed and the following steps were taken to improve parts of the vapor phase system:

1. design and fabricate a chlorinator,
2. design and fabricate a powder-gas separator,
3. design a feasible gas scrubber system, and
4. develop a computer program to compute the free energy for any reaction having less than 15 reactions and 15 products.

##### 1. Chlorinator

Various possibilities for growing  $\text{Zn}_2\text{TiO}_4$  from the vapor phase have been reviewed, analyzed for application to the present system, and accepted or rejected because of transport problems. As discussed earlier, it was impossible to chlorinate metallic zinc in the chlorinator. Introduction of  $\text{TiCl}_4$  in the vapor phase reaction for  $\text{Zn}_2\text{TiO}_4$  looked favorable;  $\text{TiCl}_4$  results from the following reaction:



A chlorinator for titanium was designed, fabricated, and installed on the apparatus. The chlorinator was electrically insulated by wrapping pressed Fiberfrax around the surface; Kanthal wire was wrapped over the Fiberfrax. The chlorinator was thermally insulated by wrapping the Kanthal wire-wrapped chlorinator with Kaowool blanket-type insulation. The chlorinator temperature profile was stabilized and calibrated. Because of a temperature drop at the outlet end of the chlorinator, the Kanthal wrapping was modified. The rewrapped Kanthal was stabilized and calibrated. A schematic of this chlorinator is shown in Fig. 3 and the calibrations are shown in Fig. 4.

##### 2. Powder-Gas Separation

A survey of the literature provided several methods of solid gas separation.<sup>18-29</sup> Four separation processes may be useful; namely,

- (1) centrifugation,
- (2) electrostatic precipitation,
- (3) thermal precipitator, and
- (4) cyclone.

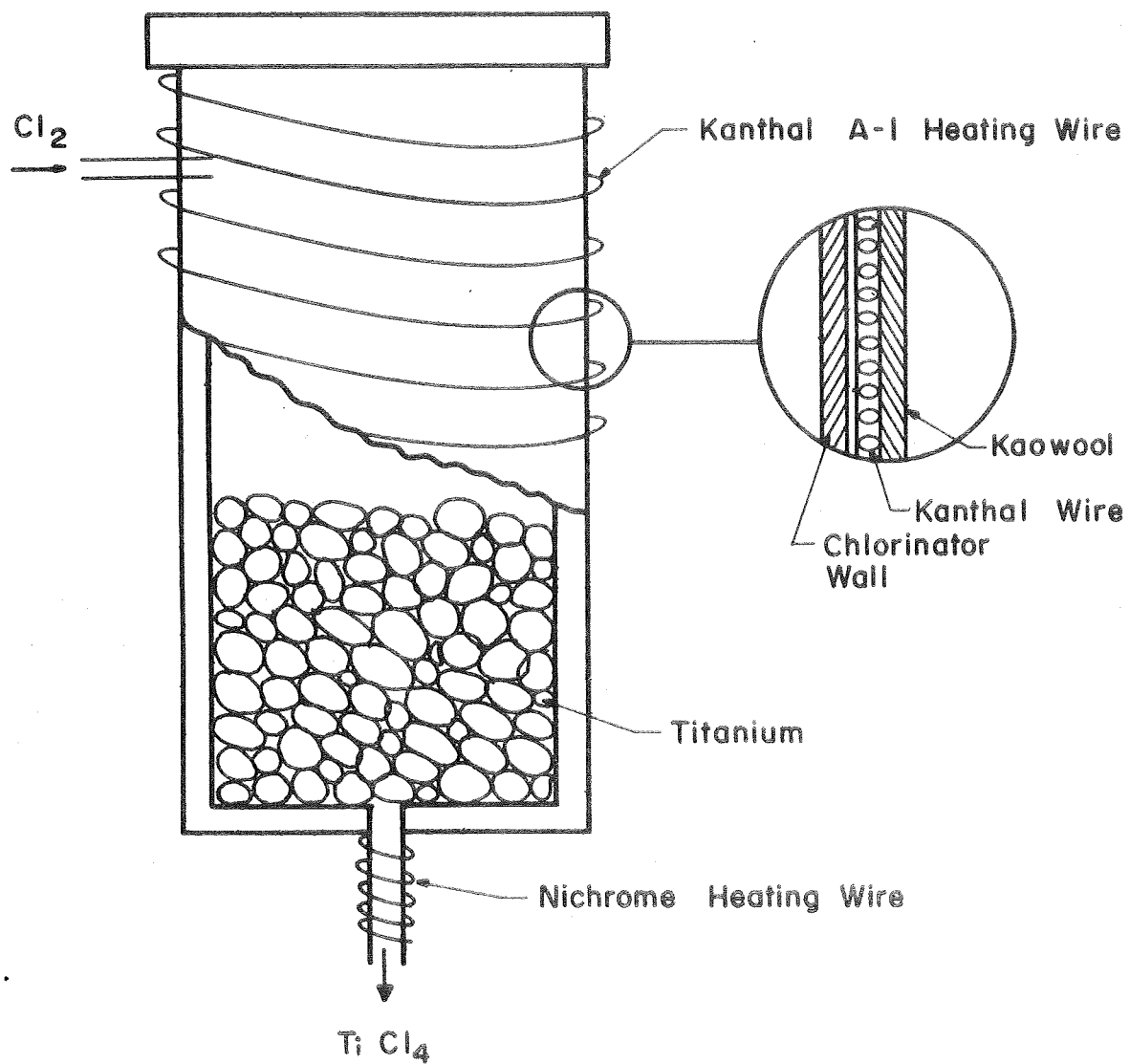


Fig. 3 - Titanium Chlorinator

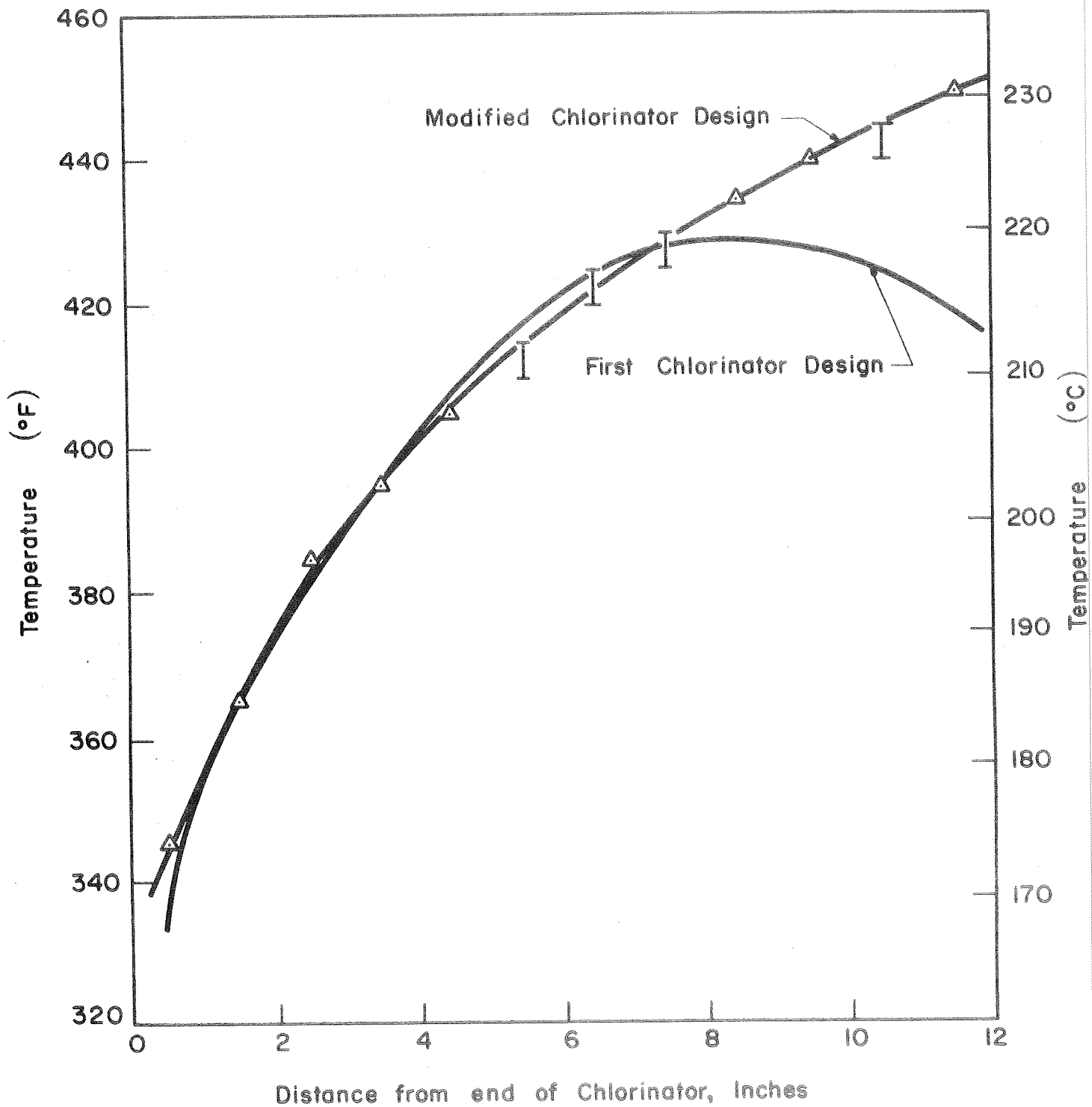


Fig. 4 - Calibration of Chlorinator Temperature Distribution

The performance of a particle collector is described as collection efficiency. Regardless of the figure of merit used to define efficiency, it should be remembered that performance is not a specific characteristic of a given collector but depends on the physical properties of the dispersoid. Figure 5 shows characteristics of particles and dispersoids together with the applicable types of gas cleaning. The primary distinguishing feature of gas dispersoids is particle size.

The most widely used unit of particle size is the micron ( $\mu$ ). The particle size of a gas dispersoid is usually taken as the average or equivalent diameter of the particle. The most widely used type of dust-collection equipment is the cyclone, in which dust-laden gas enters a cylindrical or conical chamber tangentially at one or more points and leaves through a central opening. The dust particles, by virtue of their inertia, will move toward the outside separator wall from which they are led into a receiver. At operating conditions commonly employed, the centrifugal separating force or acceleration may range from 5G, five times gravity, in very large diameter, low-resistance cyclones, to 2500G in very small, high-resistance units. The immediate entrance to a cyclone is usually rectangular.

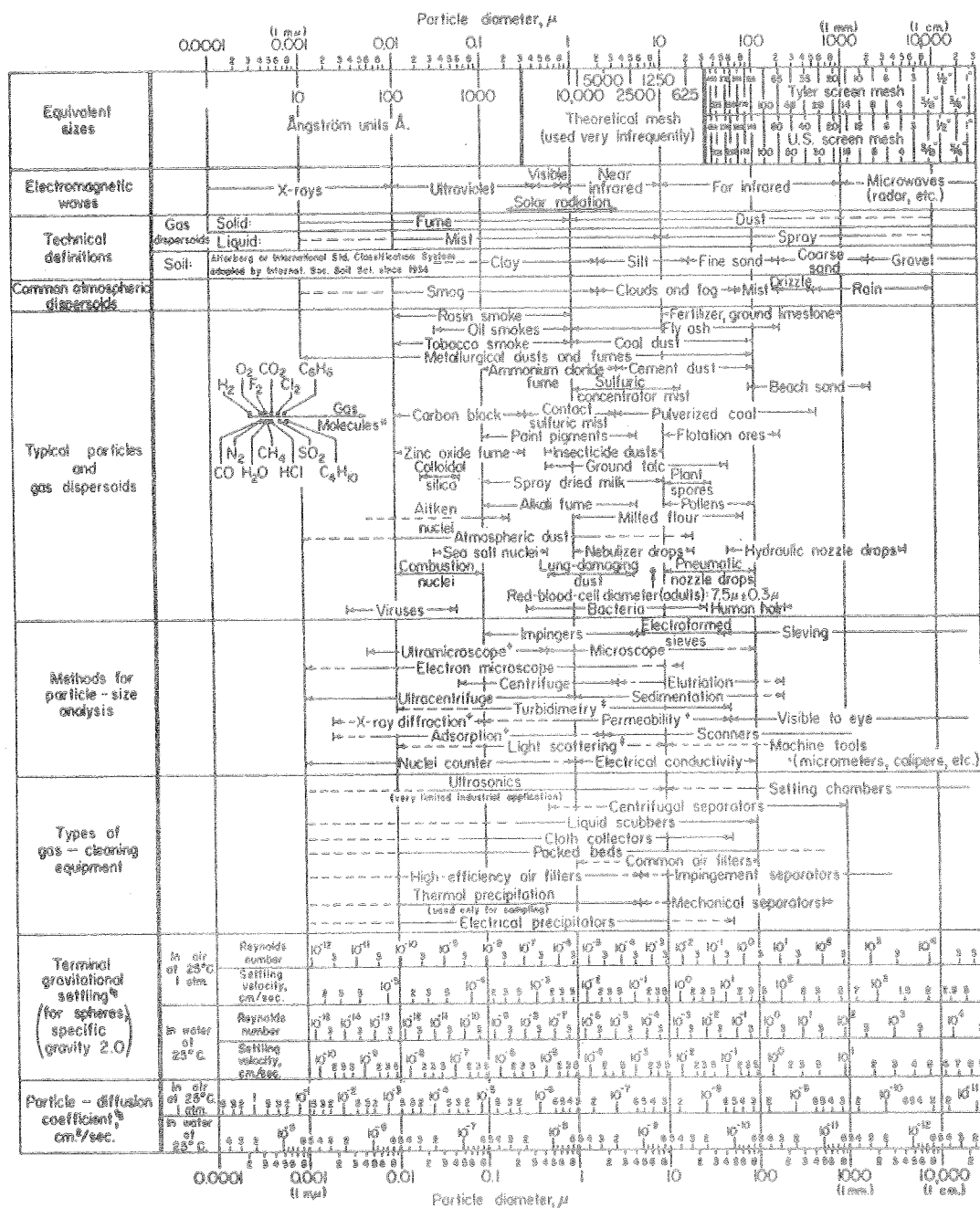
In a cyclone, the gas path involves a double vortex with the gas spiralling downward at the outside and upward at the center. When the gas enters the cyclone, its velocity undergoes a redistribution so that the tangential component of velocity increases with decreasing radius as expressed by  $V_{ct} \sim r^{-n}$ . A cyclone is essentially a settling chamber in which gravitational acceleration is replaced by centrifugal acceleration.<sup>30</sup> Because of the simplicity of construction, a pyrex cyclone was fabricated (a schematic is shown in Fig. 6).

### 3. Gas Scrubbers

Once a vapor phase reaction system is on line, it would be desirable to separate, recover, or convert into useful products the gaseous HCl,  $Cl_2$ , and CO. A review of the literature to identify efficient and practical means of recovering product gases indicated some of the wet-scrubbing techniques to be<sup>31-40</sup>

- a. spray towers,
- b. deflection washers,
- c. mechanical (combination of dry and wet),
- d. atomizing (venturi throat-type), and
- e. wetted fibers and packed towers (only method described for acid mist removal).

This survey was to examine both simple laboratory-type and large industrial scrubbers. A wet scrubber is defined as an apparatus



\* Molecular diameters calculated from viscosity data at 0°C.

\* Furnishes average particle diameter but no size distribution.

\* Size distribution may be obtained by special calibration.

\* Stokes-Cunningham factor included in values given for air but not included for water.

Fig. 5 - Characteristics of Particles and Particle Dispersoids.  
(Courtesy of the Stanford Research Institute, prepared by  
C. E. Lapple)<sup>30</sup>

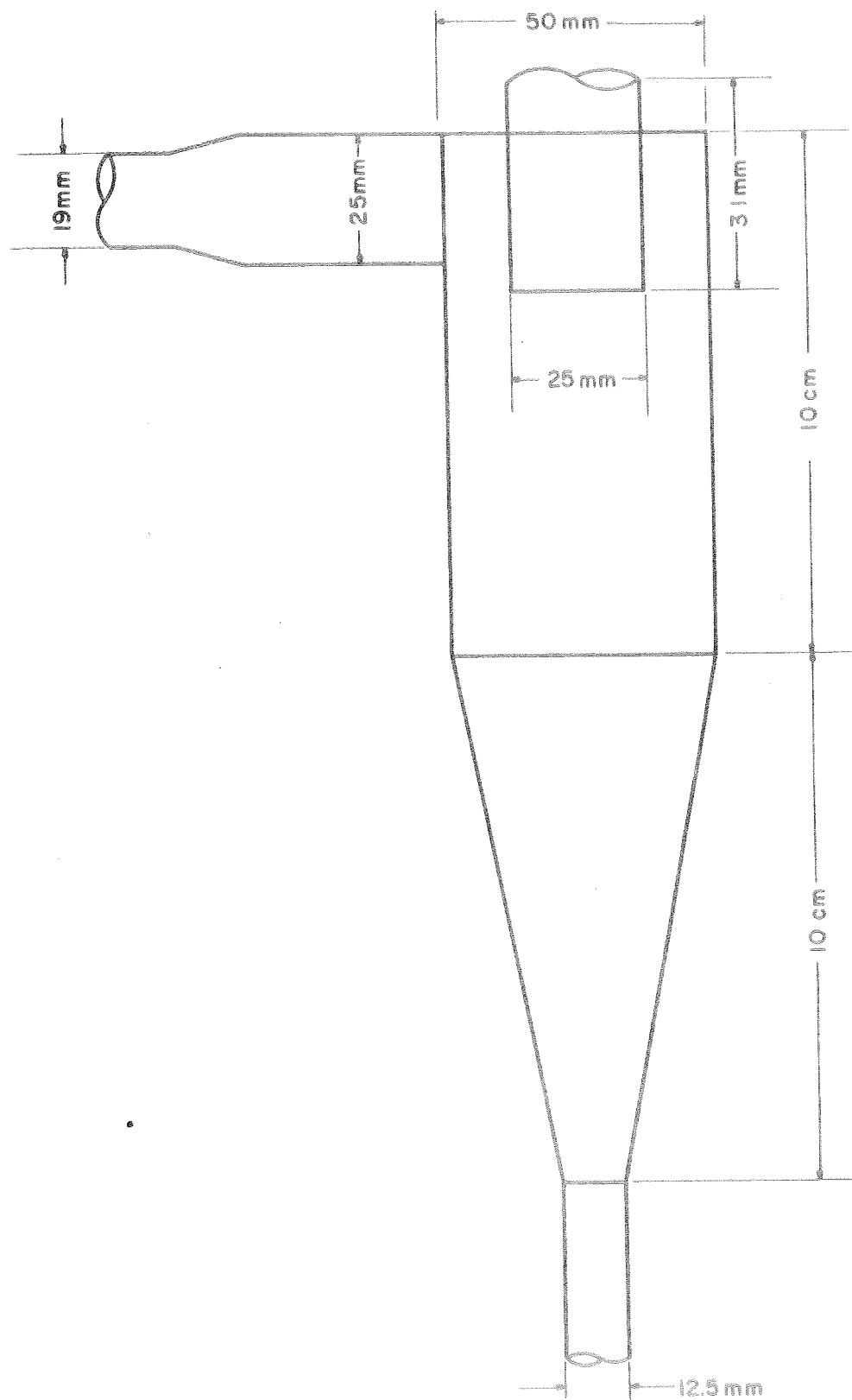
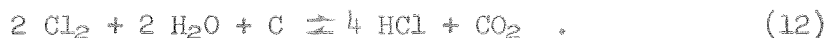


Fig. 6 - Cyclone Separator

in which a liquid is employed to achieve or assist in the removal of powders from gases. The scrubber described in the literature which combines scrubbing with dust and acid mist collection is the scrubber that will be described herein. Figure 7 shows a block-type flow plan and a schematic of a typical laboratory-type scrubber.

The basic and most essential part of this scrubber is the absorption tower, consisting of water flowing over activated charcoal.

The flows of the two fluids (water down and gas up) in the absorption tower are important. The water must flow at a minimum wetting rate (MWR) so that it wets all the charcoal. The relative flow of the two fluids (i.e., water and gas) must not be so large, however, that the upward flow of gas impedes the downward flow of water by bubbling through it, a point known as the loading point. At this point the pressure drops across the tower increases rapidly. If the relative flows are increased further, the flooding rate is reached, at which the flow of water is impeded. The tower is designed to operate at 0.2°C and remove HCl and Cl<sub>2</sub> from the gas stream. The HCl is removed by direct reaction with water. The absorption coefficient (that is, the solubility of HCl in water at 0°C and at 1/30 atm.) is 2.74 g/100 ml. The Cl<sub>2</sub> is removed by the reaction<sup>36</sup>



Because the solubility of Cl<sub>2</sub> in H<sub>2</sub>O is small, (i.e., ~ 0.1 g/100 ml at 0°C and 1/30 atm.) the above reaction will be the dominant mechanism for the removal of Cl<sub>2</sub> from the gas stream. With the HCl and Cl<sub>2</sub> removed from the gas stream, the gas out of the absorption tower consists of water vapor, CO, (from the original product gas) and CO<sub>2</sub> (from the Cl<sub>2</sub> reactions). At this point the gas stream is dried (possibly by a CaSO<sub>4</sub> drying column), passed through a vacuum pump to slightly above atmospheric pressure, and the CO-CO<sub>2</sub> mixture is passed through a separator.

Using available data for gas inputs in the vapor phase-growth apparatus, approximately  $4.3 \times 10^{21}$  molecules/minute of solid species are produced. For example, for Zn<sub>2</sub>TiO<sub>4</sub> this corresponds to  $4 \times 4.30 \times 10^{21}$  molecules of HCl. By converting the number of HCl molecules to moles and then to grams, we get approximately 1.0 grams. If the solubility of HCl in water at 1/30 atm and 0°C is 2.74 gm HCl/100 ml water, then 1.04 gm dissolves in 38 ml of water. If an equal amount of HCl is produced by the Cl<sub>2</sub> reaction in the absorption tower, then approximately 80 ml/min of water is necessary to remove the HCl and Cl<sub>2</sub> from the gas flow. Using a conservative safety factor (and realizing that the flow rates assumed in this treatment are high) then 200 ml/min of water should be sufficient.

The cold trap and back-flow trap upstream from the absorption tower are added variations that prevent solid particles from entering the absorption tower.

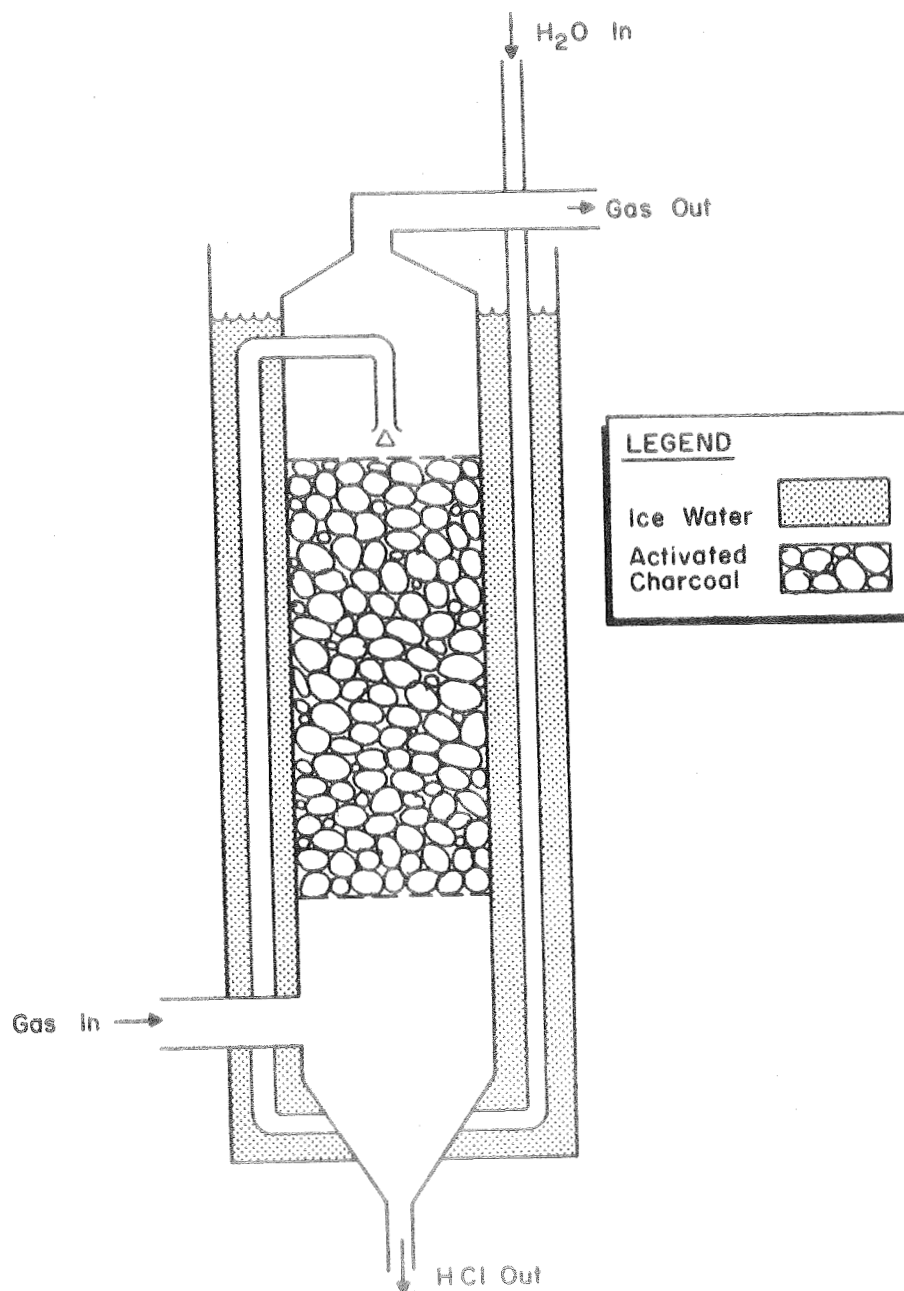
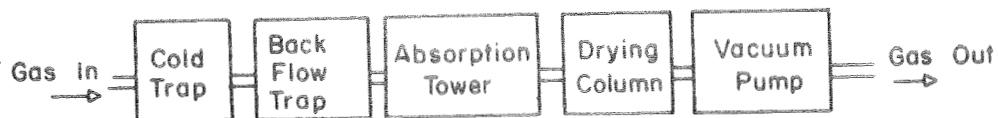
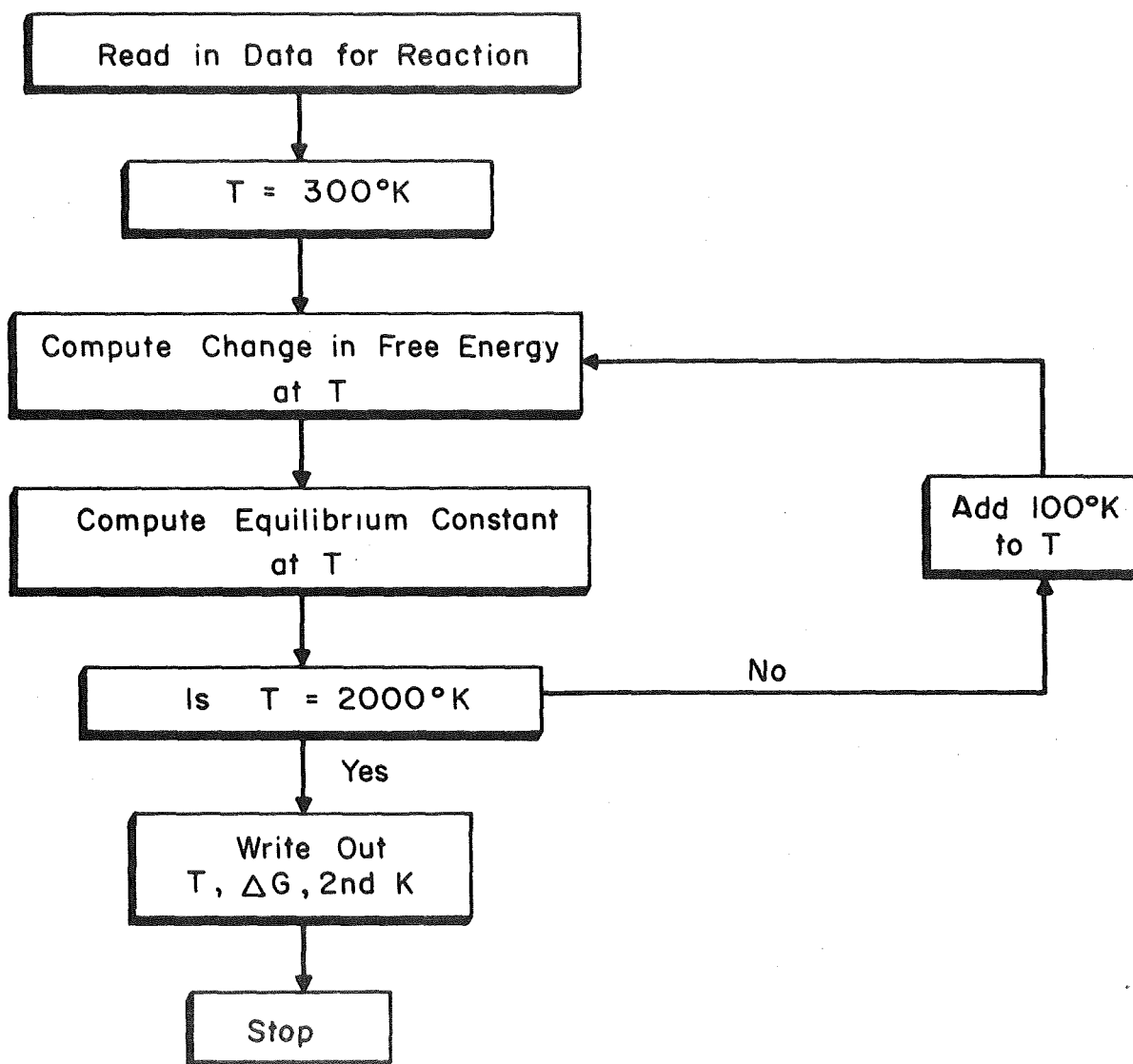


Fig. 7 - Typical Laboratory Scrubber



#### 4. Computer Program

A computer program was written for the IBM 360/75 computer to compute the free energy for any reaction having less than 15 reactants and 15 products. The computer program flow chart is shown below and the computer program is detailed in Appendix B.



Computer Program Flow Chart for Computing Thermodynamic Free Energy Values

## B. APPARATUS CONTROL

### 1. Gas Flow Control

Reactant gas flows were monitored using low-flow rotameters. Chemically pure CO, welding grade CO<sub>2</sub>, and 99.97 per cent H<sub>2</sub> were passed through calcium sulfate drying columns to remove moisture before monitoring. Chlorine (99.965 pure) was introduced into the system at three positions through three separate flowmeters and transfer lines. Refer to Figs. 8 through 10 for vapor phase apparatus, gas control panel, and a schematic of the system gas flow control, respectively.

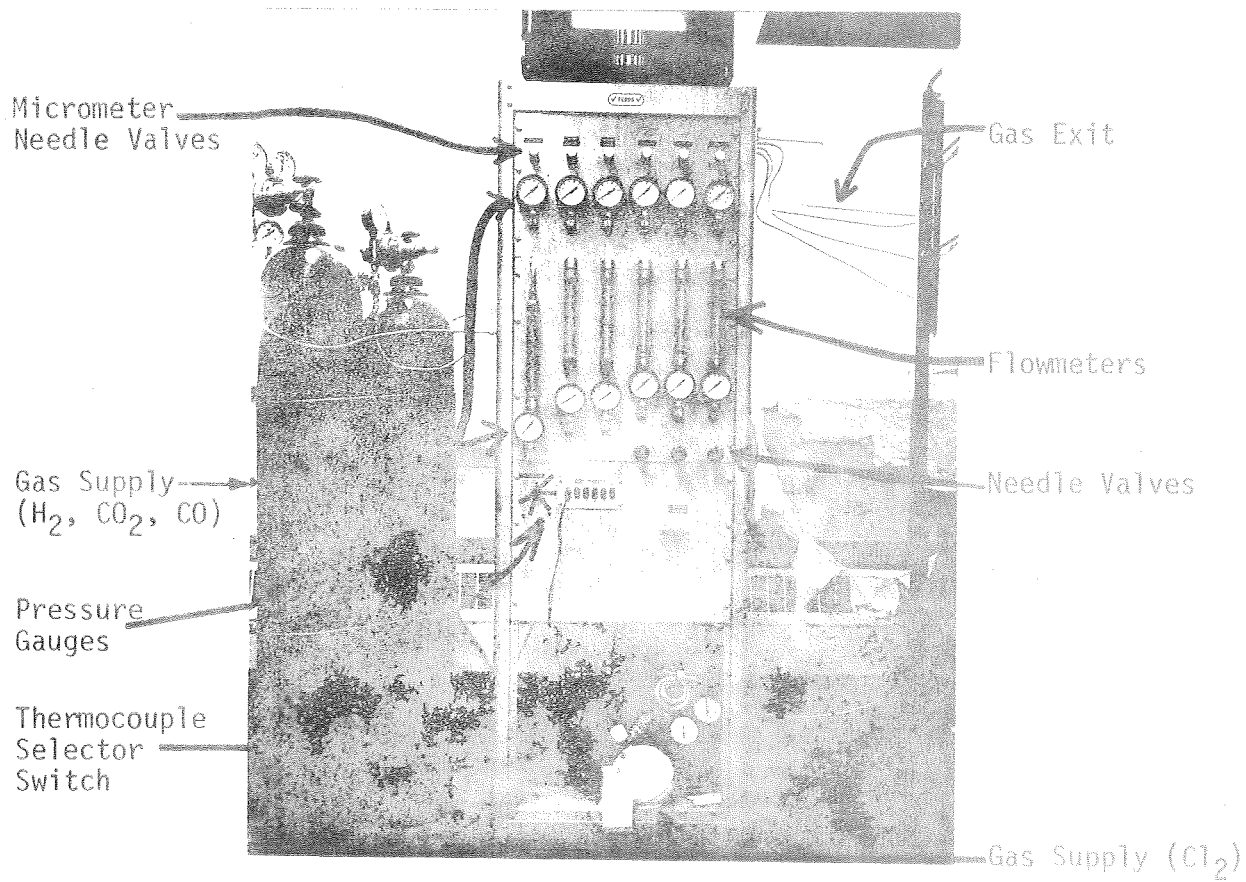
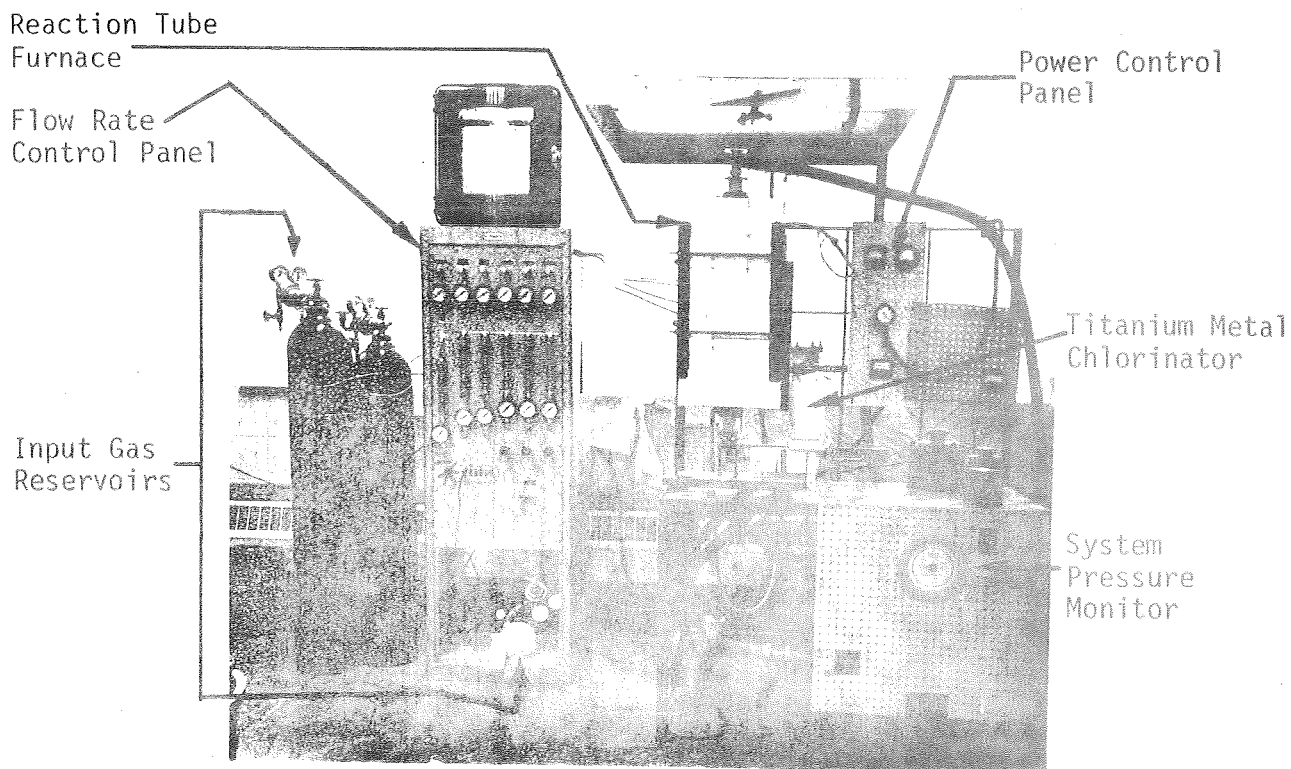
To provide greater flexibility in gas flow rate ranges, two sets of flowmeters were operated at different pressures. The low-flow rotameters were calibrated in cc/min at 0 psig and 5 psig for H<sub>2</sub>, CO, and CO<sub>2</sub>, and in cc/min at 0 psig and 25 psig for Cl<sub>2</sub>. For calculation of desired flow rates, gas pressure through the rotameters had to be considered. Gas pressures through the rotameters and flow rates were adjusted by micrometer needle valves below the rotameters.

### 2. Metal Vapor Species Production

a. Titanium and Aluminum Chlorination—Titanium tetrachloride and aluminum trichloride were introduced by chlorination of titanium and aluminum. The chlorinator (Fig. 6) was constructed of Inconel and is resistant to chlorine for temperatures up to 550°C at reduced pressures. Temperature control was achieved by wrapping the chlorinator with Kanthal wire and controlling the power input with a rheostat. Temperature of the titanium chlorinator was maintained at 400°C for all runs. The aluminum chlorinator was maintained at 300-400°C.

For titanium chloride production, titanium sponge was positioned in the chlorinator to ensure chlorine flow through the metal. For aluminum chloride production, aluminum foil was packed into the chlorinator. The transfer lines to the reaction system were heated with asbestos-insulated Nichrome wire and were maintained at 350°C to prevent condensation of the chloride species.

b. Zinc Vaporization—Zinc was introduced by vaporizing metallic zinc from a quartz glass crucible (see Fig. 11). The crucible was constructed from two cylinders 6 inches long with diameters of 12 mm ID and 15 mm OD, and 32 mm ID and 35 mm OD. A crucible was



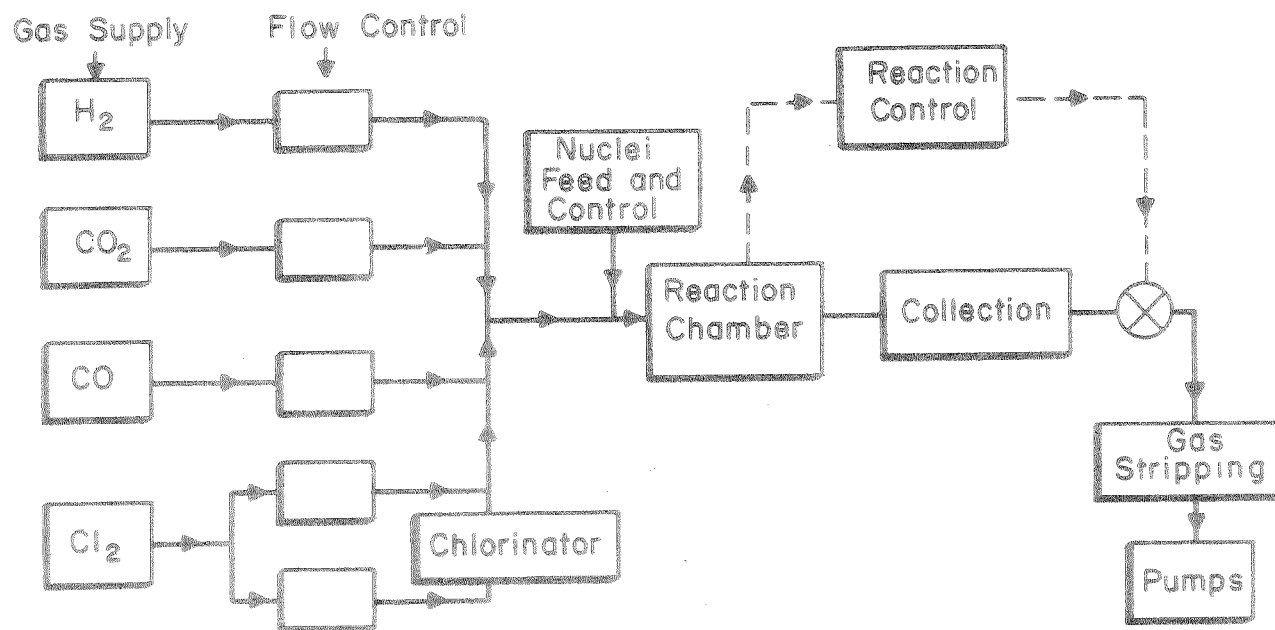


Fig. 10 - Vapor Phase System

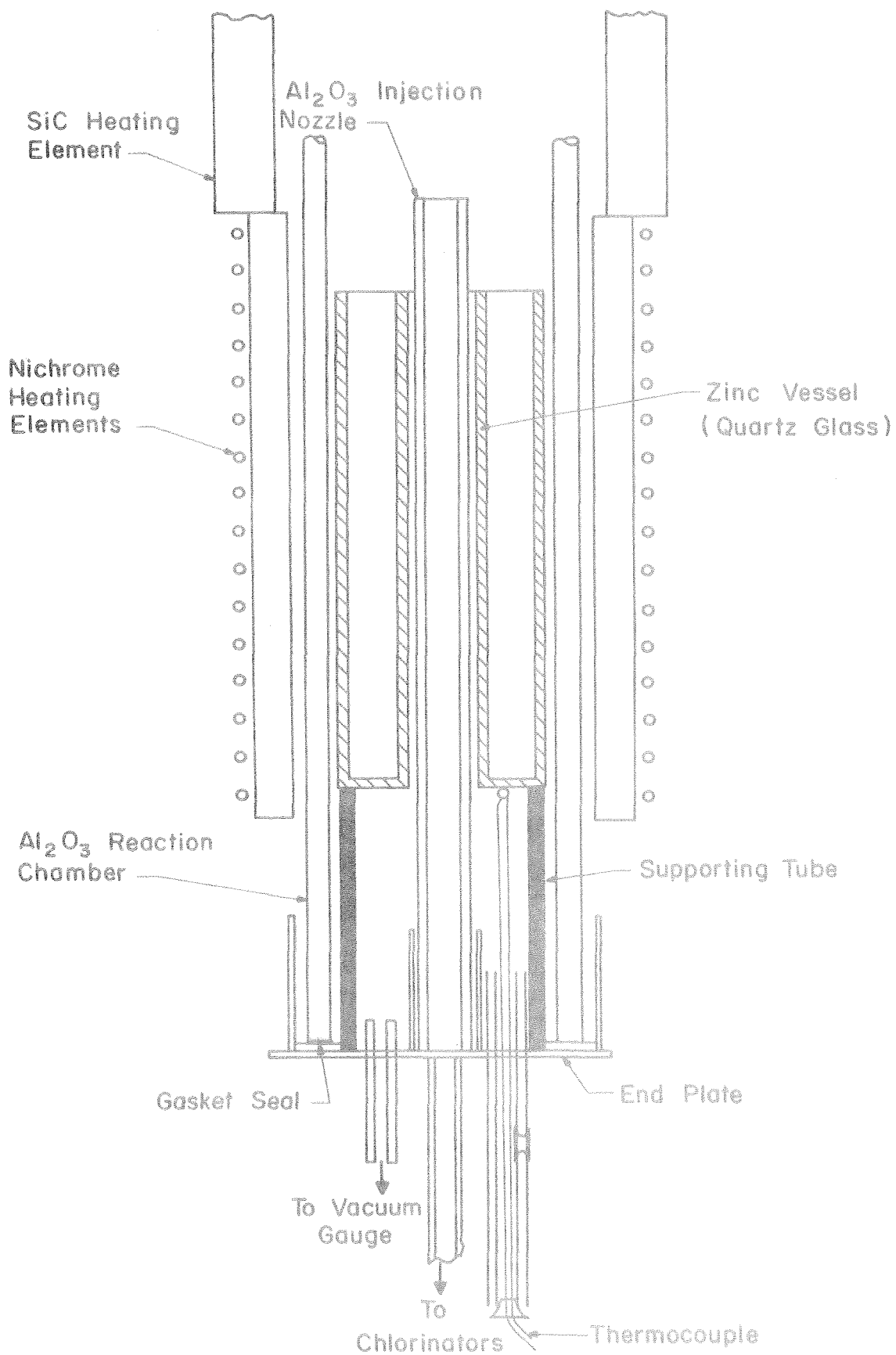


Fig. 11 - Zinc Vapor Apparatus

formed by placing the smaller tube concentrically inside the larger and joining the two at the bottom, leaving the smaller tube open at both ends. This configuration produced a calculated surface area of  $6.28 \text{ cm}^2$  between the two tubes perpendicular to the axis of rotation. The crucible was positioned with the axis of rotation vertical to maintain a constant evaporation surface area as vaporization proceeded and the liquid level decreased.

The portion of the reaction zone containing the zinc crucible was heated by an 8-inch tube muffle wrapped with asbestos-insulated Nichrome wire. The temperature of the metal was monitored by a thermocouple positioned against the bottom of the zinc crucible. Accuracy of the recorded temperature was determined by observing zinc melting. Sufficient power was supplied to the tube muffle to maintain a temperature between  $490^\circ\text{C}$  and  $650^\circ\text{C}$ , depending on the experiment.

c. Zinc Oxide Chlorination - Zinc oxide pellets were pressed from reagent grade  $\text{ZnO}$  and sintered at  $900^\circ\text{C}$ . The sintered  $\text{ZnO}$  pellets were crushed and screened to  $-4 + 10$  and  $-10 + 50$  mesh. A porous alumina disc was placed around the central injection nozzle and held in position by a quartz glass tube extending to the bottom of the reaction zone at the same height previously occupied by the bottom of the zinc crucible. Approximately two inches of  $-4 + 10$  mesh  $\text{ZnO}$  was placed on the alumina disc and above that was placed two inches of  $-10 + 50$  mesh  $\text{ZnO}$ .

Chlorine, carbon monoxide, and carbon dioxide gases were injected through a 0.25-inch Inconel tube at the bottom of the reaction zone. These gases passed through the  $\text{ZnO}$  bed and  $\text{ZnCl}$  was formed according to Eq. (10). Temperature control was provided by the same tube muffle furnace that controlled the zinc crucible temperature.

### 3. Vapor Phase Reaction Furnace

A silicon carbide tube furnace 21 inches long and 2.25 inches ID was used to heat a high-purity, recrystallized  $\text{Al}_2\text{O}_3$  tube 36 inches long with 38 mm ID and 46 mm OD. Reaction of gases and subsequent powder production occurred in a 6-inch long hot zone.

Use of silicon carbide in heating element provided a maximum temperature capability of  $1500^\circ\text{C}$ . Temperature was measured with a Pt-Pt 10% Rh thermocouple positioned between the  $\text{Al}_2\text{O}_3$  tube and the SiC heating element in the center of the hot zone.

The furnace was positioned vertically with the  $\text{Al}_2\text{O}_3$  reaction tube passing through the center and extending four inches above the heating element. The tube furnace used to heat the zinc and zinc oxide extended below the SiC heating element.

Gases were introduced into the reaction zone at the bottom and passed up through the furnace. When zinc was used as the zinc vapor species, all other gases were introduced through a central  $\text{Al}_2\text{O}_3$  injector nozzle (6 mm x 10 mm) that passed through the center of the zinc crucible and extended to within one inch of the hot zone. The  $\text{Al}_2\text{O}_3$  reaction tube was sealed at the base with a stainless steel plate and a silicone rubber gasket. Injection tubes were inserted through the stainless steel plate and silver solder-sealed to create a vacuum tight joint.

The top of the  $\text{Al}_2\text{O}_3$  reaction tube (outlet) was connected to a stainless steel tee joint and sealed with a silicone rubber gasket. The branch of the tee was connected to a rubber vacuum hose and the run of the tee was used as a sight window.

#### 4. System Pressure Control

System pressure was controllable from atmospheric pressure to 5 $\mu$  using two Duoseal vacuum pumps in parallel and a bleed valve which opened to the atmosphere. Pressure was monitored with two absolute diaphragm gages which had ranges of 0-50 mm Hg and 0-760 mm Hg.

#### 5. Gas Temperature Measurement

Because prediction of reaction products using thermodynamic data is based on constant temperature, it was necessary to know the actual temperature of the gases to verify reaction temperature. An alumina tube (10 mm in diameter) was positioned in the center of the hot zone with a thermocouple placed next to it. The temperature of the alumina tube was obtained by sighting an optical pyrometer on a mirror reflection through the viewing port while at the same time recording the thermocouple temperature. This provided a calibration of the radiation loss due to the mirror and glass viewing port. The thermocouple was next positioned between the alumina reaction tube and the silicon carbide heating element at the center of the hot zone at the same height as the 10 mm alumina sight tube. The system was evacuated and temperature measurement of the interior alumina sight tube and the thermocouple outside the reaction chamber were recorded for a range of temperatures, pressures, and gas flow rates. Hydrogen, carbon monoxide, and carbon dioxide were used as flow gases in the temperature measurements because they would not form solid reaction products which would interfere with the optical pyrometer readings. The effects of gas flows and pressure on reaction zone temperatures are shown in Fig. 12. The interior of the reaction zone was 10°C lower than the exterior when pressure was at a minimum and no gases were flowing. The interior temperature decreased as gas flow rates were increased. At the highest flow rate the interior temperature was approximately 40°C lower than the exterior

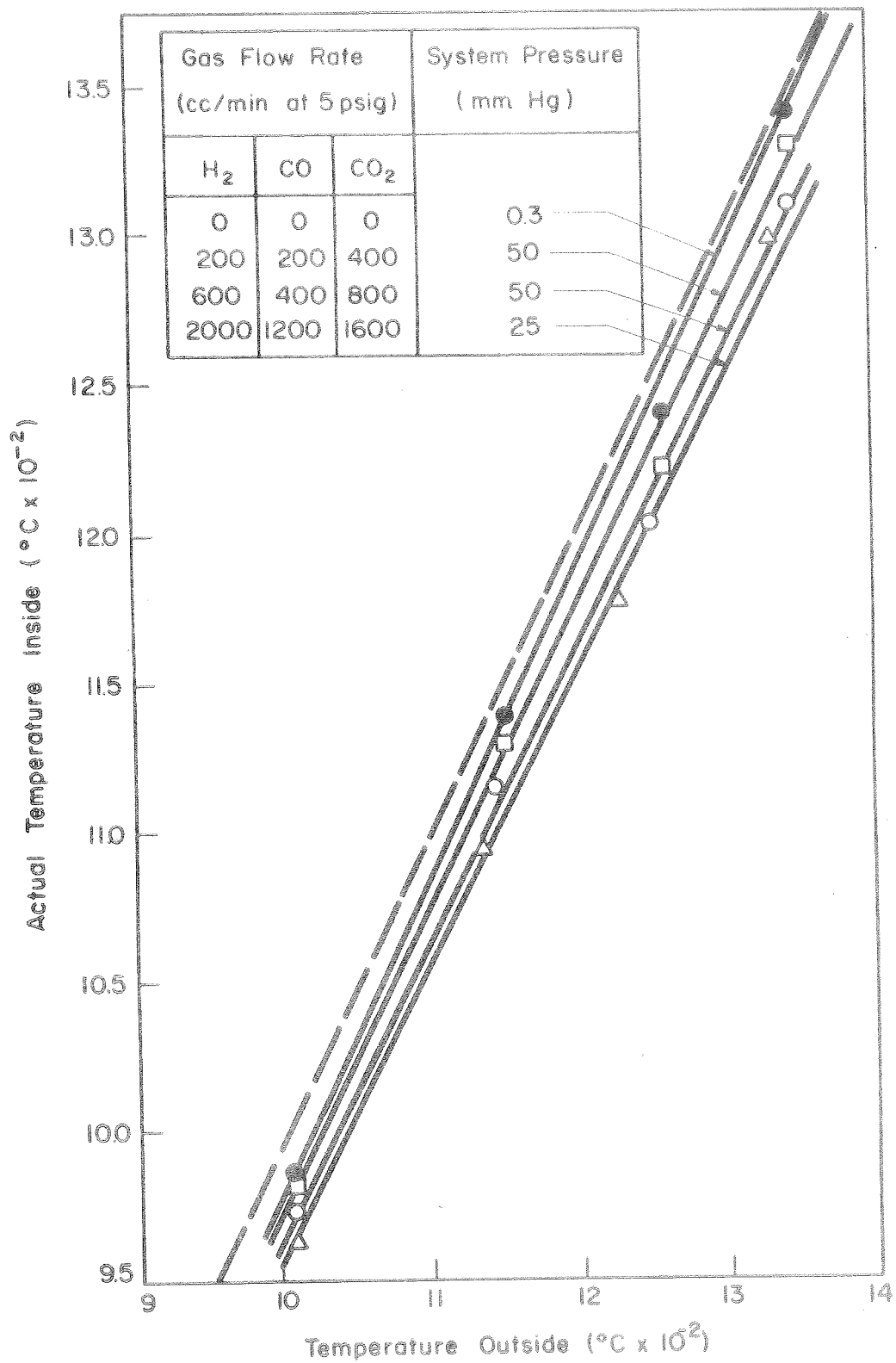


Fig. 12 - Actual Temperature inside Reaction Tube vs Temperature Outside Reaction Tube for Various Gas Flow Rates



temperature range of 1000°C to 1400°C. A temperature profile of the vapor reaction furnace is shown in Fig. 13.

#### C. OPERATION PROCEDURE FOR VAPOR PHASE RUNS

Zinc or zinc oxide and titanium, respectively, were weighed and put in the reaction zone and chlorinator. The system was evacuated and all portions of the system, except the zinc evaporation heater, were brought up to temperature and stabilized before each run. Liquid nitrogen was poured into the cold trap. With zinc evaporation as the zinc vapor source, the zinc heater was turned on approximately 30 minutes before starting the run and system pressure was raised to 140 mm Hg to prevent premature evaporation of zinc. Once zinc operating temperature was achieved, system pressure was lowered to the desired level. Gas flows were initiated in the following order;  $\text{Cl}_2$  to titanium,  $\text{CO}_2$ , and  $\text{H}_2$ . At the completion of the run, system pressure was raised again to stop zinc evaporation and zinc was cooled to 350°C prior to system evacuation. The system was closed above the cold trap, and the cold trap was removed and placed in a hood while the trapped gases evaporated. Once the chlorinator cooled to room temperature and there was no danger of rapid titanium oxidation, the reaction tube was removed from the system and the solid reaction products were analyzed.

When chlorination of ZnO was used as the zinc vapor species source, the ZnO was preheated with the rest of the system. System pressure was kept at a minimum until all gases were flowing, at which time the pressure was raised to the desired level.

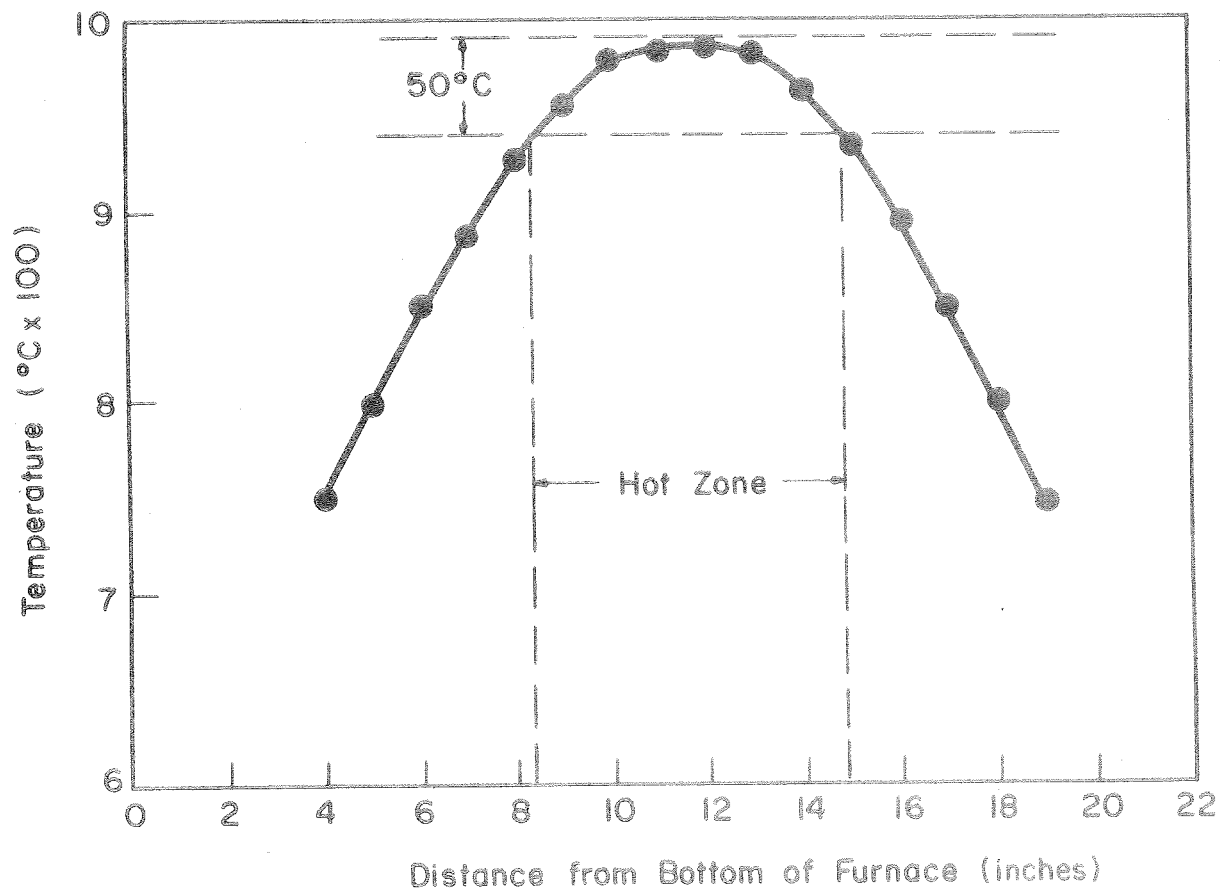


Fig. 13 - Temperature Profile of Vapor Phase Reaction Furnace

#### IV. EXPERIMENTAL RESULTS

##### A. ALUMINUM OXIDE ( $\text{Al}_2\text{O}_3$ ) PRODUCTION AND CHARACTERIZATION

###### 1. Aluminum Oxide Production

Aluminum oxide powders were prepared by the following reaction:



The reaction free energy and equilibrium constant were calculated over the temperature range 500-2000°K. The thermodynamic data are summarized in Table V.

The growth conditions for the formation of aluminum oxide are given in Table VI. Aluminum chloride was generated as discussed previously. Weight-loss measurements on the source aluminum indicated a chlorination efficiency of 80-95 per cent for the various runs.

Reactant gases were admitted to the reaction chamber through a central injector nozzle. The reaction chamber was a horizontal alumina tube, 38 millimeters in diameter. The tube was heated in a molybdenum-wound, hydrogen-protected furnace. Gases were reacted in a 10-cm long isothermal zone. Aluminum oxide powders nucleated and grew during residence in the isothermal zone, beyond which they deposited on the tube walls. Samples were carefully selected from various regions within the tube for characterization.

###### 2. Aluminum Oxide Characterization

The crystalline phases in the powder samples were identified with x-ray diffraction (see Appendix C). In all samples, the principal phases were transition aluminas, predominantly gamma and delta. Alpha alumina (corundum) was present as a secondary phase. Traces of unreacted aluminum chloride were observed in a few samples collected near the cold end of the tube where the temperature would permit deposition of aluminum chloride.

The particle size of the powder samples was determined by lineal analysis of electron micrographs. Several typical micrographs are shown in Figs. 14-17.

Comparing the particle sizes of Table VI with the growth conditions for each run, several trends are apparent.

Table V - Free-Energy Changes and Equilibrium Constants as a Function of Temperature for Aluminum Oxide Production

T (°C)	T (°K)	$\Delta G^\circ$ Reaction 13* (Kcal/mole)	$K_p$ Reaction 13*
227	500	-63.3	$3.3 \times 10^{27}$
727	1000	-75.8	$3.0 \times 10^{16}$
927	1200	-80.2	$3.4 \times 10^{14}$
1127	1400	-85.4	$1.8 \times 10^{13}$
1227	1500	-87.6	$5.0 \times 10^{12}$
1327	1600	-90.5	$2.0 \times 10^{12}$
1427	1700	-92.6	$6.9 \times 10^{11}$
1527	1800	-94.6	$2.7 \times 10^{11}$
1627	1900	-97.4	$1.4 \times 10^{11}$
1727	2000	-100.0	$7.4 \times 10^{10}$

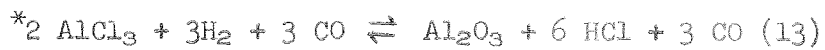


Table VI - Conditions for Aluminum Oxide Powder Production

Run No.	Flow Conditions (cc/min)						P <sub>Total</sub> (Torr)	Temp. (°C)	Particle Size (μ)
	H <sub>2</sub>	CO <sub>2</sub>	CO	Cl <sub>2</sub> xs	Cl <sub>2</sub>	Al			
VA-2	1000	200	-	-	30		15	1500	~ 0.01
VA-3	1000	200	-	-	30		200	1500	~ 0.01
VA-4	1000	200	-	-	40		350	1500	~ 0.01
VA-6	950	800	100	20	40		100	1750	0.05
VA-8	950	800	100	20	70		340	1700	0.07
								1750	
								1800	
								1850	
VA-9	950	800	100	20	70		260	1850	0.18
VA-10	600	500	210	45	50		660	1800	0.13
VA-13	100	100	-	-	80		50	1700	0.02
VA-15	100	100	-	-	80		100	1750	0.09
VA-16	50	50	-	-	40		50	1750	0.05
VA-17	100	100	-	-	80		200	1750	0.12
VA-18	50	50	-	-	40		50	1600	0.14

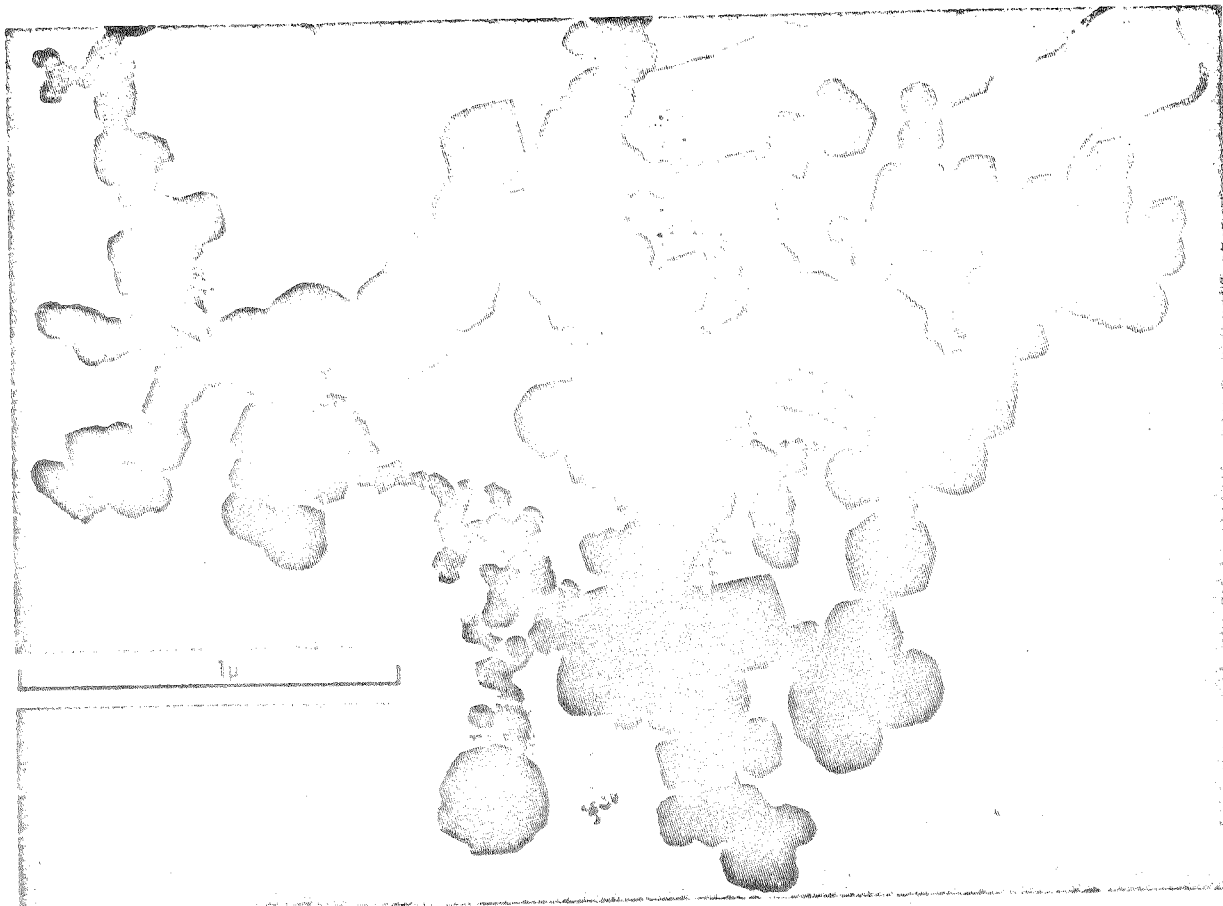


Fig. 14 - Electron Photomicrograph of Alumina Powder, 67,200X

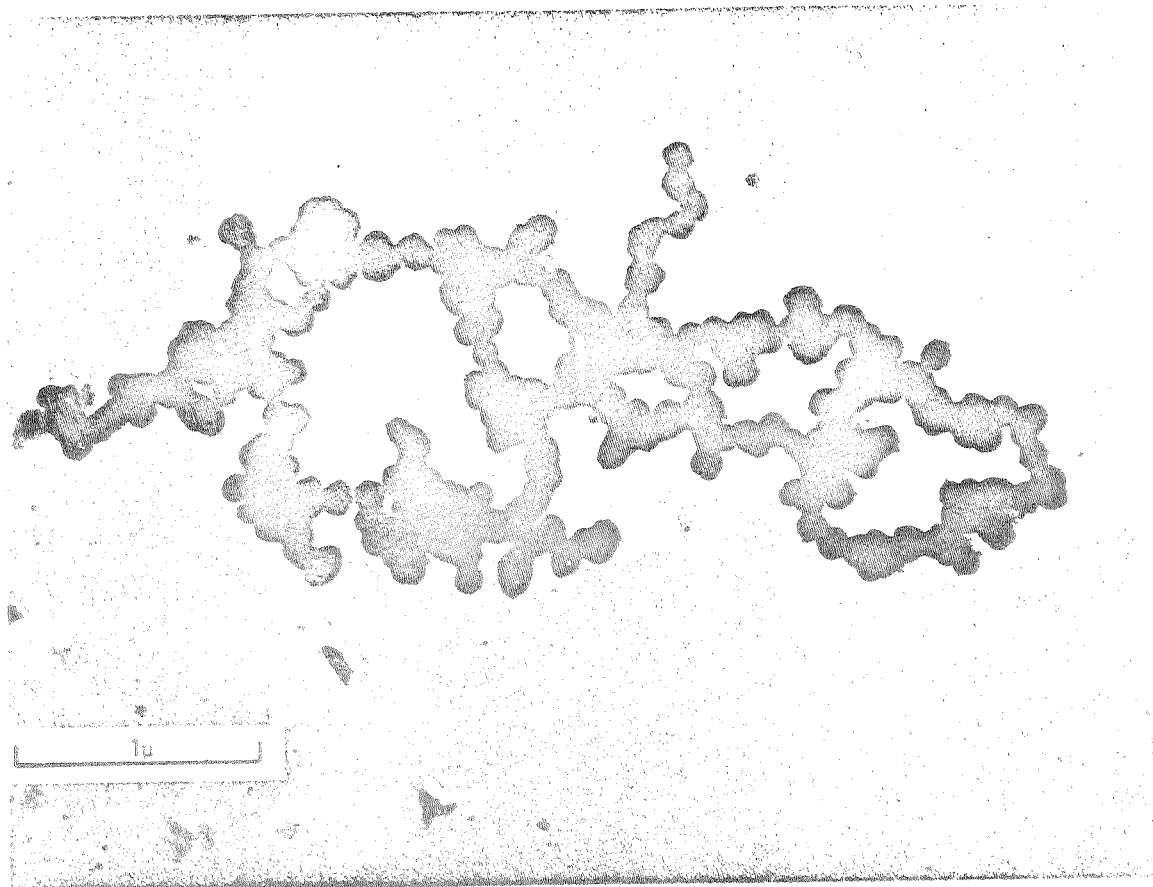


Fig. 15 - Electron Photomicrograph of Alumina Powder, 43,400X

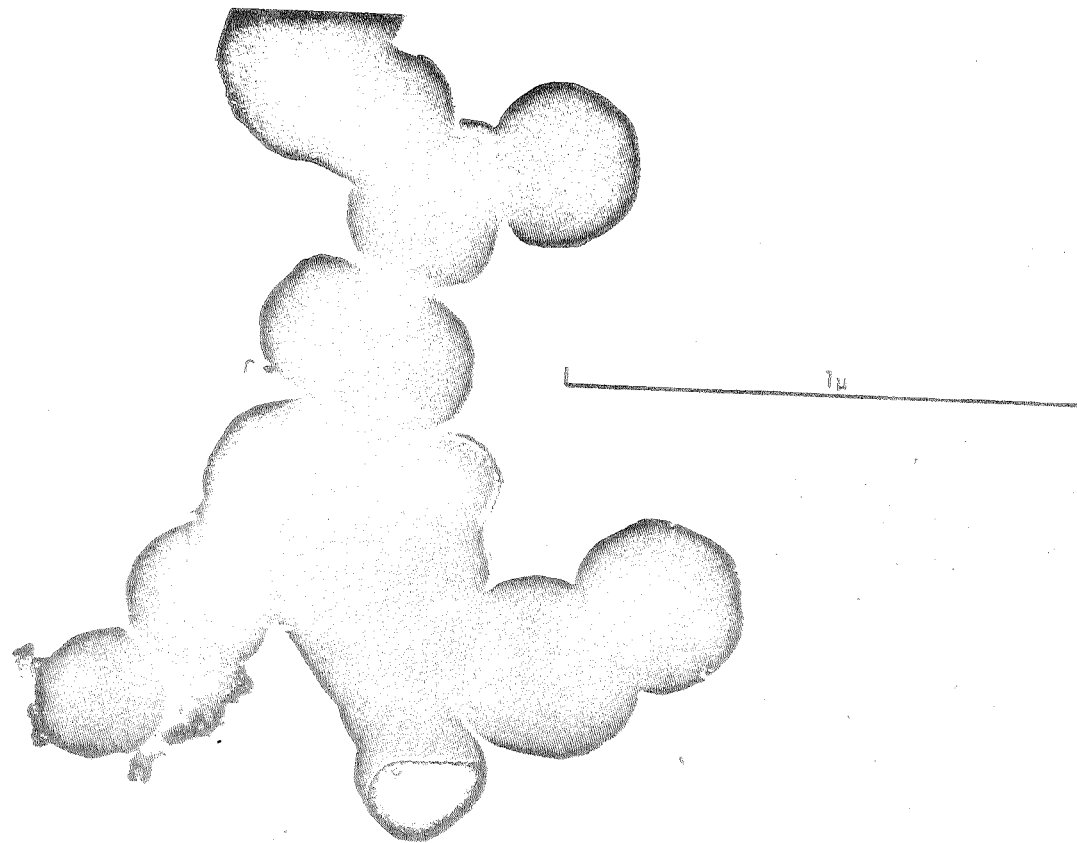


Fig. 16 - Electron Photomicrograph of Alumina Powder, 92,000X



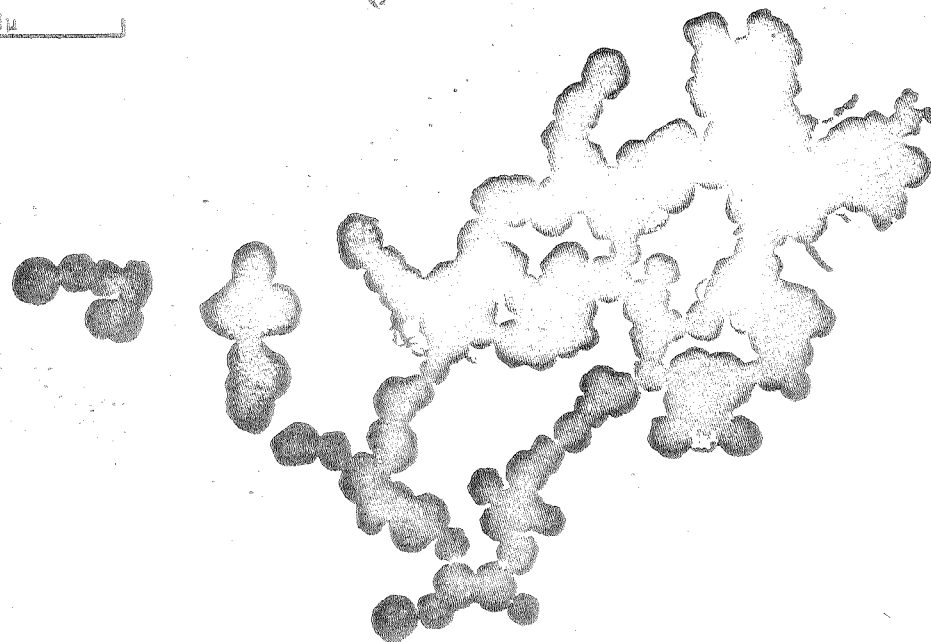


Fig. 17 - Electron Photomicrograph of Alumina Powder, 43,400X

The effect of changes in system pressure on the produced powder can be seen by comparing Run No. VA-15 with Run No. VA-17. In general, increasing system pressure decreases the gas velocity in the reaction chamber, allowing first a longer time for gas mixing and heat transfer in the reactor entrance, and second a longer residence time for powder growth in the hot zone. The effect of increased heat transfer to the gas stream and increased mixing should result in increased efficiency of conversion.

This was substantiated by the increased amount of powder produced at higher pressures. In addition, the increase in residence time in the hot zone should result in an increase in average particle size. The increase in size from  $0.09\mu$  for Run No. VA-15 to  $0.12\mu$  for Run No. VA-17 verified this assumption.

To determine the effect of temperature upon particle size, temperature was varied in VA-8 from  $1700^{\circ}\text{C}$  to  $1850^{\circ}\text{C}$ , in  $50^{\circ}\text{C}$  increments. The particle size distribution of the resulting powders was much wider than that obtained at fixed conditions. A range from 0.01 to  $0.20\mu$  was observed with an average particle size of  $0.07\mu$ . From a probability plot of particle size versus percent finer (Fig. 18), the particle size distribution appeared to be a sum of several individual normal distributions. The results of VA-9 indicate that the large size of VA-8 can be attributed to the higher temperatures.

However, upon comparing VA-16 with VA-18, it is apparent that a decrease in temperature resulted in considerable increase in particle size for these particular input gas conditions. Thus, the effect of temperature on particle size is not precisely defined from the results of these experiments.

Comparing the results of VA-15 with VA-16, the effect on particle size of the number of moles input is apparent. Doubling the inputs and simultaneously doubling system pressure to maintain the same gas velocity results in approximately a two-fold increase in particle size from  $0.05\mu$  to  $0.09\mu$ . Thus growth appears to be directly related to the availability or concentration of the growth species.

## B. TITANIUM DIOXIDE ( $\text{TiO}_2$ ) POWDER PRODUCTION AND CHARACTERIZATION

### 1. Titanium Dioxide Powder Production

Two runs were made to produce titanium dioxide (rutile) powder. The powder was formed by the following chemical reaction and the subsequent homogeneous nucleation of rutile:



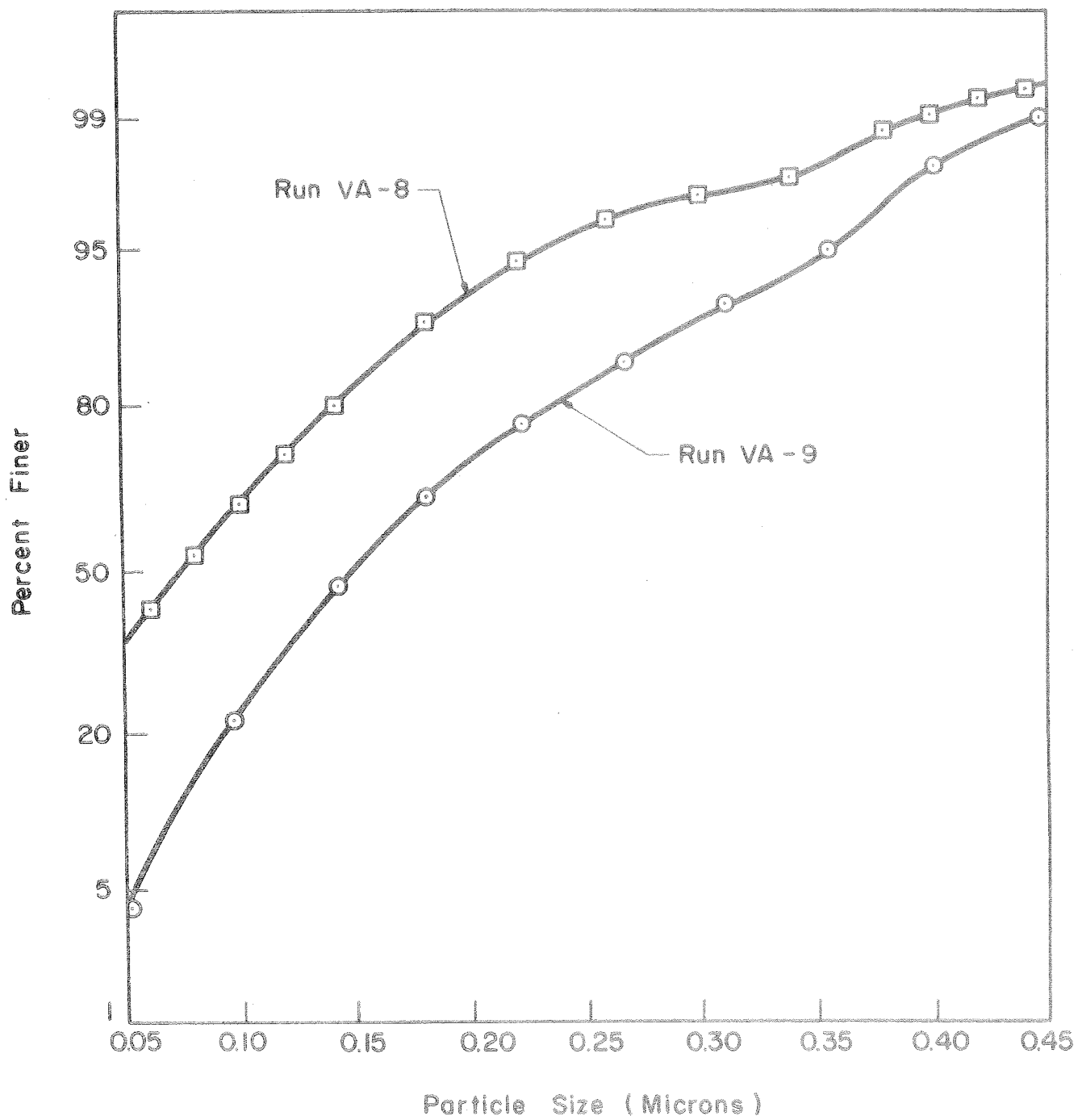


Fig. 18 - Particle Size Probability Plot of Alumina Powders

The free energy change for reaction (14) was calculated over the temperature range of 300 to 2000°K. The thermodynamic values are reported in Table VII. Reaction (14) had a substantial negative free energy change for all temperatures.

Titanium tetrachloride for the reaction was described earlier. The reaction zone temperature was maintained at 1350°C and system pressure at 210 mm Hg. The titanium chlorinator was maintained at 400°C and the transfer line at 350°C. See Table VIII for gas flow rates.

Run TiO<sub>2</sub>-1 flow rates were set to produce as near stoichiometric flows as possible while run TiO<sub>2</sub>-2 had a slight excess of H<sub>2</sub> and CO<sub>2</sub>.

Theoretical titanium weight loss was calculated from chlorine flow rates and duration of the run, assuming complete conversion of chlorine to titanium tetrachloride. A weight analysis of titanium was made after each run and it was determined that in run TiO<sub>2</sub> the titanium weight loss was 18 per cent of the calculated theoretical loss. In run TiO<sub>2</sub>-2, titanium weight loss was 21 per cent of theoretical. Efficiency of chlorination may have been higher than the reported 18 and 21 per cents because a portion of weight of the titanium after a run may have resulted from chemically absorbed chlorine.

## 2. Titanium Dioxide Powder Characterization

In both runs, small quantities of a white powder were deposited above the reaction zone and in the outlet tee. Small specks of gray powder were dispersed through the white powder in run TiO<sub>2</sub>-1; in run TiO<sub>2</sub>-2, CO<sub>2</sub> flow rates were increased in an effort to prevent formation of the gray material. However, run TiO<sub>2</sub>-2 appeared identical to run TiO<sub>2</sub>-1.

X-ray diffraction analyses of the powder from both runs, using both diffractometer and powder camera methods, showed the material to be rutile. No other phases were detectable. The gray powder formed was believed to be nonstoichiometric rutile (see Appendix D for x-ray diffraction patterns and powder camera film).

Inspection of the rutile by electron microscopy showed the rutile to have well-developed morphology in many of the particles, as shown in Figs. 19-22. The rutile particles appeared to be single crystals because of their morphology. Lineal analyses of the particles by electron micrographs showed the rutile to have an average particle size of 0.7μ, with the majority of the particles between 0.1- and 1.0μ. The particle size distribution determined by electron microscopy, is given in Fig. 23. The electron microscopy particle size analysis was substantiated using x-ray line broadening, which gave average particle size normal to the (110), (101), and (111) planes of 0.09, 0.6, and 0.6μ, respectively.

Table VII - Free-Energy Changes and Equilibrium Constants as a Function of Temperature for Titanium Dioxide Production

T (°C)	T (°K)	$\Delta G^\circ$ Reaction 14* (Kcal/mole)	$K_p$ Reaction 14*
27	300	- 4.60	$2.25 \times 10^3$
127	400	-10.55	$5.82 \times 10^5$
227	500	-17.15	$3.14 \times 10^7$
327	600	-18.20	$4.27 \times 10^8$
427	700	-21.85	$6.64 \times 10^8$
527	800	-25.45	$8.98 \times 10^8$
627	900	-28.90	$1.04 \times 10^7$
727	1000	-32.10	$1.04 \times 10^7$
827	1100	-35.55	$1.16 \times 10^7$
927	1200	-39.39	$1.49 \times 10^7$
1027	1300	-42.30	$1.29 \times 10^7$
1127	1400	-45.90	$1.46 \times 10^7$
1227	1500	-49.15	$1.45 \times 10^7$
1327	1600	-53.25	$1.88 \times 10^7$
1427	1700	-56.45	$1.81 \times 10^7$
1527	1800	-60.60	$2.28 \times 10^7$
1627	1900	-64.50	$2.63 \times 10^7$
1727	2000	-67.40	$2.32 \times 10^7$



Table VIII - System Conditions for Rutile Powder Production

Run No.	System Pressure (mm Hg)	Hot Zone Temperature (°C)	Cl <sub>2</sub> to Ti (cc/min at 25 psig)	H <sub>2</sub> (cc/min at 5 psig)	CO <sub>2</sub> (cc/min at 5 psig)
TiO <sub>2</sub> -1	210	1350	75	150	100
TiO <sub>2</sub> -2	210	1350	75	200	150

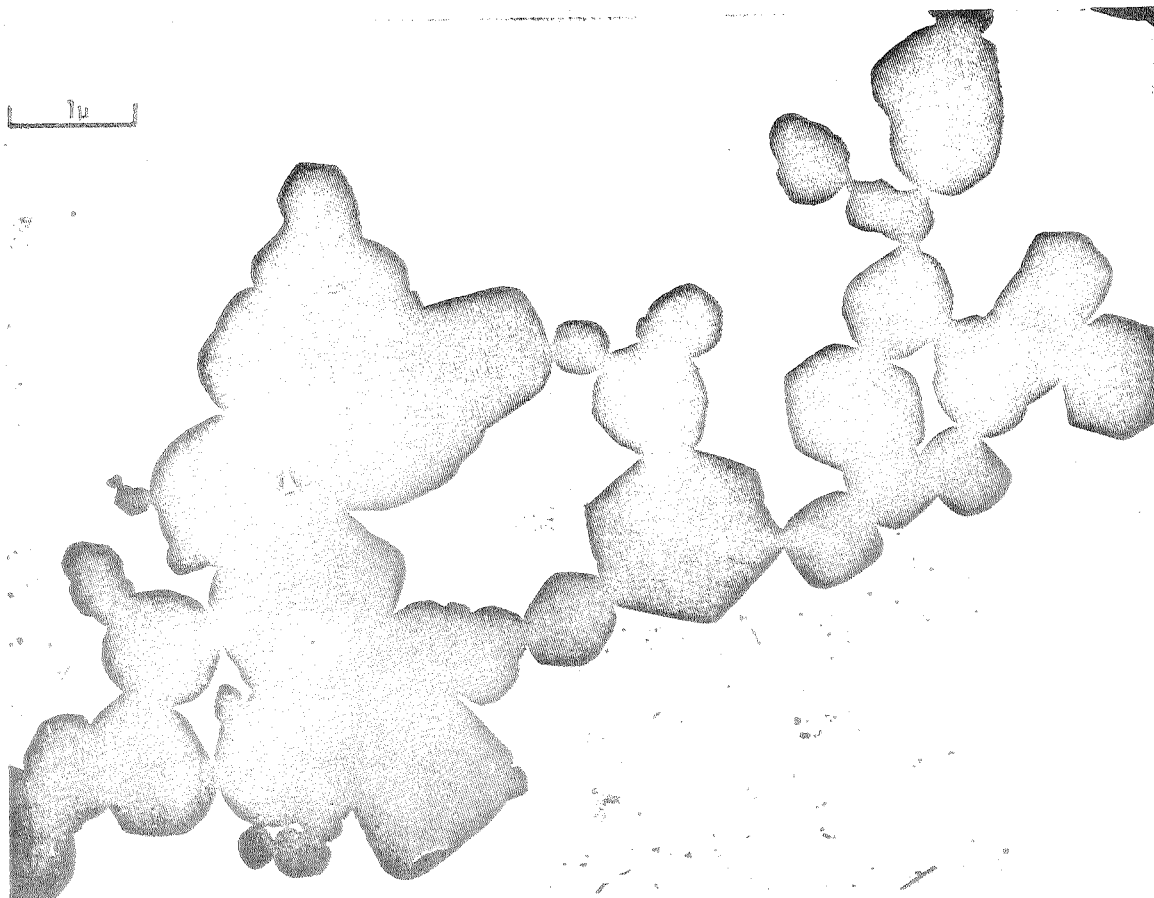


Fig. 19 - Electron Photomicrograph of Rutile Powder, Run TiO<sub>2</sub>-1,  
22,400X

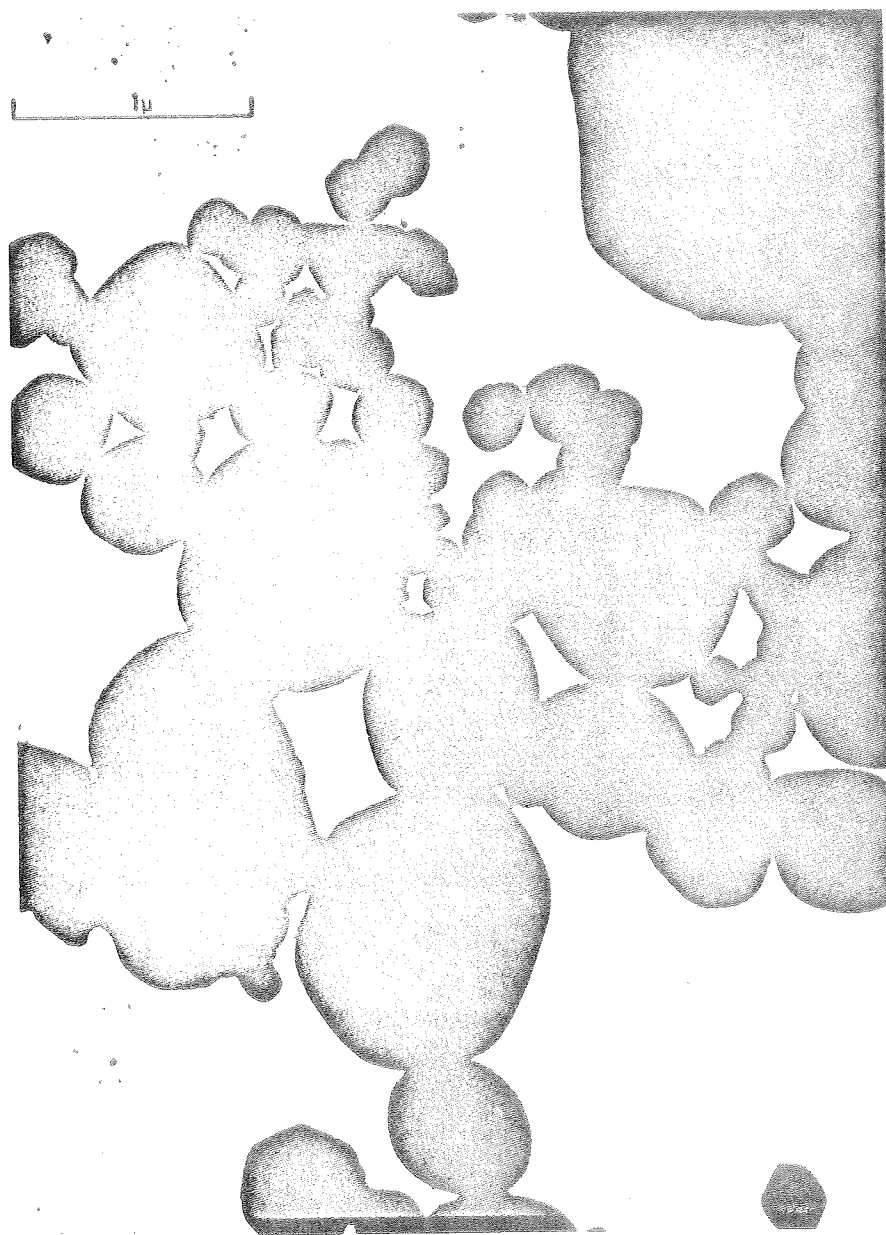


Fig. 20 - Electron Photomicrograph of Rutile Powder, Run  $\text{TiO}_2$ -1,  
42,400X

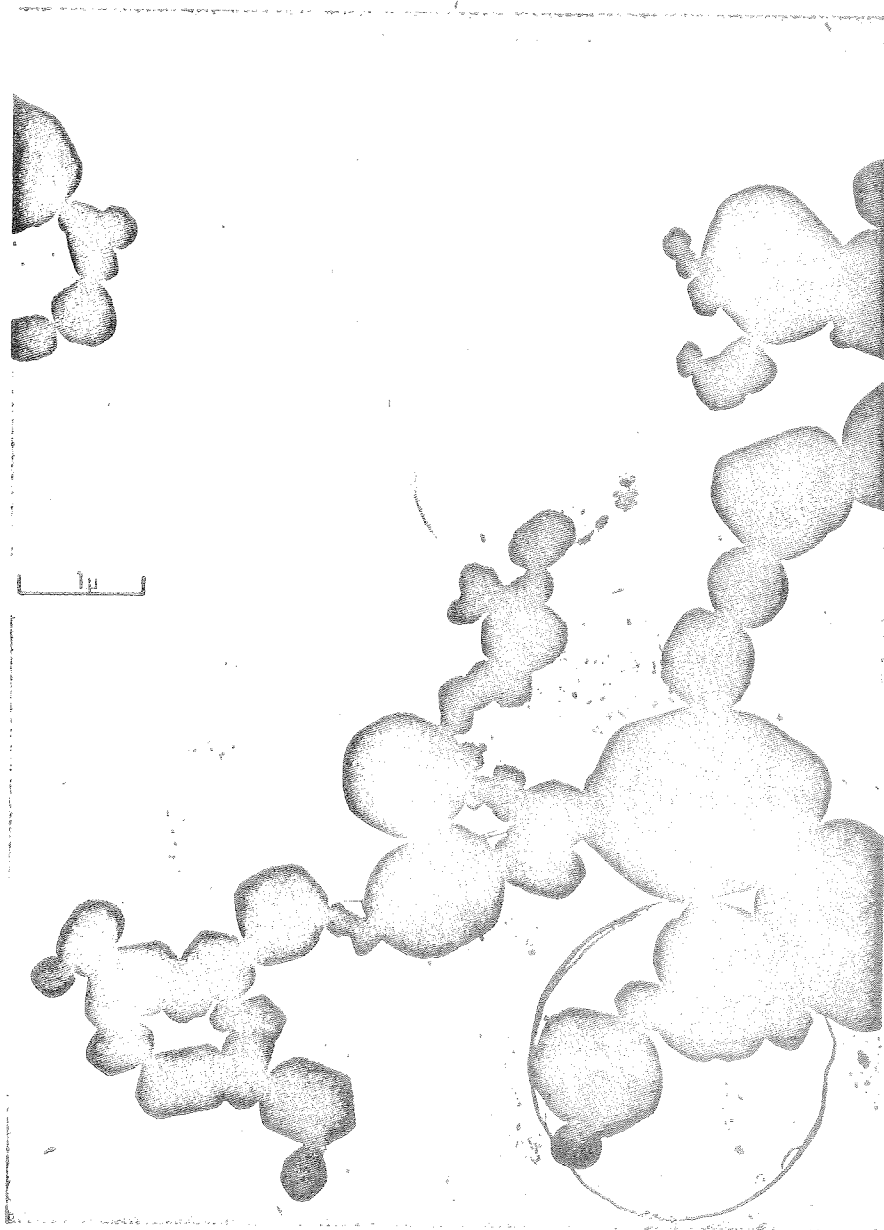


Fig. 21 - Electron Photomicrograph of Rutile Powder, Run  $\text{TiO}_2$ -1,  
22,400X



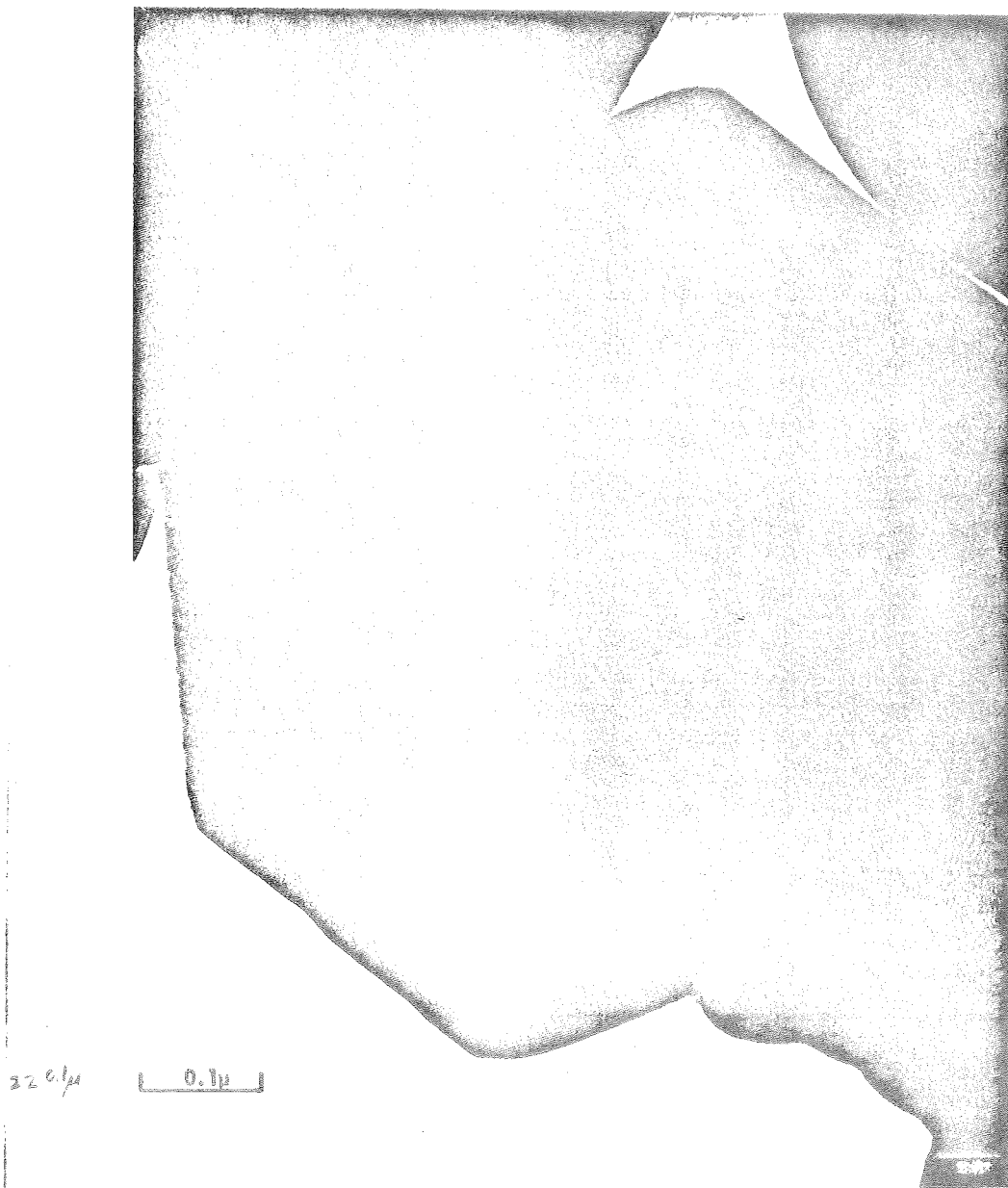


Fig. 22 - Electron Photomicrograph of Rutile Powder, Run TiO<sub>2</sub>-2,  
220,000X

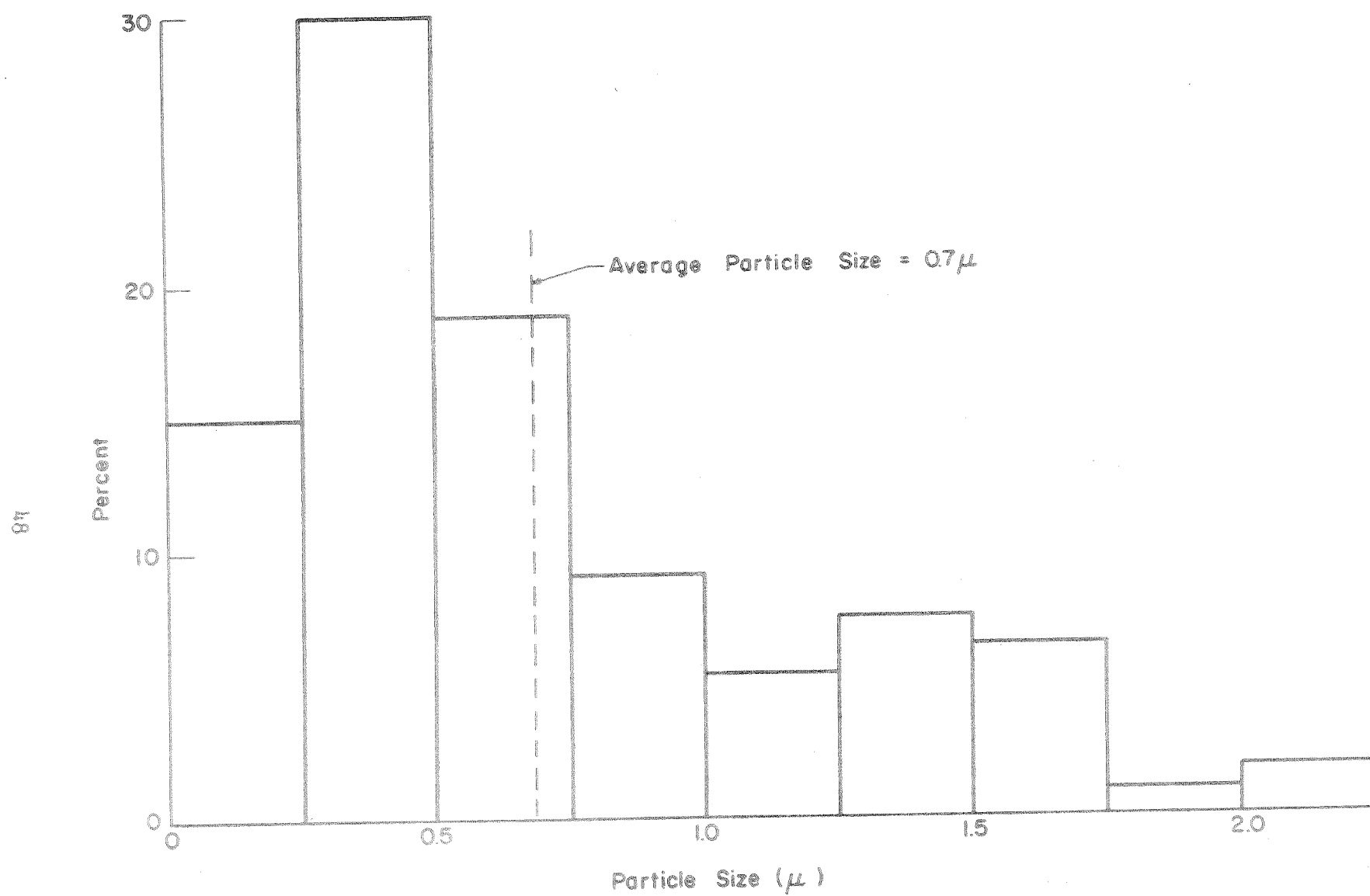


Fig. 23 - Particle Size Distribution of Vapor Grown Rutile

C. ZINC ORTHOTITANATE ( $\text{Zn}_2\text{TiO}_4$ ) POWDER  
PRODUCTION AND CHARACTERIZATION

1. Using Zinc Metal as the Zinc  
Vapor Species

Zinc orthotitanate powder was produced from homogeneous nucleation of gases following the chemical reaction represented in Eq. (4). Eight runs were made using vaporization of metallic zinc as the zinc vapor species. The conditions for these runs are shown in Table IX. The Zn/Ti ratio shown in Table IX is the ratio of the number of moles of Zn to number of moles of Ti that were introduced into the system during the run. For stoichiometric  $\text{Zn}_2\text{TiO}_4$ , the Zn/Ti ratio should be 2.0.

a. Zinc Vaporization - To establish the conditions for a controlled zinc evaporation rate, the system pressure was maintained at 50 mm Hg for all runs. The zinc temperature was varied from 500 to 600°C. The thermocouple measuring the zinc temperature was slightly off position and the recorded temperature was approximately 50°C lower than the actual temperature. This temperature difference was indicated by the observed melting of the metal which occurred at  $370 \pm 11^\circ\text{C}$  for the runs recorded; zinc melts at  $420^\circ\text{C}$ . Although the zinc temperature recorded was 50°C low, temperature measurement gave a relative and reproducible control for establishing zinc evaporation conditions. Zinc evaporation rates at 50 mm Hg system pressure is plotted versus temperature in Fig. 24. Because of gas flow rate variation it was difficult to establish a relation between evaporation rate and temperature; although in general, evaporation rate increased with temperature. Several factors may be responsible for poor control of zinc evaporation. The first and most probable factor was variation in zinc partial pressure. Note that Eq. (8) predicts increasing evaporation rate with decreasing zinc partial pressure. Even though the system pressure was maintained constant, variation of other gas flow rates caused a variation in zinc partial pressure. Increasing gas flow rates would decrease zinc partial pressure and increase zinc evaporation rate. This was indicated in runs 2, 6, and 7 where zinc temperatures were fairly close and zinc evaporation seemed to be controlled by zinc partial pressure. The second factor responsible for poor zinc evaporation was reduction of zinc evaporation surface area because of powders settling on the evaporation surface. This could not be controlled and the magnitude of the effect could not be determined for the runs made. Other control variations resulted from slight variation in system pressure and zinc temperature, although it is not believed that significant enough variation occurred in these two factors to produce the observed zinc evaporation rate variation. Because of the above difficulties, later runs were made using zinc chloride as the zinc vapor species.

Table IX - System Conditions and Phase Analysis for Runs Using Metallic Zinc as the Zinc Vapor Species

Run No.	Reaction Zone Temperature (°C)	Gas Flow Rates			Zinc Evaporation Rate (grams/min)	Zinc Temperature (°C)	Zn/Ti Ratio
		Cl <sub>2</sub> to Ti	H <sub>2</sub>	CO <sub>2</sub>			
		(cc/min at 25 psig)	(cc/min at 5 psig)	(cc/min at 5 psig)			
Zn <sub>2</sub> TiO <sub>4</sub> -							
1	1200	85	168	336	2.0	600	7.8
2	1200	100	200	400	0.40	575	1.1
3	1400	90	200	400	0.16	500	0.6
4	1040	27	570	111	0.12	540	1.3
5	1100	100	500	1000	—*	600	—
6	1300	95	300	600	0.75	560	2.6
7	1350	100	300	1600	1.90	570	5.6
8	1300	100	2000	1600	0.67	520	1.9

System Pressure (mm Hg)	Phase Analysis and Color of Powder						
	Zone 1		Zone 2		Zone 3		
	Phases	Color	Phases	Color	Phases	Color	
1	50	Not Analyzed	Not Analyzed		(1) Zn <sub>2</sub> TiO <sub>4</sub> (2) TiO <sub>2</sub> (3) ZnO	light gray	
2	50	Not Analyzed	TiO <sub>2</sub>	white	(1) ZnO (2) TiO <sub>2</sub> (3) Zn <sub>2</sub> TiO <sub>4</sub>	white	
3	50	Not Analyzed	Not Analyzed		(1) TiO <sub>2</sub> (2) ZnO (3) Zn <sub>2</sub> TiO <sub>4</sub> Trace (4) ZnTiO <sub>3</sub> Trace	white	
4	50	Not Analyzed	Not Analyzed		(1) TiO <sub>2</sub> (2) ZnTiO <sub>3</sub>	light gray	
5	50	(1) Zn (2) ZnCl <sub>2</sub> (3) TiO <sub>2</sub>	dark gray	(1) Zn (2) ZnCl <sub>2</sub>	dark gray	(1) TiO <sub>2</sub> (2) ZnO Trace	light gray
6	50	Not Analyzed	Not Analyzed		(1) ZnO (2) Zn <sub>2</sub> TiO <sub>4</sub> (3) TiO <sub>2</sub> (4) Zn Trace (5) ZnTiO <sub>3</sub> Trace	light gray	
7	50	Not Analyzed	(1) ZnO (2) Zn <sub>2</sub> TiO <sub>4</sub> (3) TiO <sub>2</sub>	gray	(1) TiO <sub>2</sub> (2) ZnO (3) ZnTiO <sub>3</sub>	light gray	
8	50	Not Analyzed	Not Analyzed		(1) TiO <sub>2</sub> (2) ZnO (3) ZnTiO <sub>3</sub>	light gray	

\*All zinc evaporated due to variation in system pressure.

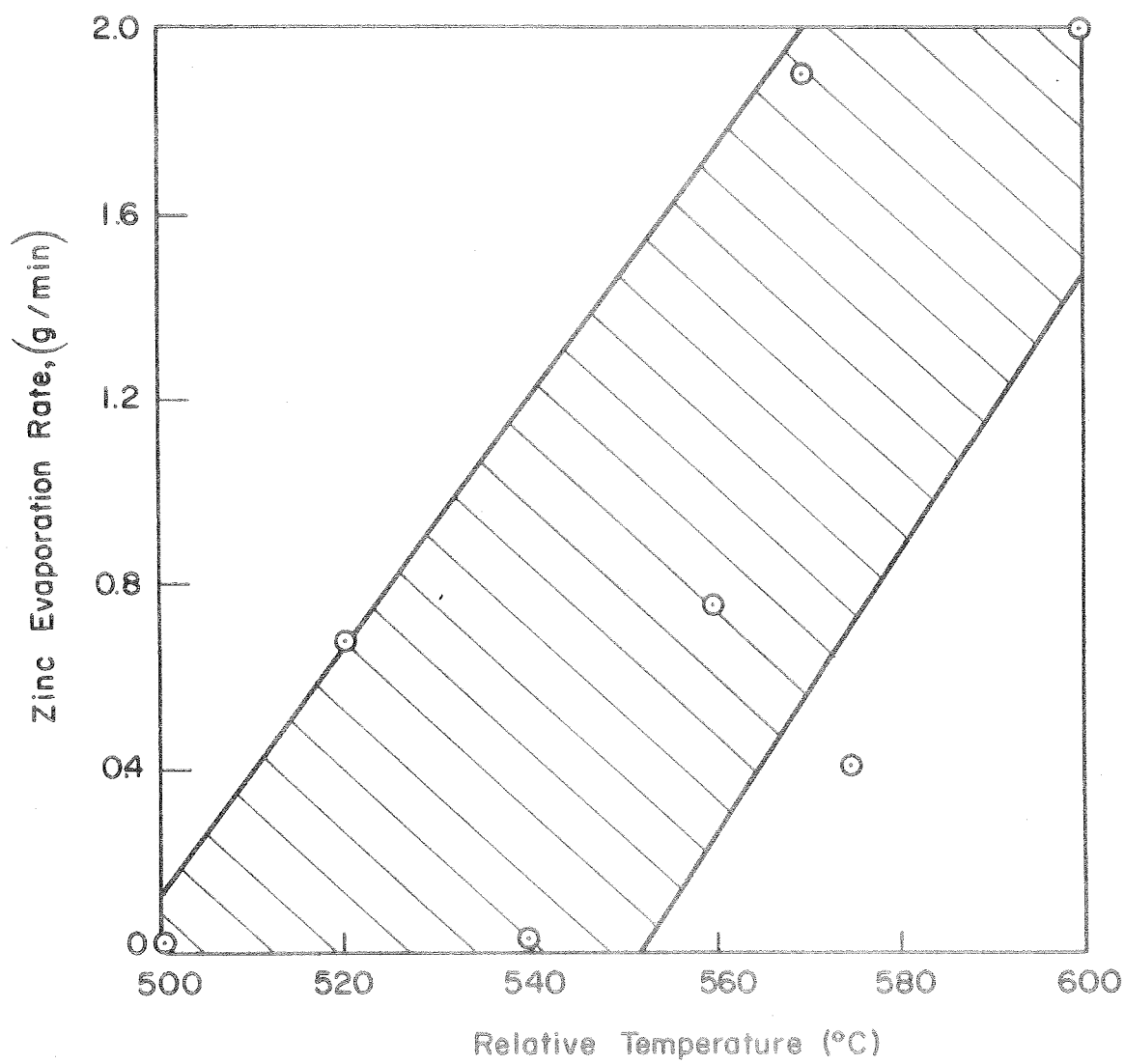


Fig. 24 - Zinc Evaporation Rate vs Temperature at 50 mm Hg

b. Powder Characteristics - In the majority of the runs, powder was deposited in three distinct zones in the reaction tube above the hot zone. The zones were (1) the top two inches of the reaction tube, Zone 1; (2) approximately 2-4 inches below the top of the reaction tube, Zone 2; and (3) from approximately 4 inches below the top of the reaction zone to the hot zone, Zone 3 (see Fig. 25 for sketch of zones). The zones were evidenced by color variation from zone to zone. According to visual evidence in most runs Zone 1 contained mainly metallic zinc which was powdery in nature and dark gray. Zone 2 contained large amounts of metallic zinc which condensed on the walls and flowed down the tube to the point that vaporization occurred again. Apparently the temperature of Zone 2 was in the range in which zinc is a liquid. The major portions of the oxides were found in Zone 3 and were evidenced by a light gray to white color. In no run was  $\text{Zn}_2\text{TiO}_4$  the only oxide formed and in all runs  $\text{TiO}_2$  and  $\text{ZnO}$  were found mixed with the  $\text{Zn}_2\text{TiO}_4$ . The results of x-ray diffractometer phase analysis (see Appendix E) as well as material color for the different portions of the tube are listed in Table IX. The phases indicated in Table IX are listed in order of peak height to give an indication of relative amounts of phases found. The results of regions left blank does not indicate a lack of material deposited in those regions but simply that these regions were not analyzed, for in every run a significant portion of the material formed from the vapor phase was found in Zones 1 and 2. In every run the materials in Zones 1 and 2 were gray to black in color and in most cases contained large amounts of metallic zinc which could be easily seen.

In four of the runs  $\text{Zn}_2\text{TiO}_4$  was formed and in one run (#1) it was found to be the most abundant phase in Zone 3. Figures 26 and 27 are electron micrographs of run  $\text{Zn}_2\text{TiO}_4$ -1, Zone 3. Although the characteristic morphology of  $\text{Zn}_2\text{TiO}_4$  is not known and therefore cannot be determined from the mixed phases in the micrographs, the micrographs do show a particle size in the 0.1 to 1.0  $\mu$  regions, as was evidenced in the rutile electron micrographs presented earlier. The characteristic hexagonal morphology shown by rutile in earlier micrographs can be seen in the micrographs of Figs. 26 and 27.

Although other oxide phases were formed besides  $\text{Zn}_2\text{TiO}_4$ , its presence in some of the runs indicates that reaction (4) was proceeding, at least to a partial degree. There are several possible explanations for formation of multiple oxide phases. The first is lack of control of Zn evaporation rate and incomplete chlorination of titanium. In runs  $\text{Zn}_2\text{TiO}_4$ -8,9 and 10, 29 per cent of the theoretical titanium weight was low. However, the efficiency may have been higher because chemically reacted chlorine on the surface of the titanium would have masked the true weight loss of the titanium after the run.

The second, and most probable explanation, is lack of mixing of the Zn vapor which flowed outside the central injection nozzle with the gases flowing through the central injection nozzle. The Reynolds

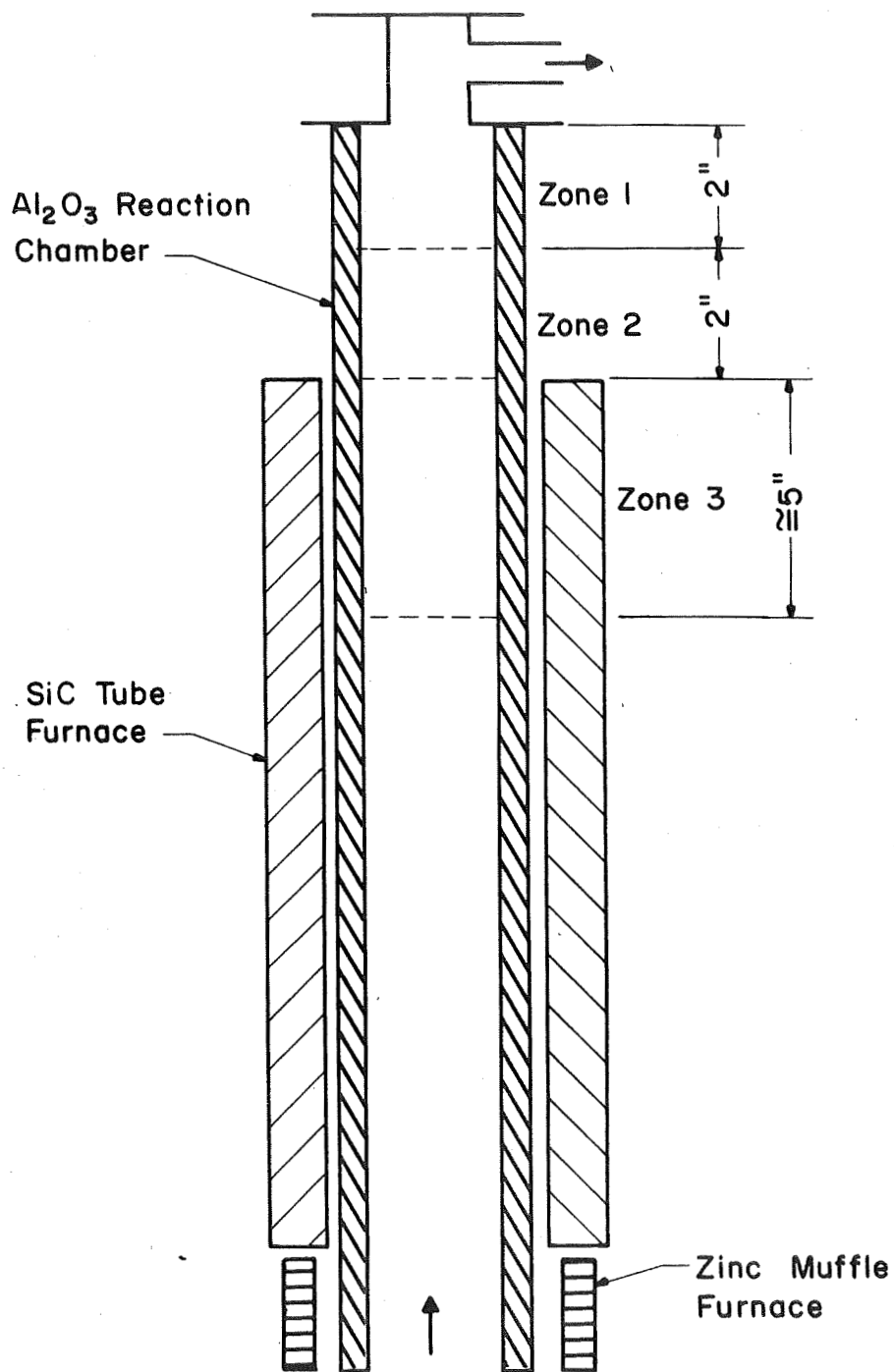


Fig. 25 - Schematic of Powder Deposition Zones

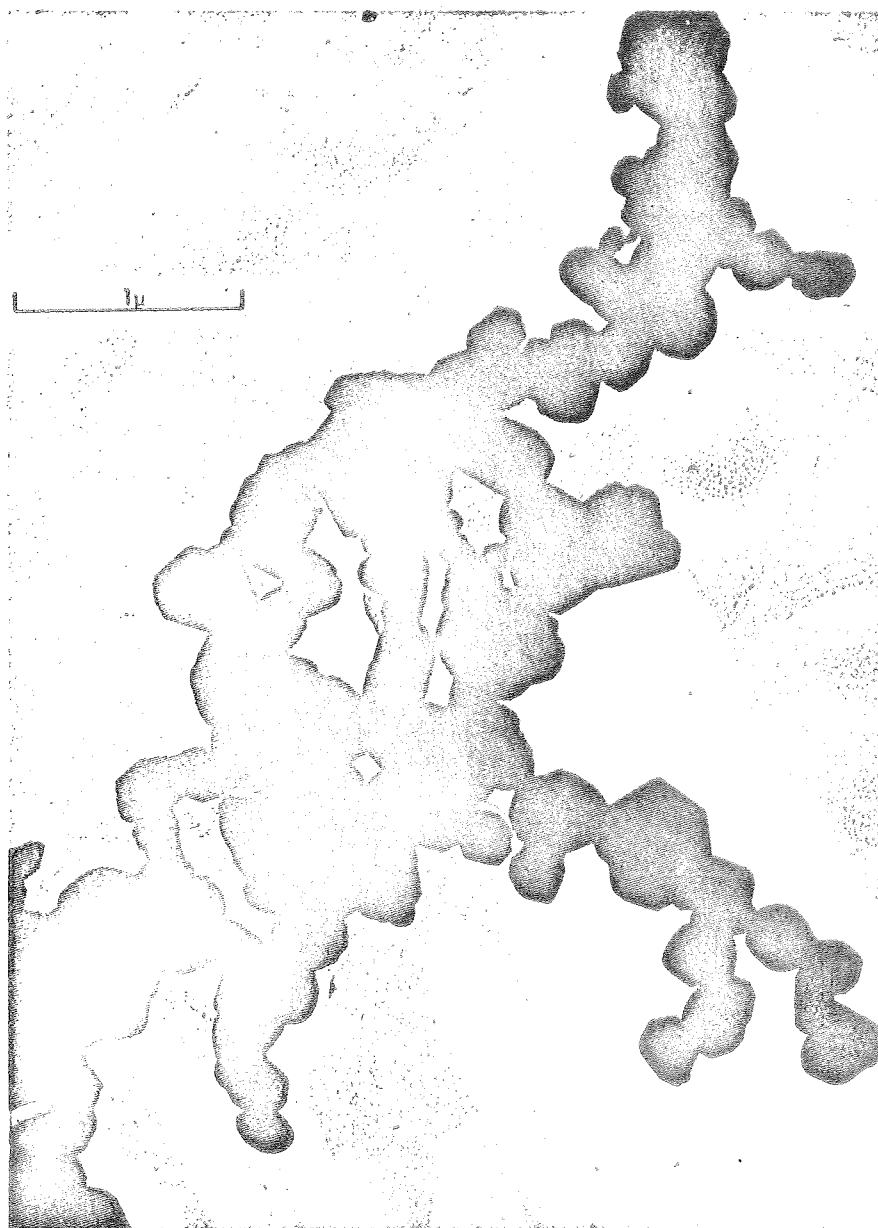


Fig. 26 - Electron Photomicrograph, Run  $\text{Zn}_2\text{TiO}_4$ -1, Zone 3, 40,000X



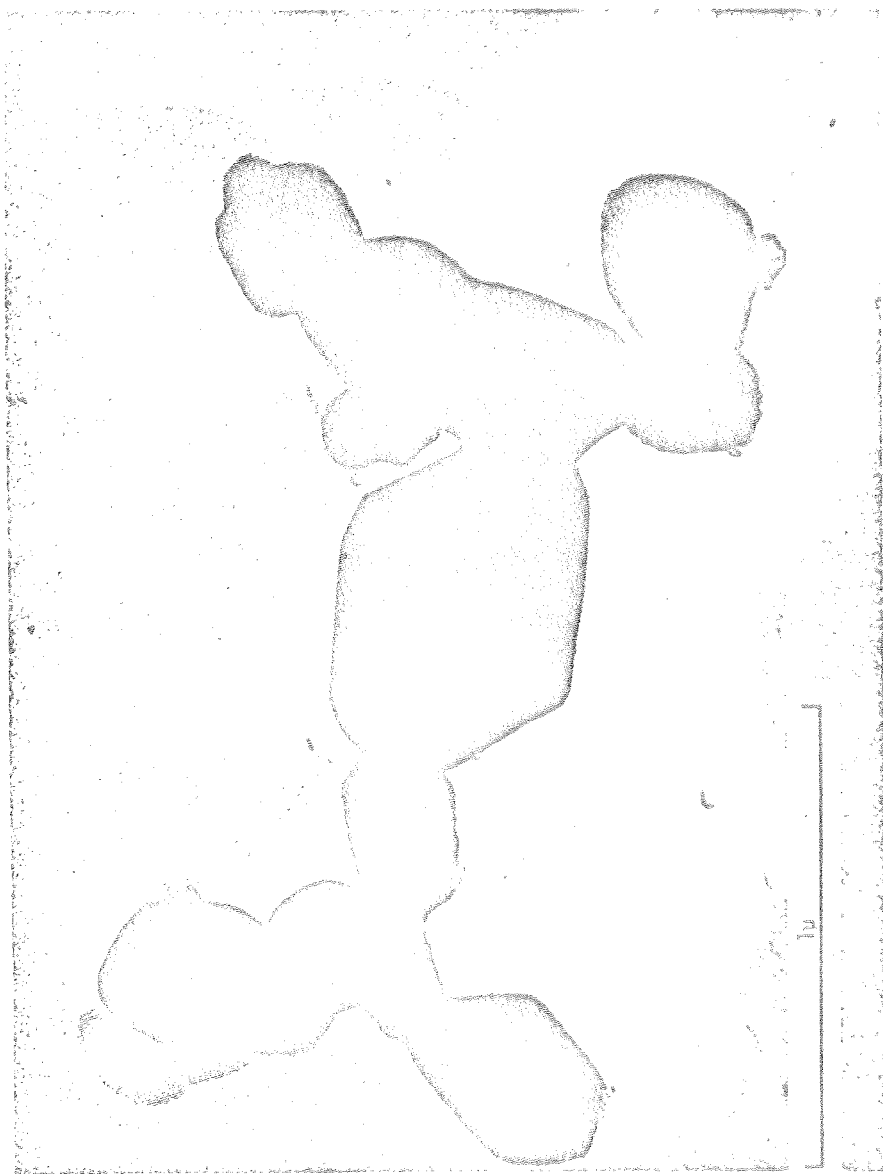


Fig. 27 - Electron Photomicrograph, Run  $\text{Zn}_2\text{TiO}_{4-1}$ , Zone 3, 82,000X

number calculated for run  $\text{Zn}_2\text{TiO}_4$ -8 for gas flow through the hot zone was 60. This indicates laminar flow and results in poor mixing conditions. Therefore, there was probably a concentration gradient across the tube, with a high Zn concentration near the outside and a high  $\text{TiCl}_4$  concentration in the center. As the oxides formed,  $\text{TiO}_2$  was formed in the central portion of the reaction tube and  $\text{ZnO}$  was formed near the outside;  $\text{Zn}_2\text{TiO}_4$  formed in the boundary region between the two parallel gas streams.

## 2. Using Zinc Chloride as the Zinc Vapor Species

Formation of  $\text{Zn}_2\text{TiO}_4$  from homogeneous nucleation in the vapor phase was attempted in these experiments using general Eq. (5).  $\text{ZnCl}_2$  was used as the zinc vapor species and was formed according to Eq. (10) from the chlorination of  $\text{ZnO}$ . The apparatus was the same as used in previous runs except  $\text{ZnO}$  was placed in the position formerly occupied by the zinc vaporization crucible and the  $\text{Cl}_2$  and  $\text{CO}$  (for  $\text{ZnO}$  chlorination), as well as  $\text{CO}_2$ , were injected into the system at the bottom of the reaction tube below the  $\text{ZnO}$  and outside the central injection nozzle.  $\text{TiCl}_4$  and  $\text{H}_2$  were transferred into the system through the central injection nozzle.

System condition for the  $\text{ZnCl}_2$  runs are summarized in Table X. The gas flow gases were operated at 25 psig and 0 psig for chlorine and at 5 psig and 0 psig for the other gases to provide a greater range of gas flows.

a. Zinc Chloride Production - Zinc oxide was chlorinated according to Eq. (10). The oxygen liberated in the chlorination reaction was utilized to supply oxygen to the system by reacting  $\text{CO}$  with the liberated oxygen giving  $\text{CO}_2$ . The temperature of the zinc oxide in the chlorination zone of the reaction chamber was maintained above  $700^\circ\text{C}$  in all runs. The chlorination efficiency (Table X) varied from 46 to 100%. The highest efficiencies were obtained when using the 0 psig chlorine flow; 70, 100, and 99% efficiencies for runs  $\text{Zn}_2\text{TiO}_4$ -14, 15 and 18; while the maximum efficiency obtained using the 25 psig flow was 61%. Perhaps the higher flow rates (number of moles of chlorine per minute) produced when using the 25 psig flow were too rapid for complete chlorination of the zinc oxide. Because of the chlorination efficiencies obtained, chlorination of  $\text{ZnO}$  is a controllable method of introducing  $\text{ZnCl}_2$  into the system.

b. Zinc Orthotitanate Powder Characteristics - Powder in runs  $\text{Zn}_2\text{TiO}_4$ -12 through 18 was deposited on the walls of the reaction tube much the same as in the  $\text{Zn}_2\text{TiO}_4$  runs using zinc evaporation. The transition region between Zones 1 and 2 were not as defined as was previously found, but large amounts of  $\text{ZnCl}_2$  were deposited in Zones 1 and 2 where metallic Zn was previously found. The main portions of the

Table X - System Conditions and Phase Analysis for Runs Using Zinc Chloride as the Zinc Vapor Species

Material	Run No.	Reaction Zone Temperature (°C)	Gas Flow Rates									
			Cl <sub>2</sub> to ZnO		Cl <sub>2</sub> to TiO <sub>2</sub>		CO to ZnO		CO <sub>2</sub>		H <sub>2</sub>	
			Flow Gage Pressure (PSIG)	Flow Rate (cc/min)	Flow Gage Pressure (PSIG)	Flow Rate (cc/min)	Flow Gage Pressure (PSIG)	Flow Rate (cc/min)	Flow Gage Pressure (PSIG)	Flow Rate (cc/min)	Flow Gage Pressure (PSIG)	Flow Rate (cc/min)
ZnO	11	1300	25	40	25	0	5	80	5	0	5	80
Zn <sub>2</sub> TiO <sub>4</sub>	12	1300	25	50	25	50	5	100	5	100	5	200
Zn <sub>2</sub> TiO <sub>4</sub>	13	1300	25	50	25	50	5	100	5	100	5	200
Zn <sub>2</sub> TiO <sub>4</sub>	14	1430	0	45	0	45	0	100	0	100	0	100
Zn <sub>2</sub> TiO <sub>4</sub>	15	1400	0	38	0	38	0	90	0	100	0	130
Zn <sub>2</sub> TiO <sub>4</sub>	16	1480	25	50	25	50	0	17	0	17	0	233
Zn <sub>2</sub> TiO <sub>4</sub>	17	1450	25	40	25	40	0	100	0	100	0	200
Zn <sub>2</sub> TiO <sub>4</sub>	18	1700	0	45	0	45	0	100	0	100	0	100

Material	Run No.	System Pressure (mm Hg)	ZnO Chlorination Efficiency (%)	Phase Analysis		
				Zone #1	Zone #2	Zone #3
ZnO	11	210	46	Not Analyzed	Not Analyzed	(1) ZnO (2) ZnCl <sub>2</sub> 4Zn(OH) <sub>2</sub>
Zn <sub>2</sub> TiO <sub>4</sub>	12	100	53	ZnCl <sub>2</sub>	Not Analyzed	Nothing Analyzed
Zn <sub>2</sub> TiO <sub>4</sub>	13	200	61	ZnCl <sub>2</sub>	ZnCl <sub>2</sub>	TiO <sub>2</sub>
Zn <sub>2</sub> TiO <sub>4</sub>	14	100	70	ZnCl <sub>2</sub>	ZnCl <sub>2</sub>	TiO <sub>2</sub>
Zn <sub>2</sub> TiO <sub>4</sub>	15	90	100	ZnCl <sub>2</sub>	ZnCl <sub>2</sub>	TiO <sub>2</sub>
Zn <sub>2</sub> TiO <sub>4</sub>	16	200	48	(1) ZnCl <sub>2</sub> (2) TiO <sub>2</sub>	(1) ZnCl <sub>2</sub> (2) TiO <sub>2</sub>	(1) TiO <sub>2</sub> (2) ZnO (3) ZnTiO <sub>3</sub>
Zn <sub>2</sub> TiO <sub>4</sub>	17	300	57	(1) ZnCl <sub>2</sub> (2) TiO <sub>2</sub>	(1) TiO <sub>2</sub> (2) ZnTiO <sub>3</sub> (3) Trace ZnO (4) Trace Zn <sub>2</sub> TiO <sub>4</sub> or Zn <sub>2</sub> Ti <sub>3</sub> O <sub>8</sub> or both	(1) TiO <sub>2</sub> (2) ZnTiO <sub>3</sub> (3) ZnO
Zn <sub>2</sub> TiO <sub>4</sub>	18	200	99	(1) Zn (2) ZnCl <sub>2</sub> (3) TiO <sub>2</sub>	(1) Zn (2) ZnCl <sub>2</sub> (3) TiO <sub>2</sub>	(1) ZnO (2) TiO <sub>2</sub> (3) ZnTiO <sub>3</sub> (4) Trace Zn <sub>2</sub> TiO <sub>4</sub> or Zn <sub>2</sub> Ti <sub>3</sub> O <sub>8</sub> or both

oxides formed were deposited in Zone 3 and they consisted of mixtures of ZnO,  $\text{TiO}_2$  (rutile), and  $\text{ZnTiO}_3$ , with traces of  $\text{Zn}_2\text{TiO}_4$  or  $\text{Zn}_2\text{Ti}_3\text{O}_8$  or both. When  $\text{Zn}_2\text{TiO}_4$  and  $\text{Zn}_2\text{Ti}_3\text{O}_8$  are present in trace quantities it is difficult to distinguish between the two using x-ray diffraction since their diffraction patterns are similar. A phase analysis of the powder is given in Table X. Although chlorination of ZnO was controllable, the problem of forming multiple oxides remained. The major difficulty was believed to be lack of homogeneous mixing of the titanium and zinc vapor species because of the low gas flow rates in the laminar region.

## V. CONCLUSIONS AND RECOMMENDATIONS

### A. CONCLUSIONS

The following conclusions can be made concerning this first 10 months effort in the development and preparation of space-stable pigments for thermal control coatings:

#### 1. Aluminum Oxide Powder

- a. For constant reactant gas inputs and reaction zone temperature, increasing reaction zone pressure increases the average particle size of alumina powder.
- b. Increasing reactant gas inputs and increasing system pressure to maintain constant gas velocities at constant temperature increases the average particle size of alumina powder.
- c. The particle size range for the various alumina runs was 0.1 to 0.5 $\mu$ .

#### 2. Titanium Dioxide

Titanium dioxide (rutile) powder was produced with hexagonal morphology and an average particle size of 0.7 $\mu$ .

#### 3. Zinc Orthotitanate Powder

- a. Zinc orthotitanate powder was produced using vapor phase reactions of titanium tetrachloride and zinc vapor. However, zinc orthotitanate was not produced in a pure form but was mixed with zinc oxide, rutile, and zinc metatitanate.
- b. Zinc evaporation rates were difficult to control because of difficulties in controlling zinc partial pressure in the system.
- c. Chlorination of zinc oxide proved to be a controllable method of introducing zinc chloride into the reaction system.

- d. It is believed that a homogeneous mixture of the zinc and titanium reaction vapor species must be obtained before oxidation of the metals is initiated to prevent formation of multiple oxides.

## B. RECOMMENDATIONS FOR FUTURE EFFORT

### 1. Zinc Orthotitanate Powder

From analyses of previous zinc orthotitanate experiments it is believed that the following developments must be incorporated to produce more dispersed powders of zinc orthotitanate:

- a. Construct a double-stage chlorinator for chlorinating zinc oxide and then titanium dioxide to achieve a homogeneous mixture of zinc chloride and titanium tetrachloride before the chlorides enter the reaction zone, (see Fig. 28 for a sketch of the double-stage chlorinator design).
- b. Chlorinate the titanium dioxide by the following reaction:



Thermodynamic data for this reaction are summarized in Table XI and indicate that the reaction is favorable. Production of  $\text{TiCl}_4$  from  $\text{TiO}_2$  has been shown to be rapid above  $1000^\circ\text{C}$ .<sup>41,42</sup>

- c. To further improve the kinetics of reaction (5), a new silicon carbide reaction furnace will be constructed to provide a longer isothermal zone.

### 2. Lanthanum Oxide and Calcium Tungstate Powders

Free energy value and equilibrium constant calculations were made for a number of chemical reactions in the  $\text{La}_2\text{O}_3$  and  $\text{CaWO}_4$  systems using the previously mentioned computer program. Therefore, it is recommended that adequate process control be initiated to verify the favorability of the thermodynamics of the following reactions:



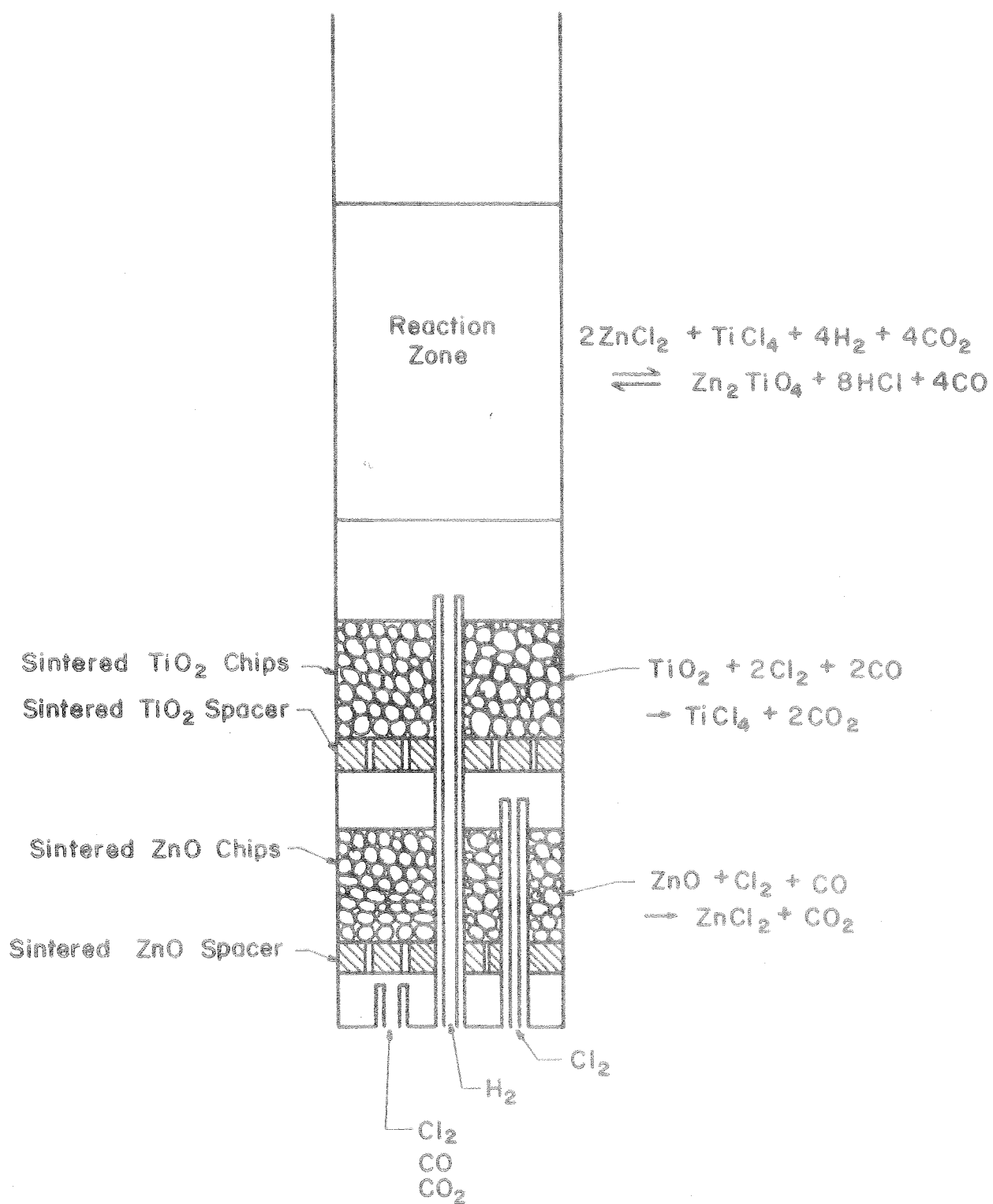


Fig. 28 - Double-Stage Chlorinator

Table XI - Free Energy Changes and Equilibrium Constants as a Function of Temperature for Titanium Dioxide Chlorination

T (°C)	T (°K)	$\Delta G^\circ$ Reaction 15* (Kcal/mole)	$K_p$ Reaction 15*
27	300	-86.40	$8.86 \times 10^{32}$
127	400	-81.25	$2.49 \times 10^{44}$
227	500	-78.45	$1.97 \times 10^{34}$
327	600	-75.40	$2.93 \times 10^{27}$
427	700	-72.55	$4.50 \times 10^{22}$
527	800	-69.55	$1.00 \times 10^{19}$
627	900	-66.70	$1.58 \times 10^{16}$
727	1000	-63.90	$9.26 \times 10^{13}$
827	1100	-61.05	$1.35 \times 10^{12}$
927	1200	-58.21	$4.00 \times 10^{10}$
1027	1300	-55.30	$1.98 \times 10^9$
1127	1400	-52.70	$1.69 \times 10^8$
1227	1500	-49.65	$1.72 \times 10^7$
1327	1600	-46.35	$2.15 \times 10^6$
1427	1700	-43.55	$3.97 \times 10^5$
1527	1800	-40.40	$8.05 \times 10^4$
1627	1900	-37.30	$1.95 \times 10^4$
1727	2000	-34.60	$6.04 \times 10^3$





## REFERENCES

1. Zerlaut, G. A.; Carroll, W. F.; and Gates, D. W., "Spacecraft Temperature-Control Coatings: Selection, Utilization, and Problems Related to Space Environment," Presented at the International Astronautical Federation Congress, Athens, Greece, (September, 1965).
2. Zerlaut, G. A., and Ashford, N., "Development of Space-Stable Thermal-Control Coatings," Report No. IITRI-U6002-73, Contract NAS8-5379, (January, 1969).
3. Plunkett, J. D., "NASA Contributions to the Technology of Inorganic Coatings," NASA-SP-SOL4, U. S. Government Printing Office, Washington, D. C., (November, 1964).
4. Kingery, W. D., Introduction to Ceramics, John Wiley & Sons, Inc., N.Y., N.Y. p 511-545, (1963).
5. Dulin, F. H., and Rase, D. E., "Phase Equilibrium in the System ZnO-TiO<sub>2</sub>," J. Am. Cer. Soc., 43:3 (1960), 125-131.
6. Bartram, S. F., and Slepety's, R. A., "Compound Formation and Crystal Structure in the System ZnO-TiO<sub>2</sub>," J. Am. Cer. Soc., 44 (1961), 493.
7. Campbell, W. B., "Determination of the Feasibility of Forming Refractory Fibers by a Continuous Process," AMRA CR 63-03/8F, (1966).
8. Schaffer, P. S., and Jones, D. W., "Development of Pigments for Thermal Control Coatings," NASA Contract No. NAS8-20162, Lexington Laboratories, Inc., (1966).
9. Wicks, C. E., and Block, F. E., "Thermodynamic Properties of 65 Elements - Their Orders, Halides, Carbides and Nitrides," Bull. 305, Bureau of Mines, (1963).
10. Stull, D. R., "JANAF Thermochemical Tables," National Bureau of Standards Report PBI68370, (August, 1965).
11. Kubo, T.; Kato, M.; Mitarai, Y.; and Uchida, K., "Solid State Reaction of the TiO<sub>2</sub>-ZnO System," Kogys Kagaku Zasshi, 66:4 (1963), 403.
12. Moore, W. J., Physical Chemistry, Prentice-Hall, Inc. p. 103 (1962).
13. Nesmeyanov, A. V., Vapor Pressure of the Chemical Elements, Elsevier Publishing Co., N.Y., p. 447, (1963).
14. Spendlove, H. W., and St. Clair, M. J., "Rate of Evaporation of Zinc at Low Pressures," Bureau of Mines Report of Investigation No. 4710, p. 1-13,,(1950).

15. Spendlove, H. W., and St. Clair, M. J., Rate of Evaporation of Zinc at Low Pressures," Trans. AIME, (1951), 1192-1197.
16. Spendlove, H. W., and St. Clair, M. J., "An Automatic Surface Follower for Measuring the Rate of Evaporation of Molten Metals Undergoing Vacuum Distillation," Rev. Sci. Instr., 23:9 (1952), p. 471-475.
17. Campbell, W. B., and Cochran, J. K., "Apparatus for Controlling Rate of Evaporation of Volatile Metals in Vapor Phase Reaction Systems," Patent Disclosure, Project RF 2633, College of Engineering, The Ohio State University, Columbus, Ohio, (18 December, 1968).
18. Rose, H. E., and Wood, A. J., An Introduction to Electrostatic Precipitation in Theory and Practice, London Constable, (1966).
19. Ruheman, M., The Separation of Gases, (1940).
20. Schoen, H. M., New Chemical Engineering Separation Techniques, N. Y. Interscience Publisher, (1962).
21. Oliver, E. D., Diffusional Separation Processes, N. Y. Wiley and Sons, (1966).
22. Poole, J. B., and Doyle, D., Solid-Liquid Separation, London H. M. S. O. (1966).
23. Pownell, J. H., "Cyclones in the Chemical and Process Industries," Chem. and Ind., (Rev.), 47 (1961), 1888-96.
24. Darby, G. M., "Classification in Hydrocyclones," Bull. Am. Cen. Soc., 34, (1955), 287-90.
25. Bradley, D., The Hydroclone, International Series of Monographs, Chem. Engr., Vol. 4, Pergamon Press, (1965).
26. Rietema, K., and Verven, C. G., Cylcones in Industry, Elsevier Publishing Co., (1961).
27. Wilkinson, B. W., "The Performance Characteristics of Cyclone Dust Collectors," PhD Thesis, The Ohio State University, (1958).
28. Trowbridge, M. E., "Centrifugation," in Solid Liquid Separation, London HMSO, Chp. 6, (1966).
29. Perry, J. H., Ed., Chemical Engineers Handbook, Section 20, (1965).
30. Ibid., p. 64 Section 20.
31. Ibid., p. 1034-1039, (1950 Edition).

32. Encyclopedia of Chemical Technology, Vol. 10, Interscience Publisher, p. 329-352.
33. Berg, E. W., Physical and Chemical Methods of Separation, N. Y. McGraw-Hill, (1963).
34. Oliver, E. D., Diffusion Separation Processes, N. Y. Wiley and Sons, (1966).
35. Pratt, H. R. C., Counter Current Separation Processes, Elsevier Publisher, (1967).
36. Schoen, H. M., New Chemical Engineering Separation Techniques, N. Y. Interscience Publisher, (1962).
37. Pirie, J. M., "Symposium on the Less Common Means of Separation," Institution of Chemical Engineers, London, (1969).
38. Gibbs, H. D., "The Production of Hydrochloric Acid from Chlorine and Water," J. Ind. Engr. Chem., 12:6 (1962), 538.
39. The Handbook of Chemistry and Physics, (1960).
40. Vivian, J. E. and Whitney, R. P., "Absorption of Chlorine in Water," Chemical Engineering Progress, 43:12, (1947), 691-702.
41. Bergholm, Arne, "Chlorination of Rutile," Trans. Metallurgical Society of AIME, 221, (1961), 1121-1129.
42. Rowe, L. W., and Opie, W. R., "Production and Purification of  $TiCl_4$ ," Transactions AIME, Journal of Metals, (November, 1955), 1189-1193.

**Page intentionally left blank**

## APPENDIX A

### FREE ENERGY VALUES USED IN THERMODYNAMIC CALCULATIONS

Table XII- Free Energy Values Used in Thermodynamic Calculations<sup>9,10</sup>

T °C	T °K	$\Delta G^\circ$												
		AlCl <sub>3</sub>	Al <sub>2</sub> O <sub>3</sub>	Cl <sub>2</sub>	CO	CO <sub>2</sub>	HCl	H <sub>2</sub>	TiCl <sub>4</sub>	TiO <sub>2</sub>	Zn	ZnCl <sub>2</sub>	ZnO	Zn <sub>2</sub> TiO <sub>4</sub>
27	300	-136.08	-378.00	0	-32.80	-94.25	-22.75	0	-175.90	-212.00	0	-88.45	-76.10	-369.60
127	400	-134.85	-370.30	0	-35.00	-94.30	-22.95	0	-170.55	-207.90	0	-84.80	-74.65	-362.20
227	500	-133.61	-362.80	0	-37.10	-94.40	-23.90	0	-167.45	-203.60	0	-81.10	-71.30	-351.20
327	600	-132.36	-355.30	0	-39.35	-94.45	-23.40	0	-164.50	-199.30	0	-78.80	-68.95	-342.20
427	700	-131.09	-347.80	0	-41.55	-94.45	-23.60	0	-161.60	-194.95	0	-76.60	-66.60	-333.15
527	800	-129.81	-340.40	0	-43.70	-94.50	-23.75	0	-158.70	-190.75	0	-74.40	-64.00	-323.75
627	900	-128.51	-332.90	0	-45.85	-94.55	-23.90	0	-155.85	-186.55	0	-72.20	-61.50	-314.50
727	1000	-127.01	-325.20	0	-47.95	-94.60	-24.00	0	-152.95	-182.35	0	-70.00	-59.00	-305.35
827	1100	-125.41	-317.20	0	-50.10	-94.60	-24.15	0	-150.05	-178.00	0	-66.72	-56.10	-295.20
927	1200	-123.80	-309.40	0	-52.15	-94.65	-24.40	0	-147.10	-173.89	0	-63.44	-53.40	-285.69
1027	1300	-122.10	-301.50	0	-54.35	-94.70	-24.40	0	-144.15	-169.55	0	-60.16	-50.70	-275.95
1127	1400	-120.57	-293.80	0	-56.25	-94.75	-24.65	0	-141.15	-165.45	0	-56.88	-47.90	-266.25
1227	1500	-118.95	-286.10	0	-58.40	-94.75	-24.70	0	-138.15	-161.20	0	-53.60	-45.10	-256.40
1327	1600	-117.31	-278.10	0	-60.60	-94.80	-24.90	0	-135.20	-157.25	0	-51.50	-42.40	-246.65
1427	1700	-115.67	-270.60	0	-62.65	-94.85	-25.00	0	-132.25	-153.10	0	-49.50	-39.40	-236.90
1527	1800	-114.03	-263.10	0	-64.65	-94.90	-25.25	0	-129.25	-149.35	0	-47.50	-36.60	-227.55
1627	1900	-112.38	-255.50	0	-66.75	-94.90	-25.45	0	-126.25	-145.25	0	-45.50	-33.80	-217.85
1727	2000	-110.73	-247.90	0	-68.75	-95.00	-25.50	0	-123.25	-141.15	0	-43.50	-31.00	-208.15

## APPENDIX B

### COMPUTER PROGRAM FORMAT

```

0001      DIMENSION IDLGR(20,20),IDLGP(20,20),IP(15),IP(15)
0002      DIMENSION IA(15),IB(15),IC(15),MA(15),MB(15),MC(15)
0003      DIMENSION JA(15),JB(15),JC(15),KA(15),KB(15),KC(15)
0004      999 FORMAT(15,1515)
0005      998 FORMAT(3X,3A4,9I7)
0006      997 FORMAT(' DELTA G IS',I9,' CALORIES AT',I3,'00 DEGREES KELVIN AND T
      THE EQUILIBRIUM CONSTANT IS',F12.4)
0007      995 FORMAT('O THE FOLLOWING DATA IS FOR THE REACTION ')
0008      994 FORMAT(' REACTANTS',4X,I2,3A4,I2,3A4,I2,3A4,I2,3A4,I2,3A4,I2,3A4,I2,3A4)
0009      993 FORMAT(' PRODUCTS',5X,I2,3A4,I2,3A4,I2,3A4,I2,3A4,I2,3A4,I2,3A4//)
0010      992 FORMAT('I THE DATA USED IN THESE CALCULATIONS IS ')
0011      991 FORMAT('O',2X,3A4,9I7)
0012      READ(5,999) IRCTN, (IR(I),I=1,IRCTN)
0013      READ(5,999) IPRDT, (IP(I),I=1,IPRDT)
0014      READ(5,998) ((IA(I),IB(I),IC(I), (IDLGR(I,M),M=3,11),MA(I),MB(I),MC(
      II), (IDLGR(I,M),M=12,20)),I=1,IRCTN)
0015      READ(5,998) ((JA(I),JB(I),JC(I), (IDLGP(I,M),M=3,11),KA(I),KB(I),KC(
      II), (IDLGP(I,M),M=12,20)),I=1,IPRDT)
0016      90 WRITE(6,992)
0017      92 WRITE(6,991) ((IA(I),IB(I),IC(I), (IDLGR(I,M),M=3,11),MA(I),MB(I),MC
      I(I), (IDLGR(I,M),M=12,20)),I=1,IRCTN)
0018      91 WRITE(6,991) ((JA(I),JB(I),JC(I), (IDLGP(I,M),M=3,11),KA(I),KB(I),KC
      I(I), (IDLGP(I,M),M=12,20)),I=1,IPRDT)
0019      95 WRITE(6,995)
0020      94 WRITE(6,994) ((IR(I),IA(I),IB(I),IC(I)),I=1,IRCTN)
0021      93 WRITE(6,993) ((IP(I),JA(I),JB(I),JC(I)),I=1,IPRDT)
0022      99 DO 96 M=3,20
0023      A=0
0024      DO 98 K=1,IRCTN
0025      98 A=A+IP(K)*IDLGR(K,M)
0026      B=0
0027      DO 97 K=1,IPRDT
0028      97 B=B+IP(K)*IDLGP(K,M)
0029      YDLG=B-A
0030      YLL=YLL+YDLG
0031      Z=1+YDLG
0032      DELG=YLL*100
0033      X=-DELG/TLN(X)
0034      C=EXP(X)
0035      9116(,997) ILLG,M,C
0036      9117
0037      9118

```



## APPENDIX C

### ALUMINUM OXIDE X-RAY DIFFRACTION PATTERNS

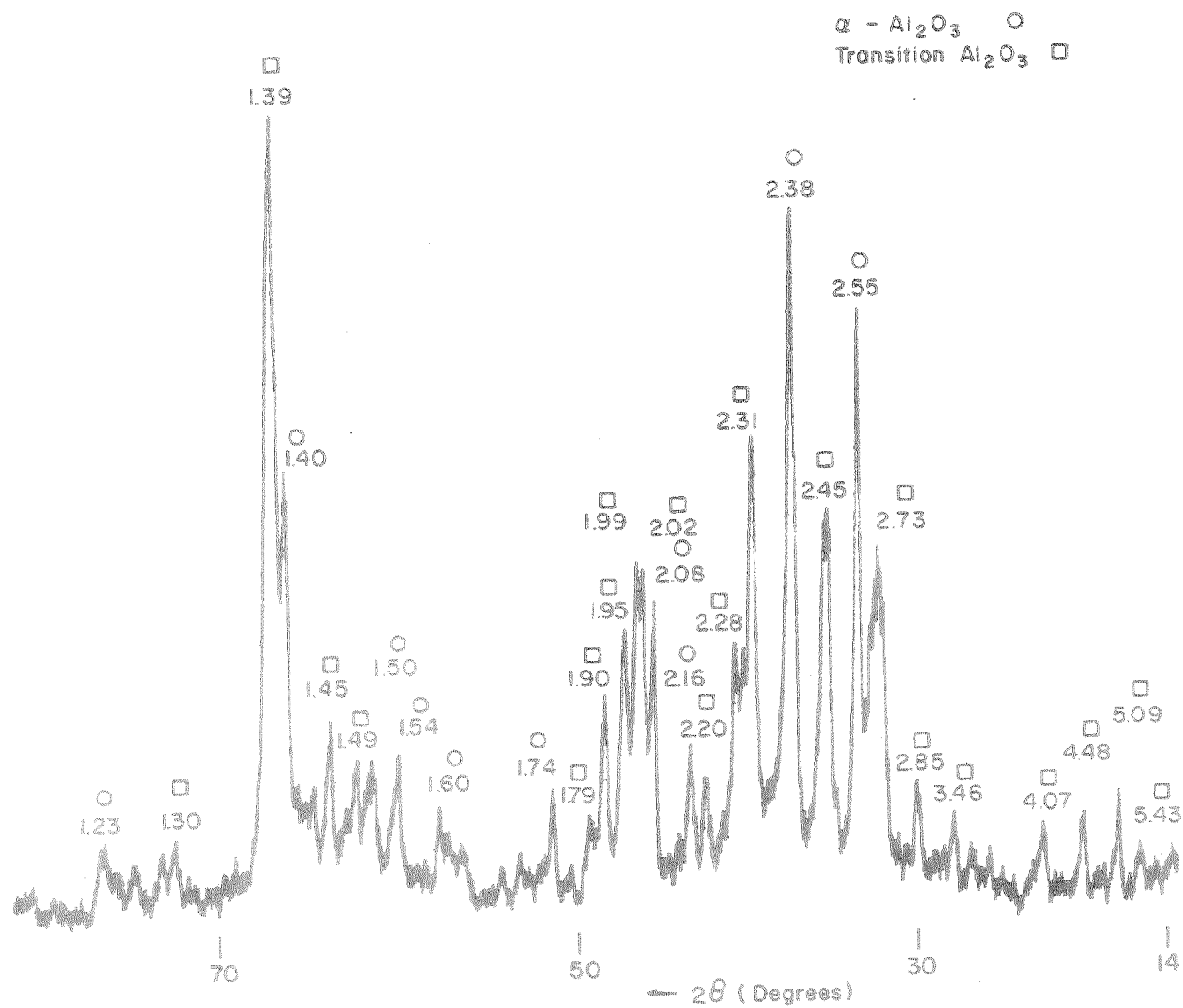


Fig. 29 - X-ray Diffractometer Trace of Vapor Grown Aluminum Oxide Powder from Run VA-10

Table XIII - X-ray Powder Diffraction Data for Alumina, Run No. VA-10

Line No.	2 $\theta$	d spacing	I	Phase	Line No.	2 $\theta$	d spacing	I	Phase
1	17.2	5.15	M	$\Delta\theta$	21	64.4	1.45	M	K, $\theta$
2	19.7	4.50	S	$\Delta,\gamma,N,K,\theta$	22	65.4	1.43	W	K, $\theta$
3	22.2	4.00	M	$\Delta$	23	67.4	1.39	S	$\alpha,\Delta,\gamma,N,K,\theta$
4	25.2	3.53	W	$\alpha,\theta$	24	72.6	1.30	W	K
5	27.5	3.24	W		25	73.5	1.29	M	$\Delta,\theta$
6	29.4	3.04	W	K	26	74.3	1.28	M	
7	31.5	2.84	S	$\Delta,N,K,\theta$	27	75.8	1.25	W	$\Delta,\theta$
8	33.1	2.70	M	$\Delta,K,\theta$	28	76.9	1.24	W	
9	34.6	2.59	S	$\alpha,\Delta,K,\theta$	29	77.7	1.23	M	N, $\theta$
10	36.9	2.43	S	$\Delta,\gamma,N,K,\theta$	30	81.9	1.18	W	
11	39.1	2.30	M	$\Delta,\gamma,N,K,\theta$	31	83.9	1.15	W	$\gamma,\Delta$
12	42.6	2.12	W	$\alpha,K,\theta$	32	85.6	1.13	M	N
13	45.9	1.98	M	$\Delta,\gamma,N,K,\theta$	33	88.5	1.10	W	
14	46.9	1.94	M	$\Delta,K$	34	94.1	1.05	M	
15	48.2	1.89	M	K, $\theta$	35	96.5	1.03	M	$\gamma,N$
16	51.0	1.79	W	K	36	99.6	1.01	M	
17	57.4	1.60	W	$\alpha,\theta$	37	101.6	.993	M	
18	60.4	1.53	M	$\gamma,N,\theta$	38	102.5	.988	W	$\gamma$
19	61.7	1.50	M	K	39	104.7	.979	M	
20	62.7	1.48	M	$\theta$	40	108.1	.951	M	
					41	111.2	.934	M	

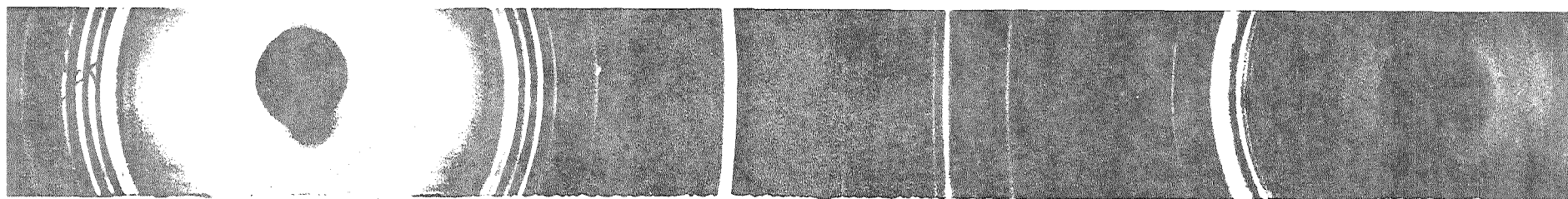


Fig. 30 - X-ray Diffraction Pattern for Alumina, Run VA-10

**Page intentionally left blank**

## APPENDIX D

### TITANIUM DIOXIDE X-RAY DIFFRACTION PATTERNS

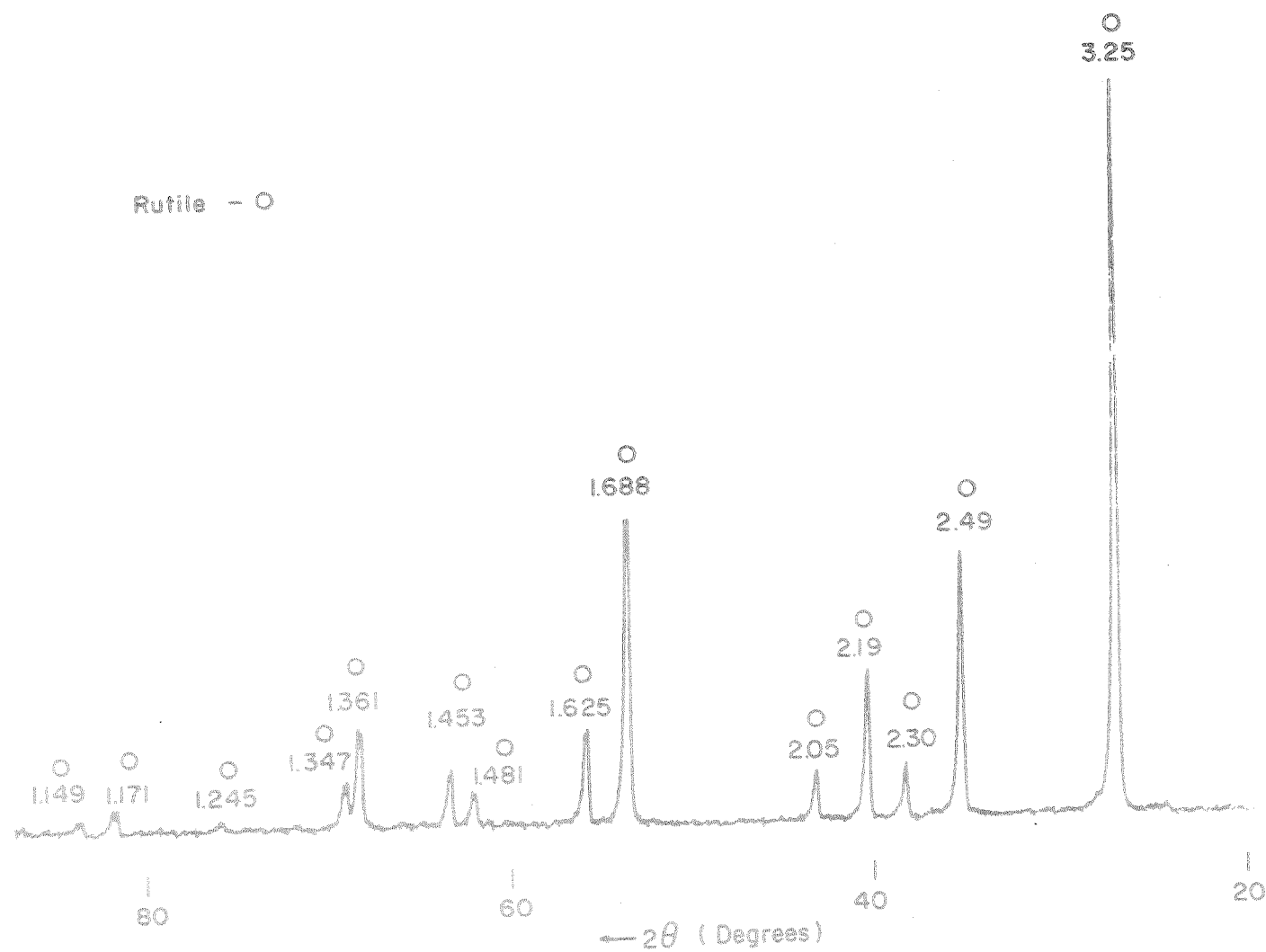
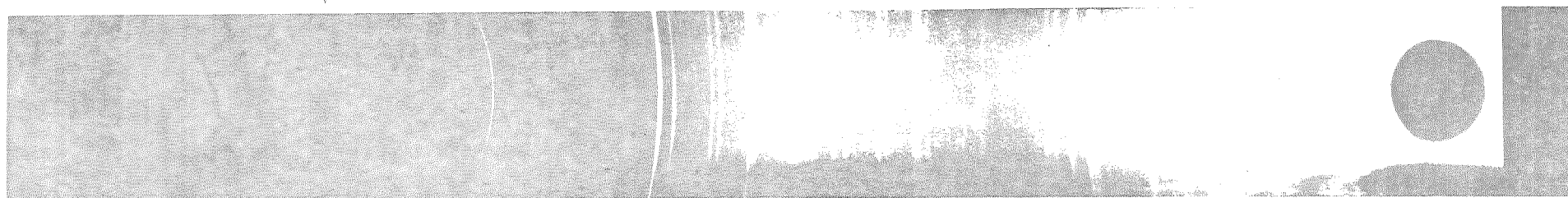


Fig. 31 - X-ray Diffractometer Trace of Vapor Grown Rutile Powder  
from Run TiO<sub>2</sub>-1

Table XIV - X-ray Powder Diffraction Data for Titanium, Run No. TiO<sub>2</sub>-1

Line No.	2θ	d spacing	I	Phase	Line No.	2θ	d spacing	I	Phase
1	27.63	3.225	S	TiO <sub>2</sub>	19	95.53	1.040	W	TiO <sub>2</sub>
2	36.28	2.474	M	TiO <sub>2</sub>	20	97.48	1.0246	VW	TiO <sub>2</sub>
3	39.43	2.283	W	TiO <sub>2</sub>	21	106.18	.9633	VW	TiO <sub>2</sub>
4	41.48	2.175	M	TiO <sub>2</sub>	22	116.53	.9056	W	TiO <sub>2</sub>
5	44.23	2.046	W	TiO <sub>2</sub>	23	117.88	.8992	W	TiO <sub>2</sub>
6	45.73	1.982	W	Camera	24	120.28	.8882	M	TiO <sub>2</sub>
7	54.53	1.681	S	TiO <sub>2</sub>	25a	122.88	.8770	M	TiO <sub>2</sub>
8	56.78	1.620	M	TiO <sub>2</sub>	25b	123.63	.8739	W	TiO <sub>2</sub>
9	62.98	1.475	W	TiO <sub>2</sub>	26a	131.88	.8459	W	TiO <sub>2</sub>
10	64.18	1.450	W	TiO <sub>2</sub>	26b	132.58	.8413	VW	TiO <sub>2</sub>
11	69.13	1.357	M	TiO <sub>2</sub>	27a	136.68	.8288	W	TiO <sub>2</sub>
12	69.93	1.344	W	TiO <sub>2</sub>	27b	137.43	.8266	VW	doublet
13	76.63	1.242	VW	TiO <sub>2</sub>	28a	140.08	.8195	M	TiO <sub>2</sub>
14	82.48	1.168	W	TiO <sub>2</sub>	28b	140.98	.8172	W	doublet
15	84.38	1.147	W	TiO <sub>2</sub>	29a	155.78	.7879	VW	
16	87.78	1.111	VW	TiO <sub>2</sub>	30a	162.13	.7797	W	
17	89.73	1.092	W	TiO <sub>2</sub>	30b	163.88	.7779	VW	
18	90.93	1.080	W	TiO <sub>2</sub>					

Fig. 32 - X-ray Diffraction Pattern for Titania, Run TiO<sub>2</sub>-1

**Page intentionally left blank**



APPENDIX E

ZINC ORTHOTITANATE X-RAY DIFFRACTION PATTERNS

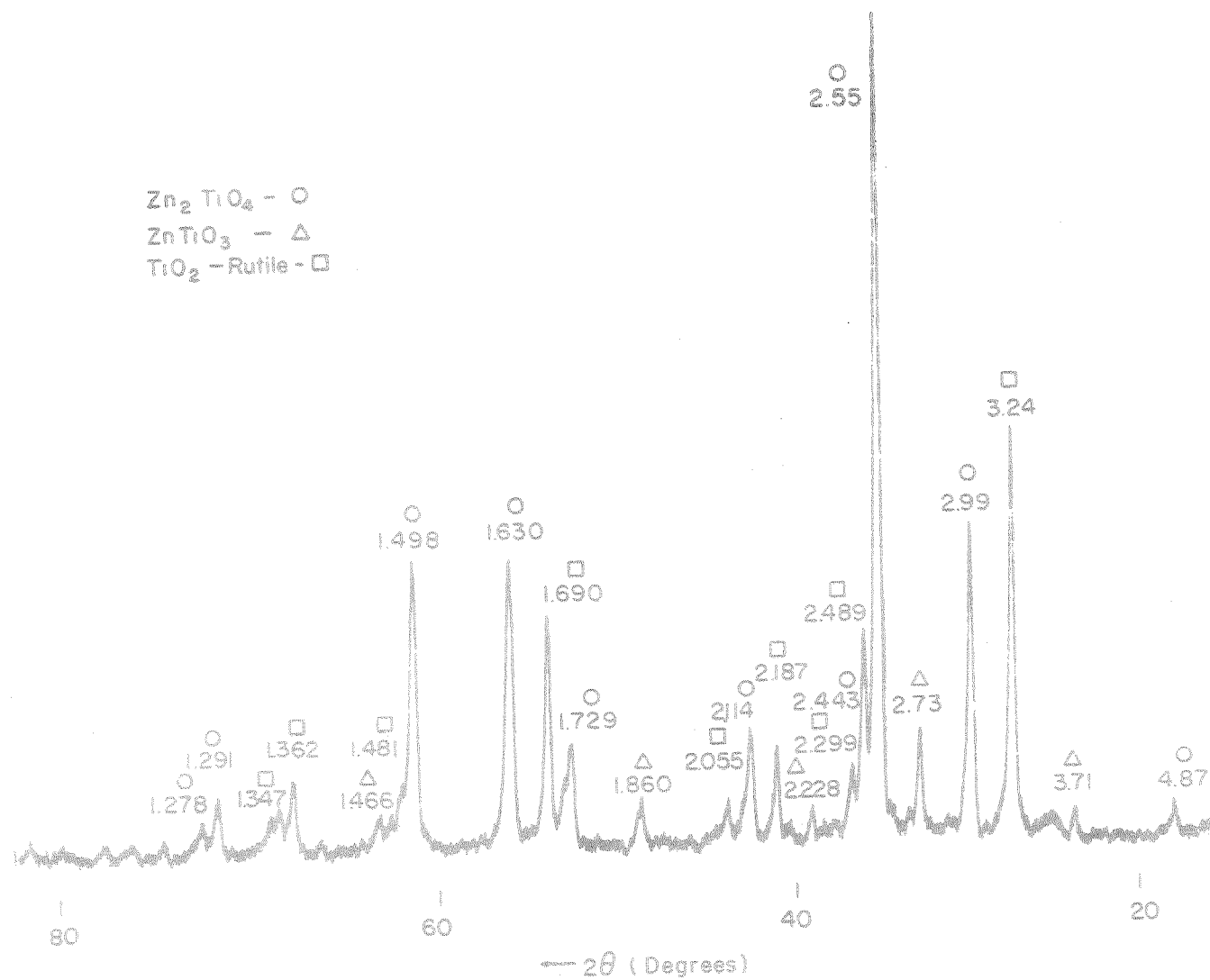


Fig. 33 - X-ray Diffractometer Trace of Oxides from Run  $\text{Zn}_2\text{TiO}_4$ -2, Showing  $\text{Zn}_2\text{TiO}_4$  as the Major Phase

Table XV - X-ray Powder Diffraction Data for Zinc Orthotitanate, Run Zn<sub>2</sub>TiO<sub>4</sub>-1

Line No.	2θ	d spacing	I	Phase	Line No.	2θ	d spacing	I	Phase
1	27.45	3.250	S	TiO <sub>2</sub>	24	85.90	1.133	W	Zn <sub>2</sub> TiO <sub>4</sub>
2	29.90	2.989	S	Zn <sub>2</sub> TiO <sub>4</sub>	25	87.45	1.117	VW	TiO <sub>2</sub> , ZnTiO <sub>3</sub>
3	32.90	2.723	M	ZnTiO <sub>3</sub>	26	88.75	1.103	M	Zn <sub>2</sub> TiO <sub>4</sub>
4	35.25	2.547	VS	ZnTiO <sub>3</sub> , Zn <sub>2</sub> TiO <sub>4</sub>	27	89.40	1.097	VW	TiO <sub>2</sub>
5	36.10	2.489	W	TiO <sub>2</sub>	28	90.70	1.084	VW	TiO <sub>2</sub>
6	39.20	2.299	VW	TiO <sub>2</sub>	29	93.50	1.060	W	Zn <sub>2</sub> TiO <sub>4</sub>
7	40.70	2.218	VW	ZnTiO <sub>3</sub>	30	95.15	1.045	VW	TiO <sub>2</sub>
8	41.35	2.185	W	TiO <sub>2</sub>	31	97.05	1.030	VW	TiO <sub>2</sub>
9	42.80	2.114	W	Zn <sub>2</sub> TiO <sub>4</sub>	32	101.20	0.999	W	Zn <sub>2</sub> TiO <sub>4</sub>
10	44.10	2.055	VW	TiO <sub>2</sub>	33	104.00	0.979	W	Zn <sub>2</sub> TiO <sub>4</sub>
11	49.00	1.860	W	ZnTiO <sub>3</sub>	34	105.10	0.972	VW	
12	53.05	1.728	M	ZnTiO <sub>3</sub> , Zn <sub>2</sub> TiO <sub>4</sub>	35	109.10	0.947	VW	
13	54.40	1.688	S	TiO <sub>2</sub>	36	116.40	0.908	VW	TiO <sub>2</sub>
14	56.55	1.629	S	Zn <sub>2</sub> TiO <sub>4</sub> , TiO <sub>2</sub> , ZnTiO <sub>3</sub>	37	117.30	0.904	VW	
15	62.05	1.497	S	ZnTiO <sub>3</sub> , Zn <sub>2</sub> TiO <sub>4</sub>	38	120.35	0.889	W	TiO <sub>2</sub>
16	69.00	1.362	W	TiO <sub>2</sub>	39	122.50	0.880	VW	
17	73.35	1.292	W	Zn <sub>2</sub> TiO <sub>4</sub>	40	123.30	0.876	VW	TiO <sub>2</sub>
18	74.30	1.278	VW	Zn <sub>2</sub> TiO <sub>4</sub>	41	126.00	0.866	W	
19	76.60	1.245	VW	TiO <sub>2</sub>	42	131.65	0.846	VW	TiO <sub>2</sub>
20	78.20	1.224	VW	Zn <sub>2</sub> TiO <sub>4</sub>	43	136.30	0.831	W	TiO <sub>2</sub>
21	79.65	1.205	VW	ZnTiO <sub>3</sub> , TiO <sub>2</sub>	44	136.90	0.829	VW	TiO <sub>2</sub>
22	82.35	1.172	VW	TiO <sub>2</sub> , ZnTiO <sub>3</sub>	45	139.70	0.822	S	TiO <sub>2</sub>
23	84.10	1.152	VW	ZnTiO <sub>3</sub>	46	140.50	0.821	VW	TiO <sub>2</sub>

Fig. 34 - X-ray Diffraction Pattern for Zinc Orthotitanate,  
Run Zn<sub>2</sub>TiO<sub>4</sub>-1